THE UNIVERSITY OF CHICAGO

OBJECTIVE CHARACTERIZATION OF IMAGE RECONSTRUCTION ALGORITHMS IN COMPUTED TOMOGRAPHY AND DIGITAL BREAST TOMOSYNTHESIS

A DISSERTATION SUBMITTED TO
THE FACULTY OF THE DIVISION OF THE BIOLOGICAL SCIENCES
AND THE PRITZKER SCHOOL OF MEDICINE
IN CANDIDACY FOR THE DEGREE OF
DOCTOR OF PHILOSOPHY

COMMITTEE ON MEDICAL PHYSICS

BY
SEAN DOUGLAS ROSE

CHICAGO, ILLINOIS
JUNE 2018

To my family

TABLE OF CONTENTS

LIST OF FIGURES

ACKNOWLEDGMENTS

I would like to begin by expressing my deepest gratitude to Dr. Emil Sidky and Dr. Xiaochuan Pan, who, throughout my time in graduate school, have provided invaluable support and guidance during this formative stage of my scientific career. It has been a great privilege to receive instruction from such outstanding mentors. I have watched many friends come through this lab over the past 5 years and seen the same level of care devoted to each and every student. Such dedication to educating graduate students has not gone unnoticed, and I offer my sincerest thanks for the countless times they provided me with advice, discussion, or simply friendly conversation.

I also wish to thank the members of my thesis committee, Dr. Ingrid Reiser and Dr. Chien-Min Kao, for their support and encouragement over the course of my doctoral studies. I've been extremely lucky to have the opportunity to work with and learn from a number of excellent collaborators in both industry and academia over the course of my Ph.D. studies. I would particularly like to acknowledge Dr. Martin Andersen, Dr. Dirk Lorenz, Dr. Frank Schöpfer, Dr. Chris Ruth, and Dr. Yiheng Zhang for aiding in my research efforts.

I am indebted to my many friends within the graduate program who've provided both scientific and personal support over the years. I'm especially appreciative of my former lab mates Dr. Adrian Sanchez, Dr. Zheng Zhang, Dr. Buxin Chen, Dr. Erik Pearson, Dr. Andrew Davis, and Dr. Xiao Han. In addition I'd like to thank all of the current and former students of the graduate program in medical physics with whom I've had the pleasure to interact.

Grant support from the Ruth L. Kirchstein NRSA F-31 EB023076 and the Lawrence H. Lanzl Award helped to make this work possible, along with NIH R01 Nos. CA182264 and EB018102.

Ultimately, I could not have performed this work without the unconditional love and support of my family and girlfriend, Rebecca, who, on more occasions than I can count, have been there to pick me up when I needed it.

ABSTRACT

Both X-ray computed tomography (CT) and digital breast tomosynthesis (DBT) have become important clinical tools for the non-invasive assessment and diagnosis of disease in the breast. The continuing development and refinement of image reconstruction methods has led to significant improvements in image quality in both of these modalities. In particular, sparsity exploiting iterative image reconstruction (IIR) methods have demonstrated potential for yielding images of improved quality from the high-noise and limited angular data encountered in breast CT and DBT, respectively; however, realization of these improvements typically requires manual tuning of numerous parameters, often in a case-by-case fashion. Even in the absence of complications introduced by the incorporation of sparsity-exploiting regularizers, it is often difficult to establish a direct link between the parameters involved in specifying an IIR algorithm and the quality of the resulting reconstruction. This thesis aims to address this issue in the context of breast CT and DBT. As a step towards this goal, we simplify the problem by considering IIR without sparsity exploiting regularizers. The primary focus of this thesis is the characterization of parameter trends for such IIR algorithms in breast CT and DBT.

CHAPTER 1

INTRODUCTION

X-ray computed tomography (CT) has become an invaluable clinical tool for the non-invasive assessment and diagnosis of disease. While planar radiography had already become a staple in the clinic at the time CT was invented, the overlap of tissues in a 2D projection image limited application of X-ray imaging to many diagnostic imaging tasks. The advent of CT removed this limitation, allowing physicians to non-invasively attain a three-dimensional representation of the internal anatomical structure of a patient. The clinical value of this achievement has repeatedly been demonstrated in the decades since, with CT being adopted as a workhorse modality for countless diagnostic imaging tasks.

In the years since the development of CT, X-ray tomographic imaging has been applied in numerous forms, ranging from dedicated CT systems to hybrid systems combining CT with nuclear medicine imaging modalities like positron emission tomography. While many of these systems have now been staples in the clinic for some time, new applications and extensions of X-ray tomography continue to be developed and investigated. The realization of these applications is enabled in part by the continuing development and refinement of CT image reconstruction, the process by which X-ray projections obtained from multiple angles are processed and combined to create a three-dimensional image.

Adaptation of X-ray CT to specific clinical tasks often requires modification of system design to accommodate constraints imposed by clinical application. This has led to the development of many systems employing novel acquisition geometries and/or low-dose imaging. One example is in the area of dedicated breast imaging, in which there are currently two FDA-approved tomographic imaging modalities: (1) breast CT and (2) digital breast tomosynthesis (DBT). The system design for each modality is motivated in part by maintaining patient dose levels similar to those employed in two-view digital mammography. The maximum dose delievered per X-ray projection is limited by this constraint in both modalities. In addition, DBT's widespread adoption for breast cancer screening is at least in part

attributable to its similarity to digital mammography, the predominant modality for screening at the time of DBT's invention. The similarities between the two modalities eased the transition to DBT as it did not cause major changes to the clinical workflow. Maintaining a design similar to that of mammography constrains the system to only acquire X-ray projections over a small angular range.

Such system design constraints impose challenges for image reconstruction, as the data quality is reduced relative to that in diagnostic CT. In breast CT, the data suffers from high noise due to the maximum dose per projection being constrained by the dose in two-view mammography. In DBT, the limited angular range of acquisition and relatively large angular spacing between adjacent X-ray projections causes artifacts when applying traditional tomographic reconstruction methods. These challenges have motivated much interest in iterative image reconstruction (IIR) methods, which have shown much promise for improving image quality in existing tomographic imaging modalities and in enabling novel system designs. In particular, IIR has been applied in both high-noise and limited angle data scenarios and shows potential for improving image quality relative to traditional analytic reconstruction methods. In our lab, much effort has been devoted over the past decade to the development and application of sparsity-exploiting IIR for improving image quality in nonstandard applications of tomographic imaging, including efforts focused on both breast CT [1] and DBT [2].

While it is widely accepted that sparsity-exploiting IIR has demonstrated potential for improving image quality in both breast CT and DBT, realizing this potential typically requires manual tuning of numerous parameters, often on a case-by-case basis. Moreover, when artifacts are observed in a IIR reconstruction, the cause can be difficult to ascertain. Traditional analytic methods, like filtered backprojection, involve a two-step procedure that can be analyzed in a step-wise fashion to aid in tuning parameters and determining the origin of artifacts. By contrast, in IIR, the reconstruction is defined implicitly as a solution to an optimization problem. Even in the absence of sparsity-exploiting regularization

strategies, which further complicate the problem, it is still often difficult to establish a direct link between the parameters in the underlying optimization problem and the appearance of a reconstruction in IIR. It is thereby challenging to develop robust methods of setting these parameters.

This thesis works towards addressing this issue in the context of breast CT and DBT. To aid in the development of sparsity-exploiting IIR, we believe it is important to further our understanding of the link between parameters in the optimization problems motivating IIR and the quality of reconstructed images. As a step towards this goal, we simplify the problem by considering IIR without sparsity exploiting regularizers. The primary focus of this thesis is the characterization of parameter trends for such IIR algorithms in breast CT and DBT. Chapter 3, in which we directly investigate early truncation of a sparsity exploiting IIR algorithm, is an exception. In the process of performing the work, a number of objective image quality metrics are employed that can be of use in guiding reconstruction algorithm development.

This rest of this introductory chapter is devoted to providing necessary background regarding the modeling of X-ray imaging systems and analytic and IIR methods in breast CT and DBT. In section 1.1.2 the system geometry of a CT system and a forward model for X-ray transmission are discussed. Next, section 1.1.3 provides a brief description of how to implement the most common analytic reconstruction method, filtered backprojection (FBP), and is followed by a discussion of IIR in section 1.1.4. We then turn our attention to DBT, beginning with a broad overview of the modality in section 1.2.1. Details of the system geometry are presented in section 1.2.2 followed by a discussion of artifacts that result from the limited angular sampling scheme in section 1.2.3.

The remainder of the thesis is organized as follows. In Chapter 2, a detailed analysis of discrete-to-discrete forward models in IIR for breast CT is presented. The studies in this chapter focus only on the converged solutions to the optimization problems motivating iterative reconstruction. In Chapter 3, the focus is expanded to the effects of early truncation

on the design of sparsity-exploiting iterative reconstruction algorithms in breast CT. In particular, a class of algorithms known to exhibit fast initial convergence are employed to investigate whether design considerations in the reconstruction optimization problems can be observed at early iterations.

Next, in Chapter 4, the focus shifts to DBT and an investigation of simulation-based metrics for characterizing IIR algorithms is presented. Image fidelity metrics, which are often employed to characterize reconstruction algorithms in CT, do not extend well to DBT due to the extremely limited angular range of acquisition. The goal of this chapter is to investigate and demonstrate alternative metrics for this purpose, and, in the process, to characterize important parameter trends in IIR for DBT. In Chapter 5, a study is performed to investigate how IIR design can be used to mitigate the orientation dependence of fiber-like signals in DBT. In the process, simulation-based metrics are employed to characterize the performance of the algorithms. Chapter 6 gives conclusions and some final considerations.

1.1 Background: Dedicated Breast Computed Tomography

1.1.1 Overview

It is well-established that large scale mammographic screening, which has now been performed in the U.S. for over 30 years, has led to a decrease in the mortality rate from breast cancer. While the benefits of screening are clear, the sensitivity and specificity of the modality are limited by the superposition of 3D structures in a 2D mammographic image of the breast. This limitation has led to the development of a number of systems attempting to use variants of tomographic imaging to obtain 3D images of the breast. One approach is dedicated breast CT [3], in which the patient lies prone with the breast pendant through an aperture in the table. A source-detector pair, located under the table, rotate around the patient's breast obtaining low-dose projection images. These projections are then reconstructed into a 3D image of the breast. Depending on the number of projections and dose

per projection, the average glandular dose in breast CT can vary from approximately that of two-view screening mammography to that of diagnostic mammography.

Breast CT is a relatively young imaging modality, with the first FDA approved system becoming available only in 2015, therefore the eventual role it will play in the clinic is not yet clear. However, the technology has a number of potential applications. For example, use of breast CT for diagnostic work-up could reduce the need for other techniques, such as mammographic imaging with magnifcation views or spot compression, and could possibly improve diagnostic accuracy [4]. Also, the fact that breast CT provides the capability of imaging the breast without compression could have potential benefits. Breast compression, in addition to reducing patient comfort, alters the relative positioning of structures in the breast. Imaging without compression removes this issue and could therefore possibly be of use in surgical planning.

1.1.2 System Geometry and Forward Model

The breast CT configurations considered in Chapters 2 and 3 constitute fan-beam system geometries. In these geometries, a source-detector pair rotate in a circular trajectory about an object, acquiring projection data at uniformly separated angular increments. A schematic of such a system geometry is shown in Figure 1.1. The geometry is defined by the detector length, source-detector distance, and the radius of the source trajectory, often referred to as the source-isocenter distance.

Performing reconstruction requires a model for the measurement process of this system. The model must relate the spatial distribution of X-ray attenuation coefficient $\mu(\mathbf{r}, E)$ of the object to the measurement g_i corresponding to the i^{th} ray, defined by source position $\mathbf{s}_i$ and direction vector $\hat{\boldsymbol{\theta}}_i$. Regarding notation, throughout this thesis boldface type is reserved for vectors denoting positions or directions in space, while italic type is used for scalars and all other vectors. Consider an incident X-ray energy spectrum $I_0(E)$. The measurement can be

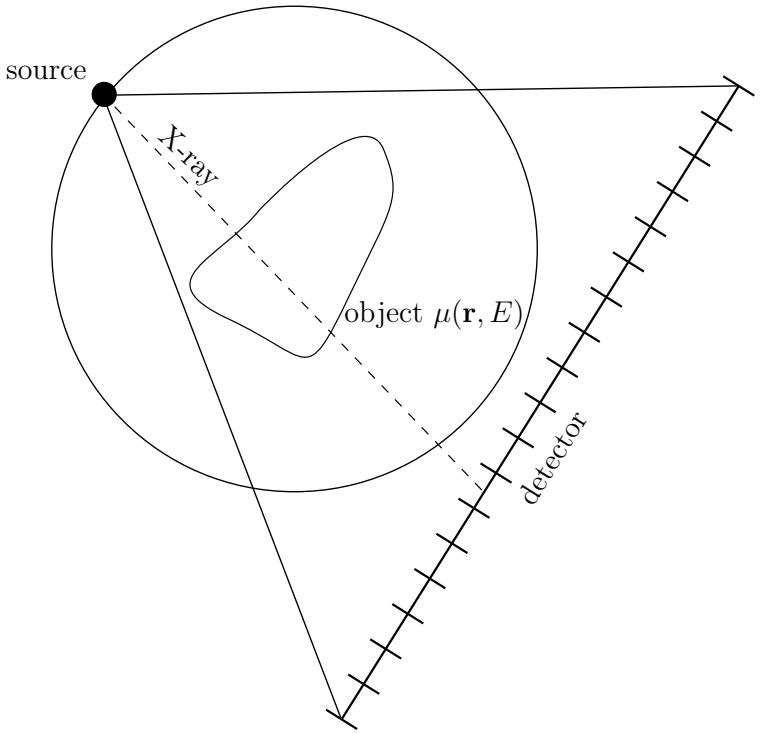

Figure 1.1: Schematic of fan-beam CT system geometry with X-ray attenuation distribution $\mu(\mathbf{r}, E)$.

modeled by the equation

$$g_i = \int_E \Lambda(E) \text{Poisson} \left\{ I_0(E) \exp\left(- \int_{\Re} \mu(\mathbf{s}_i + t\hat{\boldsymbol{\theta}}_i) \mathrm{d}t \right) \right\} \mathrm{d}E \tag{1.1}$$

where $\Lambda(E)$ denotes the response of the detector to an incident X-ray of energy E, Poisson$(\cdot)$ returns a random variable following a Poisson distribution with mean given by its argument, and $\Re$ denotes the reals. Note that this model neglects the finite size of the focal spot and detector bin and also the contribution of scatter to the measurement. It also ignores noise introduced by the detector electronics. The raw measurements g_i are often referred to as the *transmission data*.

The forward model in equation 1.1 is nonlinear and impossible to invert without further simplifying assumptions. To arrive at a more useful forward model for image reconstruction, first, assume the incident X-ray beam is monoenergetic. Doing so, the dependencies on

energy can be dropped and the model reduces to the equation

$$g_i = \Lambda I_0 \text{Poisson}\left\{\exp\left(-\int_{\Re} f(\mathbf{s}_i + t\hat{\boldsymbol{\theta}}_i)\mathrm{d}t\right)\right\}$$

where the monoenergetic X-ray attenuation coefficient distribution has been denoted by $f(\mathbf{r})$. Dividing both sides by $I_0\Lambda$ and taking the negative logarithm yields the equation

$$\begin{aligned} b_i &= -\log\left(\frac{g_i}{\Lambda I_0}\right) \\ &= \int_{\Re} f(\mathbf{s}_i + t\hat{\boldsymbol{\theta}}_i)\mathrm{d}t + p_i \end{aligned} \tag{1.2}$$

where it has been assumed the noise can be modeled by an additive Gaussian random variable p_i. The model in 1.2 is linear in f and denotes a sampling of the X-ray transform [5] of the function f with additive noise. The model is often referred to as being continuous-to-discrete because it maps a continuously defined function f to a discrete set of measurements b_i. The post-logarithm measurements b_i are often referred to as the *sinogram data*.

There are two general classes of CT image reconstruction algorithms. The first class, known as analytic methods, are motivated by inverting continuous-to-discrete models like the one in equation 1.2. The second class, called iterative methods, are based on inverting discretized formulations of the X-ray projection forward model. We will first provide an overview of the filtered back-projection method, the most commonly employed of analytic reconstruction methods, before moving on to discuss iterative reconstruction methods.

1.1.3 Analytic reconstruction: FBP

This section provides a brief summary of the most commonly employed analytic reconstruction algorithm, filtered back-projection (FBP). As the goal is only to provide the details necessary to implement the algorithm, underlying theory required to derive the algorithm is not presented. The interested reader is referred to Ref. [6, ch. 3] for a detailed derivation

of the algorithm and Refs. [5, 7] for more information regarding the theory of the X-ray transform.

The fan-beam FBP algorithm consists of three steps. To begin, consider the sinogram data vector $b \in \Re^m$ containing the measurements from each ray b_i. Assume data is acquired from J source positions and there are K detector bins. Denote the elements of b corresponding to the j^{th} view by $b^{(j)} \in \Re^K$. Let the variable $k = 1, \ldots, K$ index the detector elements within each view, with $k = k_c$ corresponding to the central ray. The first step consists of weighting all of the views according to the formula

$$c_k^{(j)} = b_k^{(j)} \frac{D}{\sqrt{D^2 + (k - k_c)^2 \Delta u^2}}$$

where D denotes the source-detector distance and Δu is the detector bin size. This step can be expressed in a more succinct fashion using vector notation

$$c = \text{diag}(w) b$$

where $w \in \Re^m$ is a vector containing the weights and the diag operator creates a square, diagonal matrix out of its argument.

In the second step, the vector of weighted measurements c is filtered in a view-by-view fashion using the ramp filter. As the ramp filter is a high-pass filter and therefore amplifies noise, its high frequency response is typically tapered with an apodizing window. One common window which will be used in many of the following chapters is the Hanning window. The frequency response of this window is defined by

$$H(\nu) = \begin{cases} \frac{1}{2}\left(1 + \cos\left(\frac{\pi\nu}{\nu_H}\right)\right) & |\nu| < \nu_H \\ 0 & \text{else} \end{cases}$$

where ν_H is referred to as the cutoff frequency. The cutoff frequency of the Hanning window

is an important parameter that controls the noise-resolution tradeoff of FBP reconstruction. Larger values of ν_H tend to yield reconstructions of higher noise content and higher resolution, while lower values of ν_H will yield reconstructions of lower noise but degraded resolution. It is common to express the cutoff frequency ν_H as a fraction of the Nyquist frequency of the detector via the equation

$$\nu_c = \frac{\nu_H}{\nu_{max}} = \nu_H(2\Delta u)$$

where $\nu_{max} = \frac{1}{2\Delta u}$ is the Nyquist frequency. This convention will be followed throughout this thesis. As with the weighting step, the filtering step can be succinctly expressed in vector notation. Denoting the discrete Fourier transform (DFT) operation by W, we have

$$c' = W^{-1}\,\mathrm{diag}(h)Wc$$

where h is a vector containing samples of the ramp filter multiplied by the Hanning window.

In the last step, a weighted backprojection of the filtered vector c' is performed yielding a pixelized image $x \in \Re^n$. The weighted backprojection operation will be denoted by B. For the exact form of the operator the reader is referred to [6, ch. 3]. The resulting image can be expressed as a linear function of the sinogram data b

$$x = BW^{-1}\,\mathrm{diag}(h)W\,\mathrm{diag}(w)b$$

1.1.4 Iterative Reconstruction

While analytic methods have been employed in CT systems for many decades, much research on iterative image reconstruction (IIR) algorithms has demonstrated the potential to provide images of improved quality, particularly in scenarios involving novel scanning trajectories or noisy data. These improvements, though, come at the cost of an increase in the number of implementation choices required to implement an algorithm. Even the simplest of IIR

algorithms involve a much greater number of parameters than their analytic counterparts.

While analytic methods are motivated by inverting a continuous-to-discrete forward model, as in equation 1.2, iterative methods are based on discrete-to-discrete imaging models. To obtain a discrete-to-discrete imaging model we return to equation 1.2, repeated here for clarity

$$b_i = \int_{\Re} f(\mathbf{s}_i + t\hat{\boldsymbol{\theta}}_i)\mathrm{d}t + p_i$$

Consider a set of n functions $\{\alpha_j(\mathbf{r})\}_{j=1,\ldots,n}$. These functions are traditionally taken to be pixels (voxels in 3D), which are defined to be 1 within a retangle (rectangular prism) and zero elsewhere, but other forms, such as Kaiser Bessel functions [8], have been proposed. The set of functions $\{\alpha_j(\mathbf{r})\}_{j=1,\ldots,n}$ is called an *expansion set* and is used to approximately represent the function f via a linear combination

$$f(\mathbf{r}) \approx \sum_{j=1}^{n} x_j \alpha_j(\mathbf{r}) \tag{1.3}$$

where $x \in \Re^n$ is a vector of expansion coefficients. Plugging equation 1.3 into the continuous-to-discrete forward model, one obtains

$$\begin{aligned} b_i &= \sum_{j=1}^{n} a_{ij} x_j + p_i \\ a_{ij} &= \int_{\Re} \alpha_j(\mathbf{s}_i + t\hat{\boldsymbol{\theta}}_i)\mathrm{d}t \end{aligned} \tag{1.4}$$

Constructing a matrix $A \in \Re^{m \times n}$ out of the elements a_{ij}, the system of equations can be written in the form

$$b = Ax + p \tag{1.5}$$

The forward model in equation 1.5 is analogous to the continuous-to-discrete forward

model 1.2, but here both the image and data are discretized. As such, this forward model is often referred to as a *discrete-to-discrete* imaging model. Operation by the matrix A is called forward projection while operation by its transpose is referred to as back projection. Note, however, that back projection can also be defined as a continuous-to-discrete operation. Discretization of this operation can lead to forward/back projector pairs that are "mismatched" in the sense that they are not transposes of each other. In all studies in this thesis, forward/back projector pairs are implemented as transpose operations.

While direction inversion of a discrete-to-discrete imaging model can be used for image reconstruction, IIR methods are often instead motivated by a reconstruction optimization problem. This allows for the addition of a regularization term to control the noise-resolution tradeoff, analogous in some ways to the apodizing window in FBP. Reconstruction optimization problems generally take the form

$$\min_x \phi(Ax, b) + \lambda\psi(x) \tag{1.6}$$

where ϕ is a *data-fidelity* function penalizing differences between Ax and b, while ψ is a *regularization* term which penalizes images based on some undesirable characteristic. For example, the Euclidean norm of the spatial gradient of the image is often employed as a form of regularization to yield smoother reconstructions. The scalar λ is called the regularization strength and controls the noise-resolution tradeoff in iterative reconstruction.

Reconstruction optimization problems can often not be solved in closed form, so iterative algorithms are typically required to obtain reconstructions, hence the name iterative image reconstruction. Even in cases where a closed-form solution can be written, it typically involves the inverse of the matrix A, which is difficult to compute and store in practice due to the extremely large size of the matrix.

Image Reconstruction Parameters

As can be seen from the previous sections, both analytic and IIR algorithms involve a number of important parameters and implementation choices that can impact the quality of reconstructions. In FBP, implementation essentially boils down to three choices: (1) width of the apodizing window ν_H, (2) pixel size, and (3) definition of the back-projection operation B. These choices are non-trivial and, in fact, have been the topic of much research; however, things become even more complicated when considering IIR.

In IIR, there are two classes of reconstruction parameters: *algorithm* and *problem* parameters. Algorithm parameters are those quantities involved in defining the iterative algorithm used to solve the motivating reconstruction optimization problem. Examples include the step size, search direction, and number of iterations. Problem parameters are involved in defining the motivating reconstruction optimization problem and include the regularization strength λ, expansion set, functional form of the data-fidelity and regularizer terms ϕ and ψ, and definition of the forward projection operator A. A pervading theme throughout this thesis is the characterization of reconstructions as a function of both problem and algorithm parameters using objective image quality metrics.

1.2 Background: Digital Breast Tomosynthesis

1.2.1 Overview

Though the concept of tomosynthesis was first described in the 1960s [9], development did not begin on what would become its first major clinical application, DBT, until the late 1990s [10]. It was another 14 years before the first FDA approved DBT system, the Hologic Selenia Dimensions, hit the market. Since then, DBT has enjoyed widespread adoption as either an adjunct to, or replacement for, digital mammography for breast cancer screening. As such, development of DBT has continued and the FDA has approved three more DBT systems, each employing different acquisition geometries.

The motivating idea behind DBT is to reduce the so-called structure noise in 2D mammography resulting from superposition of tissues from different planes in a projection image. Tomosynthesis provided a simple means to address this issue, achievable with minimal modification to existing digital mammography systems. In DBT, X-ray projections are acquired over a small angular range, ranging from 15° to 50° depending on the system, and reconstructed to form a 3D image of the breast. Unlike CT, the resolution of this reconstruction is highly anisotropic due to the extremely limited angular span of the projections; however, the limited depth resolution attainable by this method has been shown to have significant benefits. A number of studies comparing DBT and digital mammography have concluded that, when used in conjunction with digital mammography, DBT improves the detection rate of invasive cancers while simultaneously reducing the recall rate in breast cancer screening [11–15].

1.2.2 System Geometry

The DBT configuration considered throughout this work is that of the Hologic Selenia dimensions scanner, in which the 15 X-ray projections are obtained in 1° increments over a total angular span of 15°. This geometry is shown schematically in Figure 1.2. The source rotates along the arc of a circle whose center lies in the detector plane. Planes parallel to the x-y plane are referred to as *in-plane* slices in DBT while the z direction is referred to as the depth dimension. Note, throughout this thesis, the spatial coordinates $(\mathrm{x}, \mathrm{y}, \mathrm{z})$ will be unitalicized to distinguish them from vectors. As in digital mammography, DBT can be performed in both the craniocaudal and mediolateral oblique orientations. In both cases, in-plane refers to slices parallel to the detector plane. Due to the significant depth blur of reconstructions in DBT, only in-plane slices are viewed in clinical practice.

As DBT is an X-ray projection based imaging modality, the same forward model applies

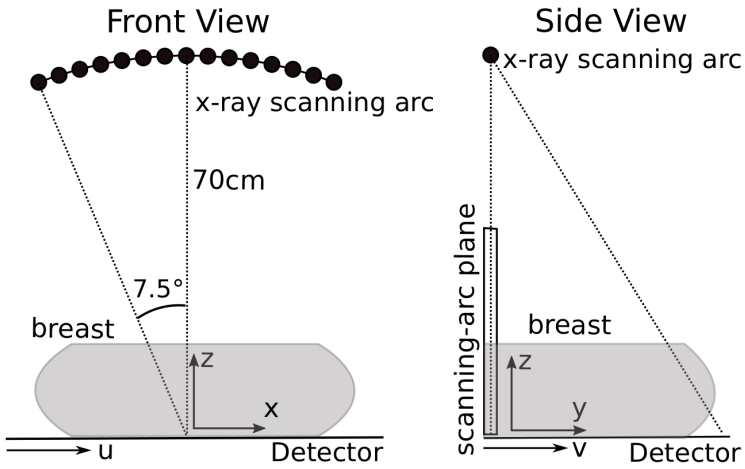

Figure 1.2: Illustration of the DBT system configuration used throughout this work. The X-ray source traverses a 15° arc with respect to isocenter, which is located in the detector plane. The scanning-arc plane is used to refer to the plane containing the X-ray source trajectory.

as in CT. The linear continuous-to-discrete forward model

$$\begin{aligned} b_i &= -\log\left(\frac{g_i}{\Lambda I_0}\right) \\ &= \int_{\Re} f(\mathbf{s}_i + t\hat{\boldsymbol{\theta}}_i)\mathrm{d}t + p_i \end{aligned}$$

still holds with the modification that the source positions $\mathbf{s}_i$ and direction vectors $\hat{\boldsymbol{\theta}}_i$ are now defined based on the system geometry shown in Figure 1.2.

1.2.3 Image Reconstruction and Artifacts

The challenge of image reconstruction in DBT is to obtain a representation of f from X-ray projection data acquired over a limited angular span. Mathematically speaking, without incorporating prior information, the measured projection data does not contain enough information to reconstruct a 3D volume with isotropic resolution. In order to do so, X-ray projections would be needed from more angles. Nevertheless, based on a wealth of experience from CT, both analytic and iterative methods have been successfully adapted to DBT. As in CT, each DBT reconstruction method involves variety of parameter and implementation

choices that can significantly impact the quality of reconstructed images; however, there is more freedom in algorithm design for DBT than in CT since one does not expect to obtain a representation of the breast possessing isotropic resolution. For example, even simple backprojection reconstruction can yield images of some utility [16, 17].

As seen in the previous section, the functional form of the imaging model in CT is identical to that in DBT. As such, image reconstruction in DBT follows largely similar approaches to those in CT. In fact, the implementation of FBP described in section 1.1.3 can be directly applied to DBT. However, the differences in angular sampling between the two modalities lead to reconstructed images of vastly different appearance. Reconstructed images in DBT tend to contain significant in and out-of-plane artifacts. This is illustrated in Figure 1.3, reprinted with permission from [18], in which FBP reconstructions of a simulated breast phantom are shown for both CT and DBT sampling schemes. The reconstructions were performed from noiseless projection data to isolate the differences arising from the truncated angular sampling in DBT.

There are two notable artifacts in the DBT reconstructions shown in Figure 1.3. The first, called “ghosting", is an out-of-plane artifact resulting from the significant depth blur of DBT reconstructions. This artifact can be visualized with the right-hand signal in the two in-plane slices of the DBT reconstruction. In slice 1, the signal is in focus, whereas in slice 2, a “ghost" of the signal, having lower intensity, is observed. From the phantom images, we see that the signal does not physically overlap with this slice. The second artifact is an in-plane artifact called overshoot and can be visualized with any of the signals in either of the in-plane slices of the DBT reconstruction. This artifact appears as a region of low intensity surrounding the edges of reconstructed signals. Note this artifact is most prominent in regions where the edge of the signal lies perpendicular to the direction of source travel (x-direction).

Research in DBT image reconstruction has largely focused on the reduction of the artifacts introduced by truncated angular sampling [19]. In analytic reconstruction, a number of

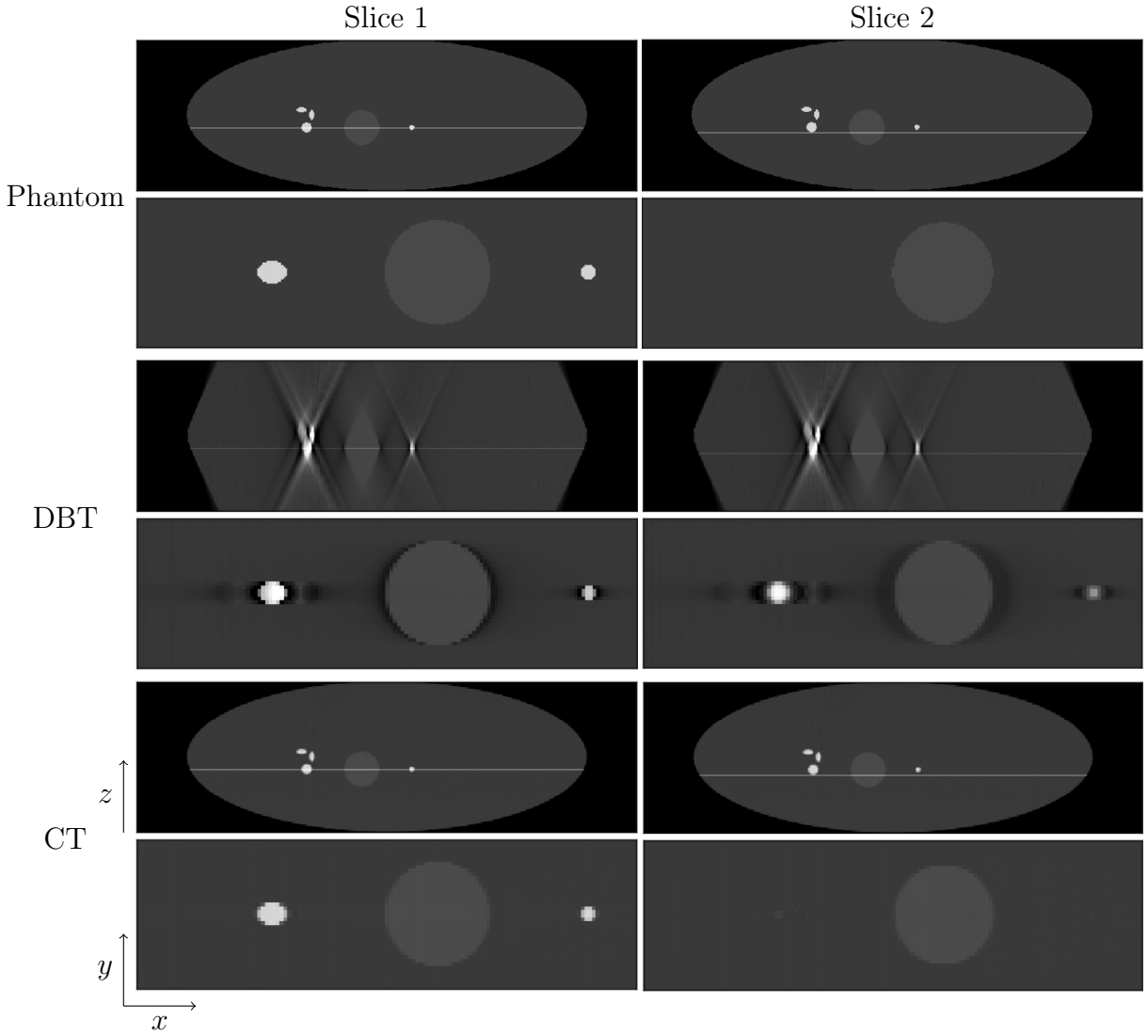

Figure 1.3: DBT and CT reconstructions of a simulated breast phantom from noiseless projection data. In-plane (x-y) slices are shown in the bottom row of each panel while coronal (x-z) slices are shown in the top row. Horizontal lines in the coronal images indicate the location of each in-plane slice. The x direction corresponds to the direction of source travel.

modifications to the ramp filter have been proposed to both reduce overshoot and improve the signal-to-noise ratio of large signals [20]. In addition, a number of iterative methods have been proposed and have shown promise for both improving conspicuity of small, high-contrast signals and reducing out-of-plane artifacts [2]. While a large number of reconstruction algorithms have now been proposed in DBT, there has been relatively little characterization of their parameter dependencies via objective image quality metrics. In chapters 4 and 5, we

attempt to address this issue, first by investigating objective, simulation-based image quality metrics for DBT, and then by applying such metrics to the characterization of reconstruction algorithms in reducing the orientation dependence of fiber-like signal conspicuity in DBT.

CHAPTER 2

INVESTIGATING IMAGE REPRESENTATION IN LINEAR ITERATIVE IMAGE RECONSTRUCTION FOR BREAST CT

2.1 Introduction

Much work over the past decade has focused on the development of optimization-based IIR methods to reduce the required dose to achieve a clinically useful reconstruction using sparse-view or low-dose acquisition schemes in X-ray computed tomography (CT) [21–28]. In addition, IIR methods have been used to incorporate realistic physics into the imaging model and their potential has been demonstrated for beam-hardening correction, metal-artifact reduction, and reconstruction from low-intensity measurements [29–31].

In optimization-based IIR, a continuous object is discretized by representing it as a linear combination of a finite number of functions in an expansion set [32]. While the most common approach is to use non-overlapping cubic voxels (3D) or square pixels (2D), other sets, such as spherically symmetric Kaiser-Bessel functions [8, 33, 34], Gaussian blobs [35], and natural pixels [36, 37] have also been investigated and each shown to have particular advantages and disadvantages. Discretization of the continuous object in any of these finite sets leads to inconsistencies between re-projections generated from the reconstructed images and noiseless projection data [38–40]. These inconsistencies are a potential source of artifacts in reconstructed images.

Perhaps the most intuitive approach to dealing with the inconsistencies introduced by discretization is to use a larger expansion set with finer spatial resolution, but this approach carries with it its own issues. Restricting our attention to the pixel expansion set, as the pixel size is decreased, the conditioning of the discrete-to-discrete imaging model deteriorates, eventually leading to artifacts in the reconstruction if proper regularization is not employed [39, 41]. While the re-projections of the reconstructed images at these small pixel sizes may better agree with the measured projection data, poor conditioning of the reconstruction

procedure may cause small inconsistencies, such as those introduced by discretization, to generate significant artifacts in the reconstruction.

In the absence of regularization, there is a pixel size dependent tradeoff between conditioning and modeling of the data that governs one's ability to obtain a reconstruction with minimal discretization artifacts. By introducing regularization, one may be able to diminish some of the effects of poor matrix conditioning and thereby use smaller pixel sizes, possibly leading to an improvement in image quality. The question then remains as to how to determine what pixel size and regularization strength should be employed. It is worth noting that the aforementioned tradeoff between conditioning and modeling will manifest itself even when reconstructing from noiseless data due to the inconsistencies introduced by discretization.

In this chapter, we perform a simulation study to characterize the effects of pixel size, regularization parameter and expansion set in IIR for breast CT. As our primary interest is the pixel-size/expansion-set dependent tradeoff between conditioning and modeling of the data, the attention in this chapter is confined to a subset of reconstruction optimization problems for which the reconstructed image can be expressed as a linear function of the data; however, we note that the methodology applied in this chapter would easily extend to an investigation of nonlinear reconstruction algorithms.

Early truncation of iterative algorithms can cause the obtained reconstruction to differ quite significantly from the accurate solution of an optimization problem, especially for poorly conditioned reconstruction problems. Here we confine our attention to accurate solution of the reconstruction optimization problem, eliminating dependence of the reconstructions on algorithm parameters such as step size and number of iterations, and allowing for direct comparison of the reconstruction optimization problems themselves.

The chapter is organized as follows. In section 2.2, we outline the general structure of the simulation studies employed in subsequent sections. In sections 2.3 and 2.4, we perform extensive studies characterizing the behavior of reconstructions as a function of pixel size,

regularization parameter, and expansion set. The studies are organized by the level of inconsistency considered between the measured data and the forward model employed by the reconstruction algorithm. In section 2.3, the data is taken to be ideal, by which we mean it is the Radon transform of a continuous object, while in section 2.4, deviations from this ideal scenario are introduced in a sequential fashion. In section 2.5 we present our conclusions.

2.2 Methods

2.2.1 Study Design

In the following, we outline an empirical simulation method for investigating pixel size, regularization parameter, projection model, and expansion set in optimization-based IIR. The idea of the method is, for a fixed data set, to compare images reconstructed in finite-dimensional expansion sets to a continuous (or high-resolution) phantom. In order to do this, one must first define the continuous phantom, which can be done by either writing down a functional form for the phantom (e.g. a superposition of ellipses) or defining the phantom on a high-resolution pixel grid. The high-resolution grid must be defined so that the the pixel size is much smaller than the detector bin size projected to midline.

Data is first generated by forward projecting the high-resolution or continuous phantom. If the phantom is defined on a high-resolution grid, this can be done with any discrete-to-discrete forward projection model, while if the phantom is defined continuously, this can be done by sampling the Radon transform of the object, assuming it can be written in closed form. Noise can also be introduced at this stage.

Reconstructions are performed from the data and resampled by nearest-neighbor interpolation onto the high-resolution grid on which the phantom is defined. If the phantom is defined continuously, it also needs to be sampled onto the high-resolution grid. The reconstructions are then compared to the high-resolution phantom via some quantitative metric.

Though a number of metrics could be used for this comparison, here the root-mean-square-error (RMSE) between the two images is employed.

This method allows for an efficient and quantitative comparison of reconstructions with different pixel sizes, regularization strengths, and image expansion sets in the presence of inconsistency between the forward model used in reconstruction and the forward model used to generate the data. Since the reconstructions are resampled onto the high-resolution grid on which the phantom is defined, the RMSE provides a measure of how well the reconstructions estimate a higher-dimensional object. This is reflective of the primary goal in CT, which is to obtain an accurate representation of a continuous object in a finite expansion set. Note that even if the same method of forward projection is used to both generate the data and perform reconstruction, the fact that the two forward models utilize different pixel sizes prevents the method from committing the so-called "inverse crime" [39, 40] in which the forward models used to generate data and reconstruct are the same.

2.2.2 System Geometry

We consider a 2D circular fan-beam geometry with 512 views and a 20cm flat-panel detector containing 512 detector bins. The source-to-detector and source-to-center distances are taken to be 150 and 100cm, respectively. The system field of view (FOV) is 13.3cm in diameter. These parameters were chosen to mimic a breast CT system. For the studies in this chapter, the high-resolution phantom was defined on a 4096×4096 dimension grid — 0.032mm pixel size — spanning the system FOV.

For IIRs employing a pixel size expansion set, we plot RMSE as a function of the reconstructed image pixel size. To aid in the interpretation of these pixel sizes, we define the relative pixel size

$$\Delta x_r = \frac{\Delta x}{\Delta u}\frac{d}{r}$$

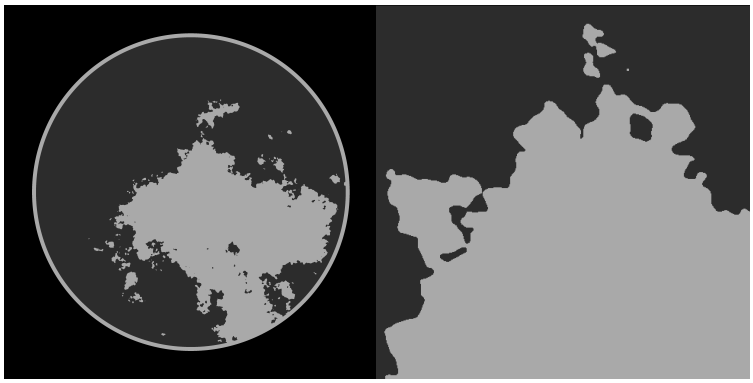

Figure 2.1: Left: High-resolution breast phantom employed for generating data and for image RMSE calculation. Right: Zoomed in ROI of phantom to be used for visualization. Display window: $[0.18, 0.26]$.

where Δx is the pixel size, Δu the detector bin size, r the radius of the source trajectory, and d the source-detector distance. A relative pixel size of 1.0 means that the detector bin size, projected to midline, is equivalent to the image pixel size.

2.3 Ideal Data

In this section we investigate the behavior of different reconstruction-optimization problems as a function of pixel size, regularization parameter, forward projection model, and expansion set under ideal conditions. By ideal it is meant that the data corresponds to the Radon transform of a high-resolution or continuously defined phantom object function. The object function considered is the high-resolution, binary breast phantom shown in Figure 2.1. The fibroglandular and fatty tissue components are taken to have attenuation coefficients of 0.233 and 0.194cm^{-1}, respectively, based on measurements at 50keV [42]. The region of interest (ROI) shown on the right of Figure 2.1 will be displayed to aid in visualization of detailed structures. For this section, the data considered was generated by forward projecting the high-resolution phantom using the ray-driven line intersection model (LI) implemented using Siddon's method [43].

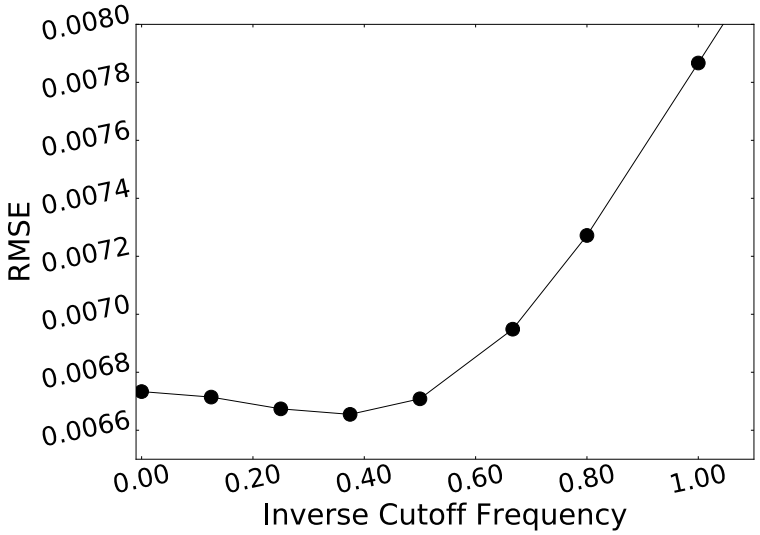

Figure 2.2: Image RMSE as a function of inverse cutoff frequency for Hanning window apodized FBP reconstructions from ideal data.

2.3.1 Least squares

The first study investigates the effect of pixel size on the solution to the unregularized least squares reconstruction optimization problem

$$\min_x \frac{1}{2}\|Ax - b\|^2 \tag{P1}$$

where $A \in \Re^{m \times n}$ is a matrix representing the forward projection operator, $x \in \Re^n$ is an image estimate, and $b \in \Re^m$ is the sinogram data. For the system geometry considered, the data is of size $m = 512^2$ while n, the size of the pixel grid, is varied. Only pixels within the system FOV are considered in the reconstruction, so the size of the image vector x is slightly less than the number of pixels in the square grid on which it is displayed. Numerically accurate solutions to this optimization problem were obtained using the conjugate gradient least squares (CGLS) algorithm [44]. Pseudocode is provided in Appendix A. In cases where $n > m$ the solution to P1 is not unique, so the minimum norm solution was reconstructed by initializing the CGLS algorithm with the zero image. The matrix A was calculated using the LI method, similarly to the data.

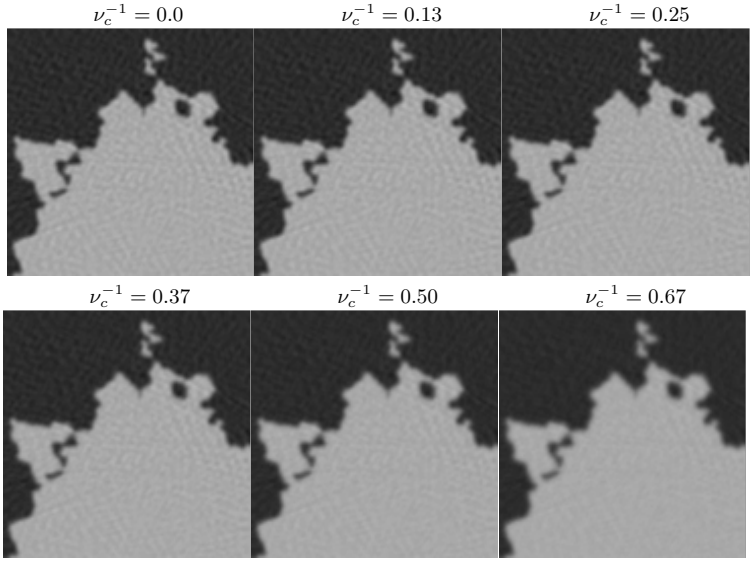

Figure 2.3: ROI of FBP reconstructions from ideal data at varying Hanning window cutoff frequencies. Regularization increases going from left to right and top to bottom. Display window: $[0.18, 0.26]$

For reference, FBP reconstructions were performed on a 1024×1024 pixel grid ($\Delta x_r = 0.5$) using Hanning windows of different cut-off frequencies $\nu_H = \nu_c/(2\Delta u)$. The RMSE curve for these reconstructions is shown in Figure 2.2. The RMSE is shown as a function of inverse cutoff frequency so that regularization increases to the right. An inverse cutoff frequency of $\nu_c^{-1} = 0.0$ is used to indicate no apodization. For the purposes of visualization, ROIs of the FBP reconstructions are shown in Figure 2.3. The RMSE curve generated from least squares reconstructions is shown in Figure 2.4, and the corresponding reconstruction ROIs are shown in Figure 2.5.

The minimum RMSE achieved among the FBP reconstructions was 6.654×10^{-3} while the lowest RMSE achieved among the least squares reconstructions was 1.097×10^{-2}. Limiting the pixel size of the least squares reconstructions to those in which the number of measurements exceeds the number of unknowns, a minimum RMSE of 1.098×10^{-2} is achieved with $\Delta x_r = 1.68$. In the RMSE sense, FBP provides clearly superior reconstructions under the conditions considered.

At relative pixel sizes above 1.68, the RMSE of the least squares reconstructions decreases

with decreasing pixel size, but a sharp increase is observed at relative pixel sizes just below 1.68. This is followed by a subsequent drop in RMSE creating a peak at relative pixel sizes around 1.00. Referring to the corresponding images in Figure 2.5, the reconstruction obtained at a relative pixel size of 1.00 is pathologically distorted, while the image at a relative pixel size of 1.19 appears noisy. In Appendix A, we investigate this behavior with a smaller system and show that these distortions result from a severe deterioration of matrix conditioning as the number of pixels n approaches the number of measurements m. For the geometry considered, this occurs at approximately a relative pixel size of 1.0. It is also seen that the drop in RMSE at relative pixel sizes less than 1.0 results from very close agreement between the LI forward model and the Radon transform when small pixel sizes are employed. We will see in section 2.4 that this drop in RMSE does not occur if the measured data is not taken to be the Radon transform of the high-resolution phantom.

The reconstructions at relative pixel sizes less than 1.0 contain structured artifacts. These artifacts, known as Moire patterns [45], result from the line-intersection method "missing" pixels in some views when the relative pixel size becomes smaller than the detector bin size. The increasing prominence of these artifacts cause the RMSE to again increase as relative pixel size is further decreased to the left of the peak.

2.3.2 Regularization for improved conditioning

Motivated by the observed increase in RMSE at relative pixel sizes near 1.0 due to deterioration of matrix conditioning, the next study considers a regularized modification of the least squares reconstruction optimization problem. The problem considered is Tikhonov regularized least squares reconstruction

$$\min_x \frac{1}{2}\|Ax - b\|^2 + \frac{1}{2}\left(\lambda\|A\|\|x\|\right)^2 \tag{P2}$$

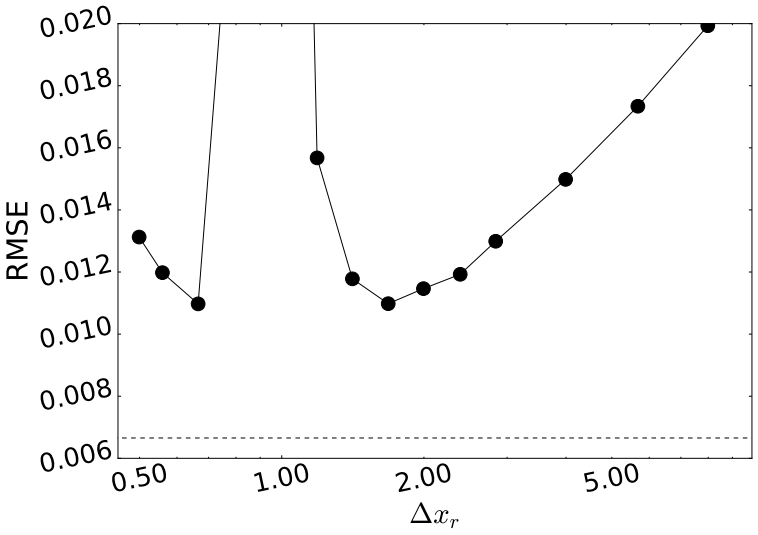

Figure 2.4: Image RMSE as a function of relative pixel size for least squares reconstructions from ideal data using the LI forward model. Horizontal line indicates minimum RMSE achieved by FBP over varying levels of Hanning window apodization.

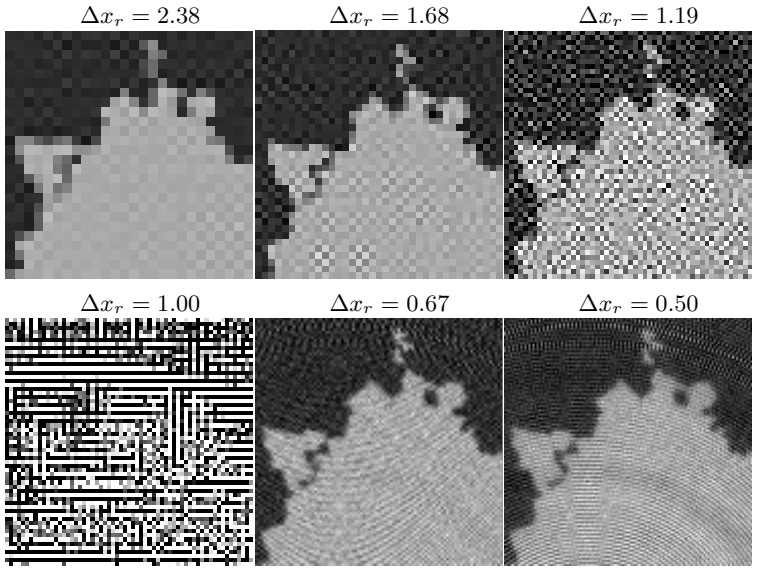

Figure 2.5: ROI of least squares reconstructions from ideal data at varying relative pixel size. Reconstructions were performed using the LI forward model. Regularization increases going from left to right and top to bottom. Display window: $[0.18, 0.26]$

where $\|A\|$ denotes the maximum singular value of A. Note that $\|A\|$ can be calculated efficiently using the power method [46]. Normalizing the regularization term in this way, the parameter λ can be interpreted as the fraction of the maximum singular value of A below which the contribution of the spectrum of A to the reconstruction is significantly diminished.

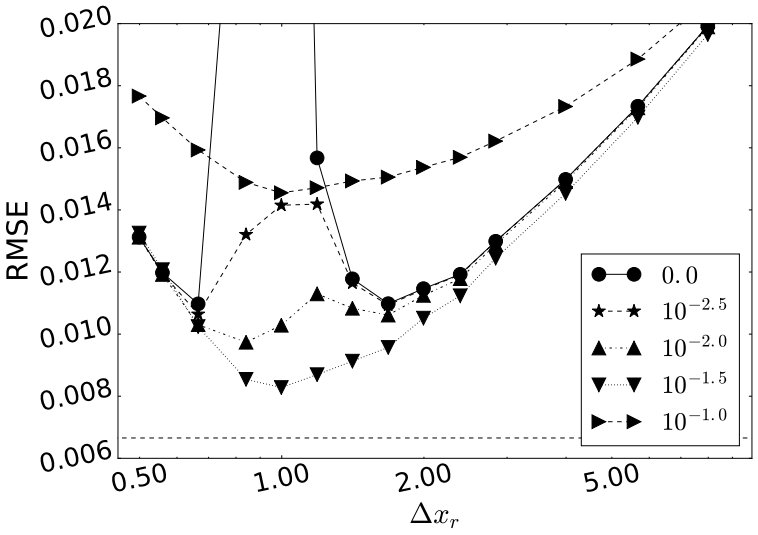

Figure 2.6: Image RMSE as a function of relative pixel size for LI-Tik reconstructions from ideal data. Horizontal line indicates minimum RMSE achieved by FBP over varying Hanning window apodization. Legend indicates value of the regularization parameter λ employed in LI-Tik reconstruction.

The optimization problem was numerically solved with the CGLS algorithm. For this study, reconstructions were again performed using the LI forward model. Tikhonov regularized least squares reconstructions employing the LI method will from here on be referred to by LI-Tik.

The RMSE curves resulting from LI-Tik reconstruction are shown in Figure 2.6 while corresponding reconstructions are shown in Figure 2.7. Referring to the RMSE curve, appropriate choice of regularization parameter allows for effective removal of the peak in the RMSE curve and the attainment of a minimum RMSE of 8.729×10^{-3} ($\lambda = 10^{-1.5}$, $\Delta x_r = 1.00$), closer to, but still larger than, the value of 6.654×10^{-3} obtained with the FBP reconstruction. The curve with $\lambda = 10^{-1.5}$ demonstrates the best behavior in terms of RMSE. Under-regularized RMSE curves continue to exhibit a similar, though less intense, peak to the unregularized curve while the over-regularized curve lies everywhere above the $\lambda = 10^{-1.5}$ curve.

The sensitivity of the RMSE to the value of λ is less at large relative pixel sizes but gains in RMSE are achievable with appropriate regularization at a relative pixel size of

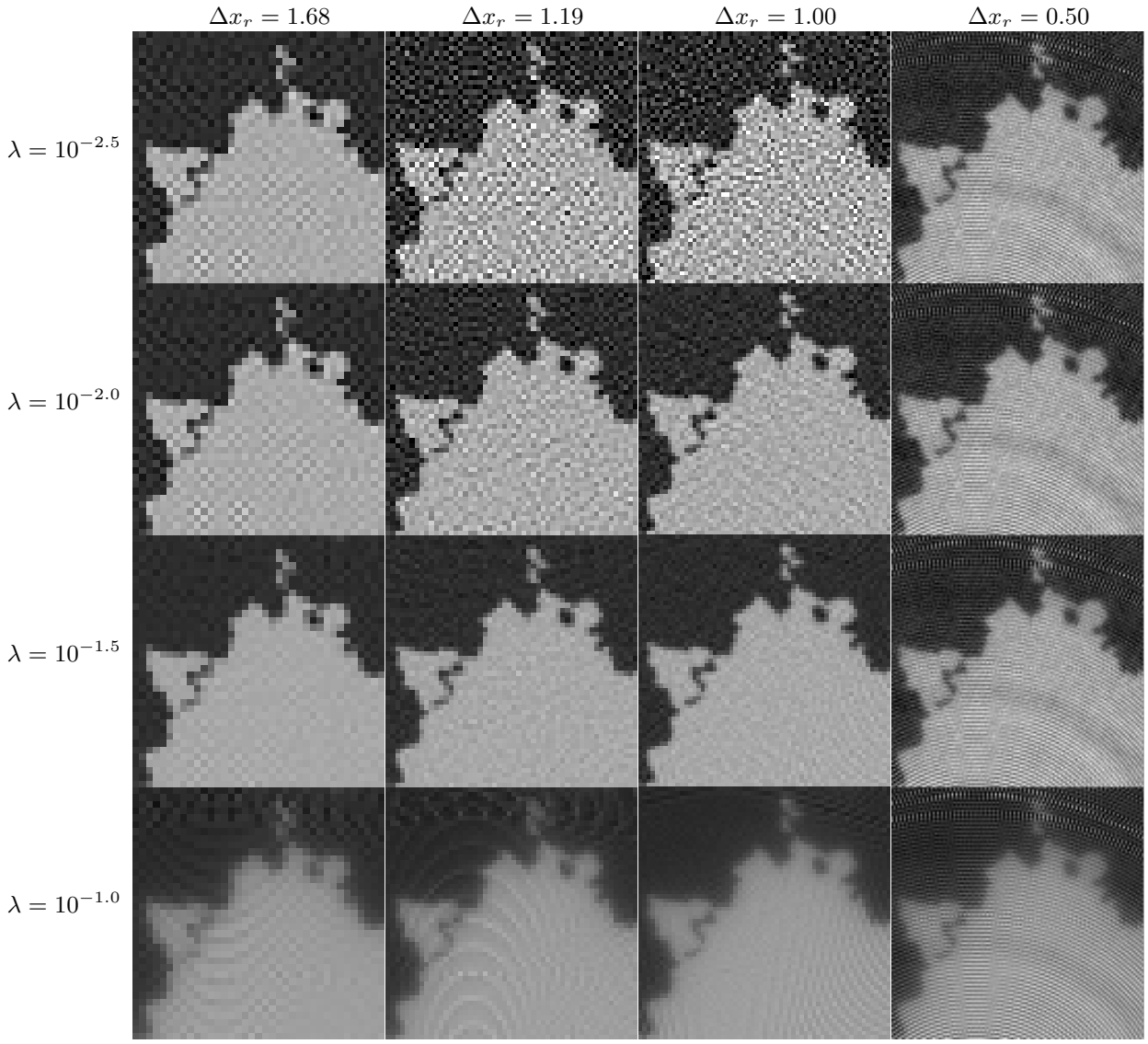

Figure 2.7: ROI of LI-Tik reconstructions from ideal data at various relative pixel sizes and regularization strengths. Relative pixel size decreases going from left to right. Regularization strength increases going from top to bottom. Display window $[0.18, 0.26]$

1.00. The trends in RMSE are reflected in the images shown in Figure 2.7. Observing the reconstructions at a relative pixel size of 1.00, one sees that increasing the level of regularization initially removes high-frequency distortions from the image before eventually lowering the mean pixel value and blurring the edges of fibroglandular structure. Moire pattern artifacts are also observed in over-regularized reconstructions and at relative pixel sizes below 1.00.

2.3.3 Forward Projection Method

To investigate whether other commonly used forward models exhibit similar behavior to the LI model, reconstructions were performed with three additional projection methods: (1) distance-driven (DD) [45], (2) Joseph's method with linear interpolation (JL) [47], and (3) Joseph's method with nearest-neighbor interpolation (JN). Tikhonov regularized least squares reconstructions using these forward models will be referred to as DD-Tik, JL-Tik, and JN-Tik, respectively. The DD method, in particular, is designed to avoid Moire pattern artifacts so we expect to observe different behavior when employing this forward model at small pixel sizes.

The resulting RMSE curves are shown in Figure 2.8. With all four projection methods, the RMSE is minimized at every relative pixel size with a regularization strength of $\lambda = 10^{-1.5}$. Sequences of reconstructions at this regularization strength are shown for each of the forward models in Figure 2.9. A $\lambda = 10^{-2.5}$ reconstruction at a relative pixel size of 1.68 is shown for each forward model to provide an approximation of the minimum RMSE unregularized reconstruction These reference reconstructions visually demonstrate the loss in potential RMSE incurred by using large enough pixel sizes to avoid poor system matrix conditioning.

Similar trends to LI-Tik are observed with both the JL-Tik and JN-Tik reconstructions. In particular, appropriate choice of regularization parameter allows for removal of the peak at relative pixel sizes near 1.00 and attainment of a lower RMSE, though still not as low as that attained by FBP. The JL-Tik, and JN-Tik reconstructions also exhibit Moire pattern artifacts at pixel sizes below 1.00, as can be seen in Figure 2.9.

The RMSE curves for the DD projector exhibit similar behavior to those of the other forward models at large pixel sizes but continue to decrease, albeit at a decreasing rate, as relative pixel size is decreased beyond 1.00. Referring to Figure 2.9, one can see that this results from the lack of Moire pattern artifacts in the DD-Tik reconstructions.

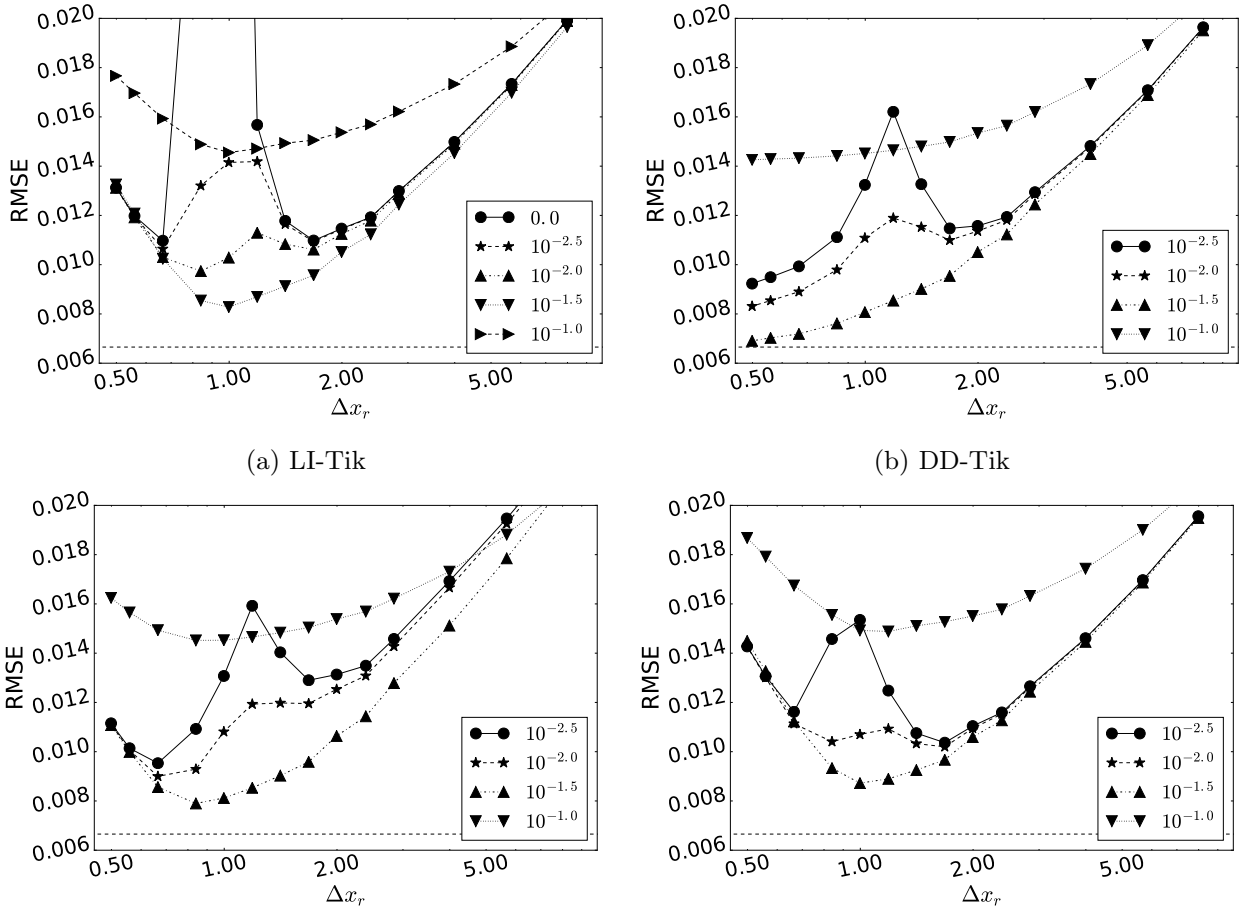

(a) LI-Tik

(b) DD-Tik

(c) JL-Tik

(d) JN-Tik

Figure 2.8: Image RMSE as a function of relative pixel size for least squares reconstructions from ideal data with Tikhonov regularization using the LI, DD, JL, and JN forward projection models. Horizontal lines indicate minimum RMSE achieved by FBP over varying levels of Hanning window apodization. Legends on each plot indicate the regularization strength λ employed in reconstruction.

2.3.4 Image Representation

To this point, none of the IIR methods have yielded an RMSE below that of the FBP reconstruction (6.654×10^{-3}). DD-Tik reconstruction was closest with a minimum RMSE of 6.908×10^{-3} using the same 1024×1024 pixel grid ($\Delta x_r = 0.50$) as FBP. The LI, JL, and JN forward models did not perform as well, each achieving minimum RMSEs near 8.000×10^{-3}. Note the improved performance of DD-Tik reconstruction is not attributable to better modeling because the LI forward projection method provides the closest approximation of the actual method by which the data was generated. This motivates us to investigate alternative

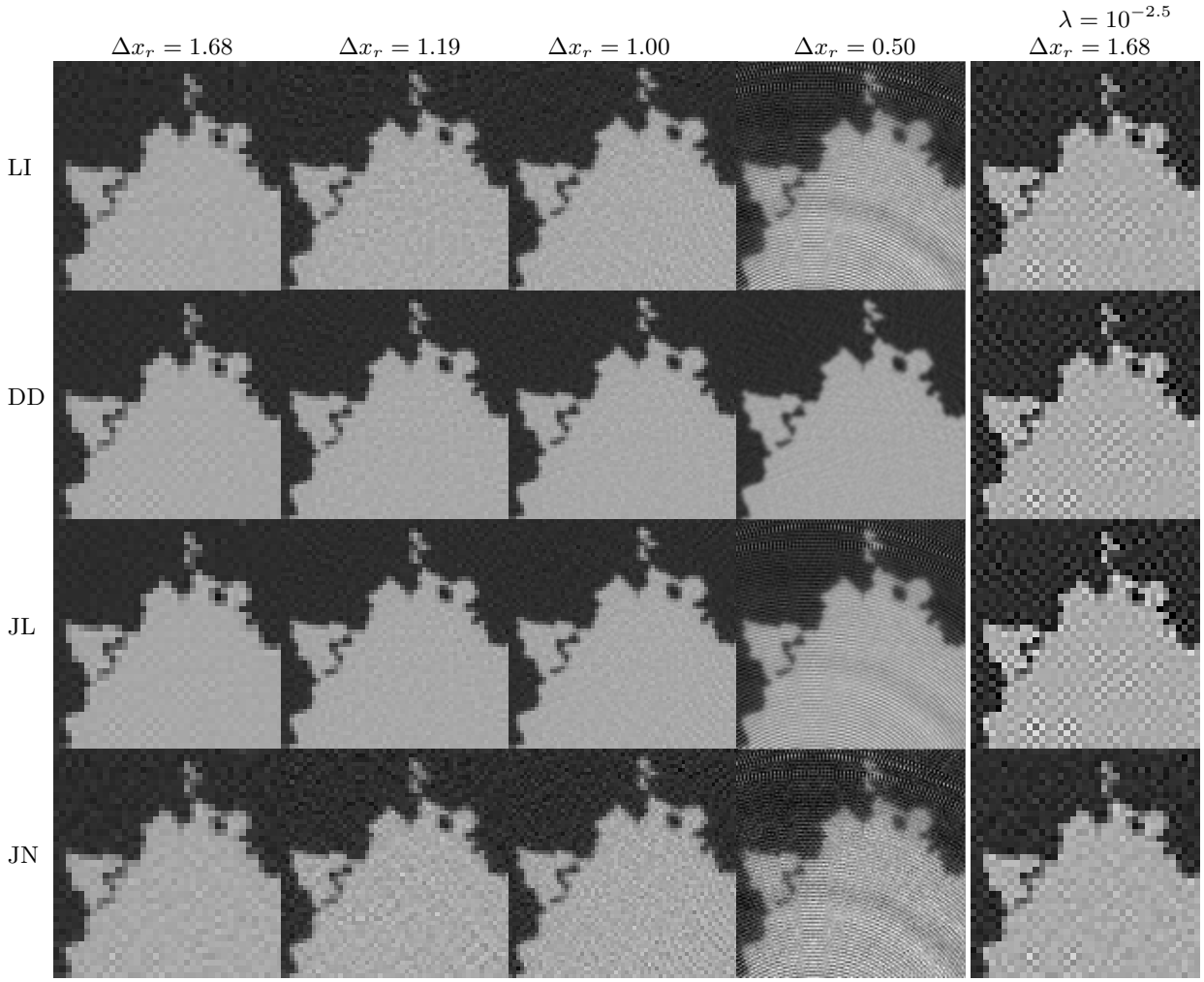

Figure 2.9: Left four columns: ROIs from Tikhonov regularized least squares reconstructions from ideal data with $\lambda = 10^{-1.5}$ using each of the four forward models. This regularization strength provides the minimum RMSE reconstruction at all relative pixel sizes for each of the forward models. Relative pixel size decreases from left to right. Rightmost column: Minimum RMSE $\lambda = 10^{-2.5}$ reconstruction ($\Delta x_r = 1.68$) for each forward model, shown to illustrate image quality at a pixel size large enough to avoid conditioning issues. Display window: $[0.18, 0.26]$

methods of avoiding Moire pattern artifacts without having to alter the forward model. To this end, in this section we investigate two different image representation schemes.

The reconstruction optimization problem for both schemes investigated in this section can be written in the form

$$\min_y \frac{1}{2}\|ARy - b\|^2 + \frac{1}{2}(\lambda\|AR\|\|y\|)^2 \tag{P3}$$

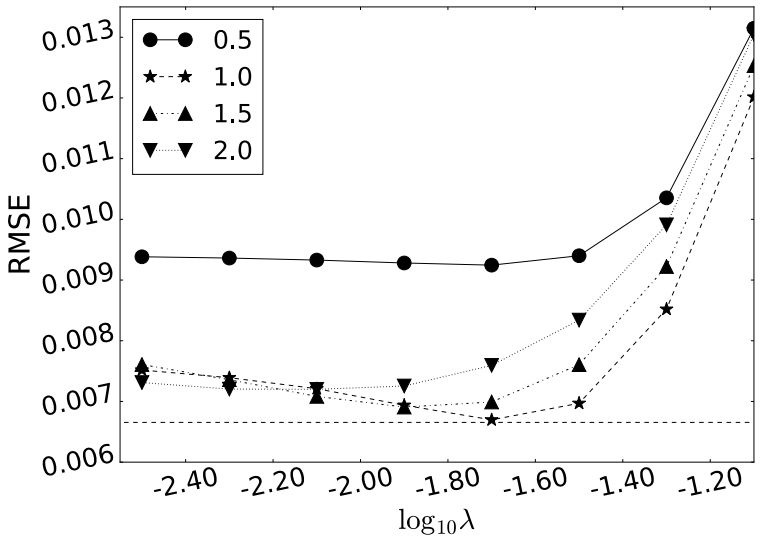

Figure 2.10: Image RMSE as a function of regularization strength for LI-Blur reconstructions from ideal data with four different values of FWHM. Legend indicates FWHM of Gaussian relative to projected detector bin width Δu_p. Horizontal line indicates minimum RMSE achieved by FBP over varying levels of Hanning window apodization.

where the columns of $R \in \Re^{p \times n}$ represent an n-element expansion set consisting of vectors defined as linear combinations of p pixels. The solution to this optimization problem yields a coefficient vector $y^* \in \Re^n$ which is then acted on by R to yield an image in $\Re^p$, the image space. Representing the image in a different expansion set, defined by the columns of R, allows one to change the conditioning of the reconstruction optimization problem. It also allows for modification of the balance between the number of unknowns n and the number of measurements m without the need to change the size of the pixel grid p. The two schemes we will investigate differ only in definition of the expansion matrix R.

The first method, referred to as the Gaussian blur model [48], takes $p = n$ — number of pixels equals number of unknowns — and defines R to be a Gaussian blurring matrix with a pre-specified full width at half maximum (FWHM). The image is thereby confined to the subspace spanned by pixelized approximations to Gaussians in the image space $\Re^p$. The second method, motivated by the natural pixel expansion set [36, 37], takes $n = m$ — number of unknowns equals number of measurements — and sets R to be a pixel driven fan-beam backprojection operator, the columns of which are pixelized approximations to

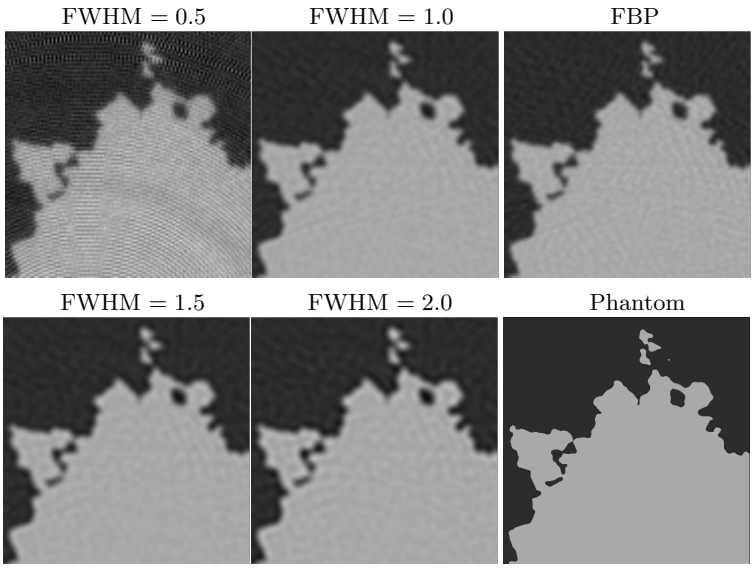

Figure 2.11: Left two columns: ROI of Minimum RMSE LI-Blur reconstructions from ideal data at each FWHM. Rightmost column: ROI of Minimum RMSE FBP reconstruction and phantom. Display window: $[0.18, 0.26]$

natural pixels in $\Re^p$. Consistent with the FBP reconstructions, p is taken to be 1024×1024 in both Gaussian blur and natural pixel reconstructions. The LI forward projection method is used to define A when using both methods. Both optimization problems are numerically solved using CGLS. For convenience, we will refer to the Gaussian blur model by LI-Blur and the natural pixel method by LI-NP.

For LI-Blur, the expansion set is varied by changing the FWHM of the Gaussian. Analogous to the relative pixel size, we specify this FWHM is specified as a fraction of the projected detector width

$$\Delta u_p = \Delta u \frac{r}{d}$$

where Δu is the detector bin width, r is the source-to-center distance, and d is the source-to-detector distance. RMSE curves are generated by varying the regularization strength at a constant FWHM.

For LI-NP, the expansion set is defined by the system geometry, so we do not vary the elements of the expansion set. To generate an RMSE curve, we vary the regularization

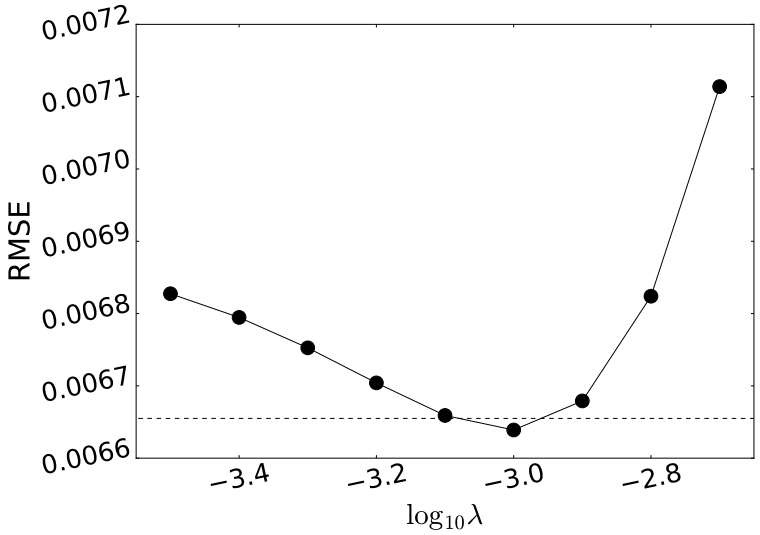

Figure 2.12: Image RMSE as a function of regularization strength for LI-NP reconstructions from ideal data. Horizontal line indicates minimum RMSE achieved by FBP over varying levels of Hanning window apodization..

strength.

RMSE curves from the LI-Blur reconstructions are shown in Figure 2.10 and reconstructed images in Figure 2.11. A minimum RMSE of 6.697×10^{-3} is achieved by the $\lambda = 10^{-1.7}$ reconstruction with FWHM = 1.0. Moire pattern artifacts are not observed in the reconstructions with FWHM greater than or equal to 1.0 and the achievable minimum RMSE is much closer to that of FBP (6.654×10^{-3}) than observed in the LI-Tik reconstructions of Figure 2.8. With a FWHM of 0.50, Moire pattern artifacts again appear. Increasing the value to 1.0, the artifacts disappear. Further increasing the FWHM begins to blur the fibroglandular structure.

The RMSE curve from the LI-NP reconstructions is displayed in Figure 2.12. Example reconstructions are shown in Figure 2.13. A minimum RMSE of $6.638 \times 10^{-3.0}$ is achieved by the $\lambda = 10^{-3.0}$ reconstruction, making LI-NP the first IIR method considered to obtain an RMSE below that of FBP.

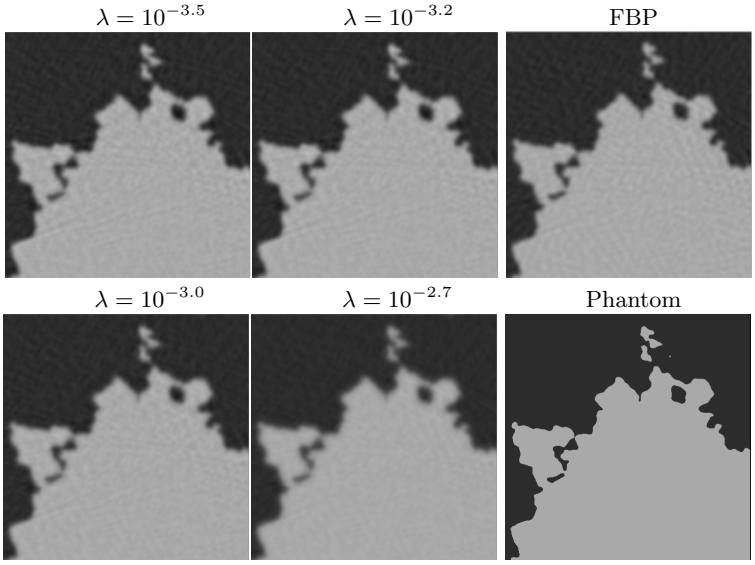

Figure 2.13: Left two columns: ROIs of LI-NP reconstructions from ideal data at varying regularization strength. Regularization increases from left to right and top to bottom. Rightmost column: ROIs of minimum RMSE FBP reconstruction and phantom.

2.3.5 Summary of investigation

An investigation of pixel size in optimization-based IIR was performed with a least squares reconstruction optimization problem in which the data was taken to be the Radon transform of a high-resolution phantom. A large increase in RMSE resulting from deterioration of system matrix conditioning was observed in unregularized RMSE curves at relative pixel sizes near 1.00. It was seen that a relative pixel size of approximately 1.68 or above would be needed to avoid such conditioning issues.

Appropriately strengthed Tikhonov regularization demonstrated the ability to mitigate the effects of deteriorating system matrix conditioning, providing reconstructions with lower RMSE at relative pixel sizes near 1.00 than achievable in the unregularized case, though a large sensitivity of the reconstruction to the regularization parameter λ was observed in this pixel size regime. Moving to lower pixel sizes, the LI-Tik, JN-Tik, and JL-Tik methods all exhibited Moire pattern artifacts. The DD-Tik method demonstrated the ability to avoid such artifacts at relative pixel sizes below 1.00. The LI-Blur and LI-NP methods both showed promise for avoiding Moire pattern artifacts without altering the forward model. The

DD-Tik, LI-Blur, and LI-NP methods were the only IIR methods considered which yielded reconstructions with RMSE comparable to that of the minimum RMSE FBP reconstruction.

2.4 Non-Ideal Data

In the previous section, the behavior of reconstructions as a function of pixel size was investigated under ideal conditions in which the data was taken to be the Radon transform of a phantom defined on a high resolution grid. In this section, to investigate the sensitivity of the previous results to changes in the model for data generation, reconstruction behavior is investigated as a function of pixel size and regularization parameter in scenarios for which the data includes components attributable to other physical factors. The section is divided into two studies. In the first study, the process of generating data is modified to account for the finite size of the detector, while in the second, contributions of Poisson noise are considered. The Tikhonov regularized least squares, LI-Blur, and LI-NP methods are then investigated to determine the effect of these changes on the previous results.

2.4.1 Finite detector width

Data was generated similarly to in section 2.3, but unlike before, 20 equally spaced rays over each detector bin were projected using the LI method and averaged to obtain noiseless data. The resulting sinogram is referred to as the finite detector bin width (FDBW) data set.

Reconstructions were performed using FBP with Hanning windows of different cut-off frequencies. The resulting RMSE curves and reconstructions are shown in Figures 2.14 and 2.15, respectively. A minimum RMSE of 7.792×10^{-3} was achieved with no Hanning window apodization.

As demonstrated in the previous section, deterioration of system matrix conditioning causes severe distortion in unregularized least squares reconstructions around relative pixel sizes of 1.00. A similar effect is expected with the finite bin width projection data so un-

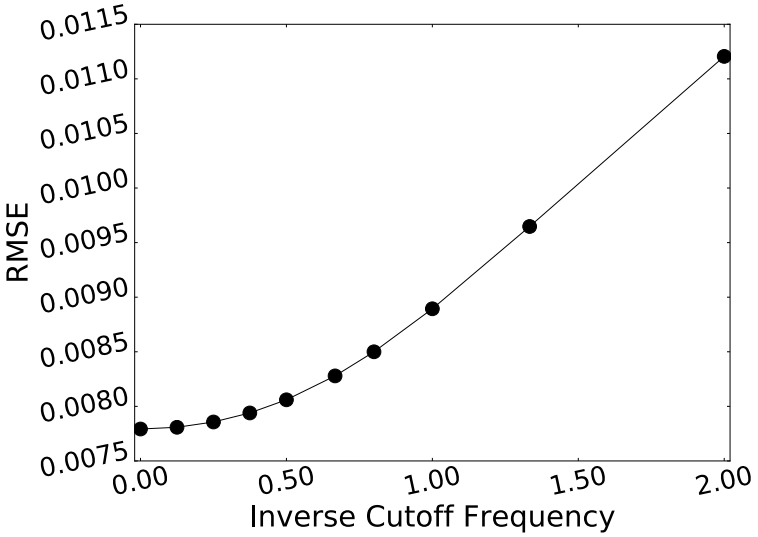

Figure 2.14: Image RMSE as a function of inverse cutoff frequency for Hanning window apodized FBP reconstructions from FDBW data.

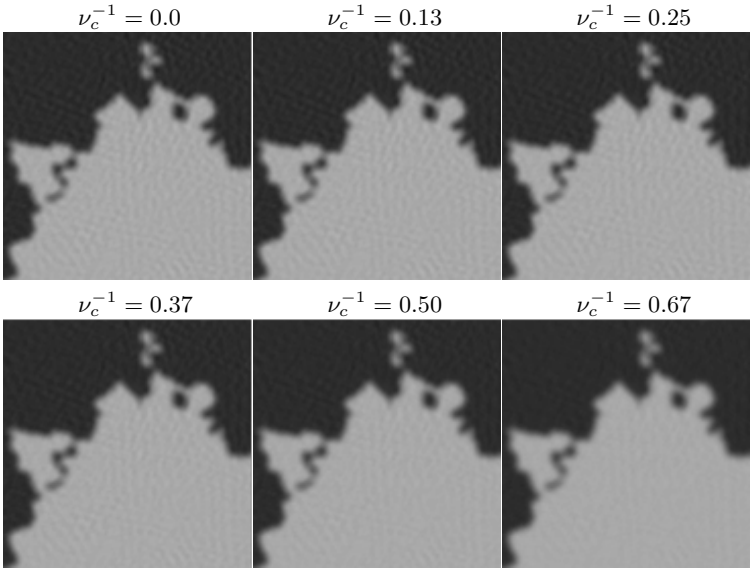

Figure 2.15: ROIs of FBP reconstructions from FDBW data at various Hanning window cutoff frequencies. Regularization strength increases going from left to right and top to bottom. Display window: $[0.18, 0.26]$

regularized reconstructions were not performed, and the investigation instead began with Tikhonov regularized least squares reconstructions utilizing the LI, DD, JL, and JN forward projectors. The resulting RMSE curves are shown in Figure 2.16.

In the minimally regularized RMSE curves ($\lambda = 10^{-2.5}$), minima are again observed in each of the curves at relative pixel sizes near $\Delta x_r = 1.68$. By contrast to the Radon

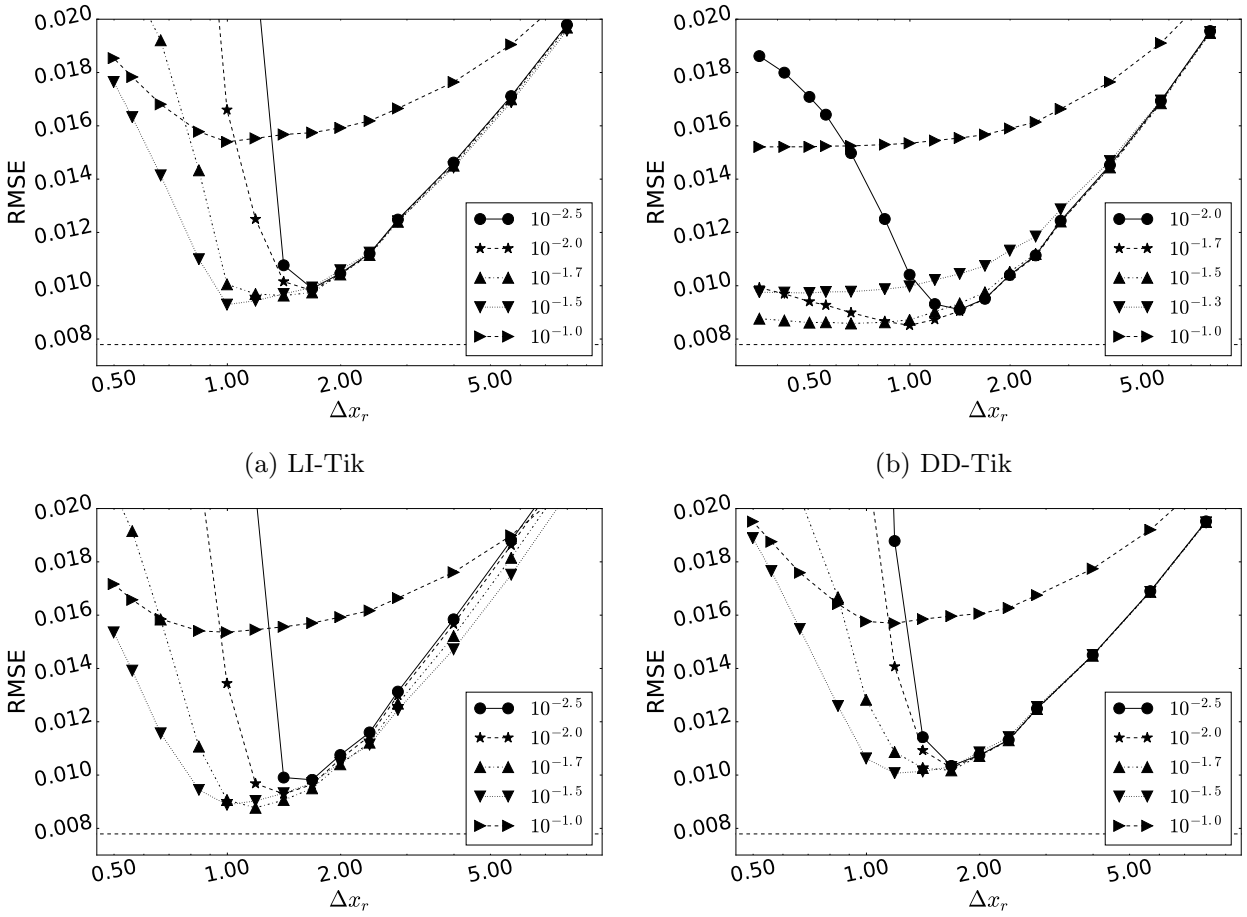

(a) LI-Tik

(b) DD-Tik

(c) JL-Tik

(d) JN-Tik

Figure 2.16: Image RMSE as a function of relative pixel size for Tikhonov regularized reconstructions from FDBW data using LI-Tik, DD-Tik, JL-Tik, and JN-Tik. Horizontal lines indicate minimum RMSE achieved by FBP over varying levels of Hanning window apodization. Legends indicate value of regularization strength λ employed in reconstruction.

transform data, no drop in RMSE is observed at relative pixel sizes below 1.00. As shown in Appendix A, the drop occurred because of the agreement between the LI projection method and the Radon transform when employing small pixel sizes. It is therefore not surprising to see the drop is no longer present.

The minimum RMSE among all of the curves shown is 8.515×10^{-3} and is achieved with DD-Tik. Note that the RMSE curves generated from the reconstructions using DD-Tik do not continue to decrease with decreasing pixel size as they did when Radon transform data was used. With the exception of the over-regularized $\lambda = 10^{-1.0}$ curve, all of the DD RMSE

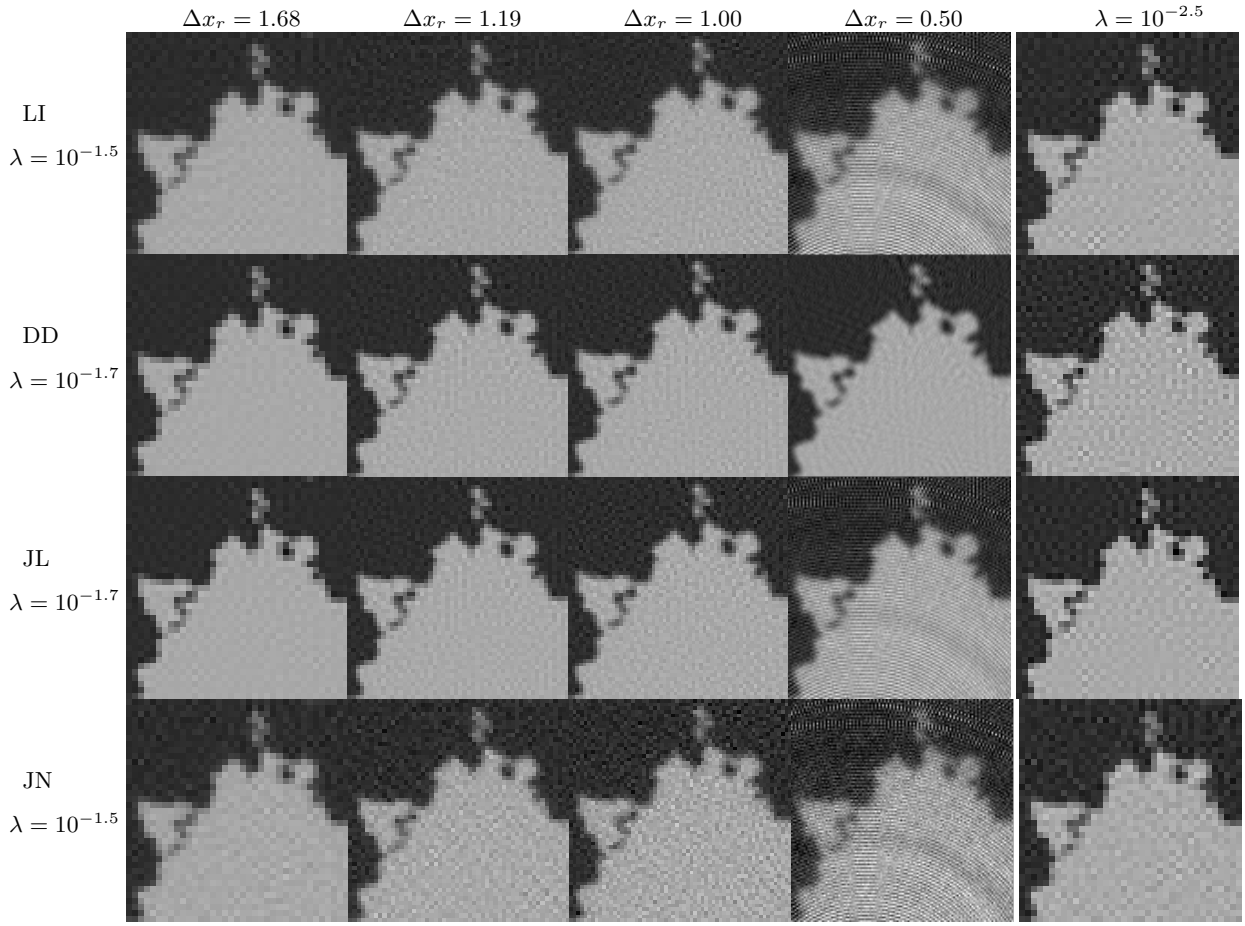

Figure 2.17: Left four columns: ROI from Tikhonov regularized least squares reconstructions of data generated using FDBW data. Each row shows reconstructions for a different forward model at the regularization strength for which that forward model achieved a minimum RMSE. Relative pixel size decreases going from left to right. Rightmost column: Minimum RMSE $\lambda = 10^{-2.5}$ reconstruction for each forward model, shown to provide a reference for image quality at pixel sizes large enough to avoid conditioning issues. Display window: $[0.18, 0.26]$

curves display a clear minimum followed by an increase in RMSE with further decrease in pixel size.

Reconstructions from each forward projection method are shown in Figure 2.17. The regularization strength for each projection method was chosen so that the minimum RMSE reconstruction for that method was included in the figure. The minimum RMSE $\lambda = 10^{-2.5}$ reconstruction for each forward model is shown for comparison. The DD-Tik reconstructions again avoid Moire pattern artifacts but exhibit some minor high-frequency artifacts that

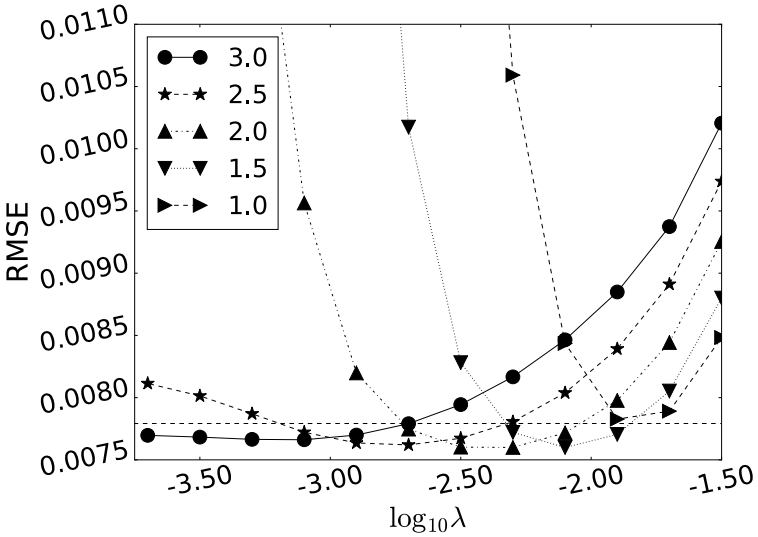

Figure 2.18: Image RMSE as a function of regularization strength for LI-Blur reconstructions from FDBW data. Legend indicates FWHM of Gaussian relative to projected detector bin width Δu_p. Horizontal line indicates minimum RMSE achieved by FBP over varying levels of Hanning window apodization.

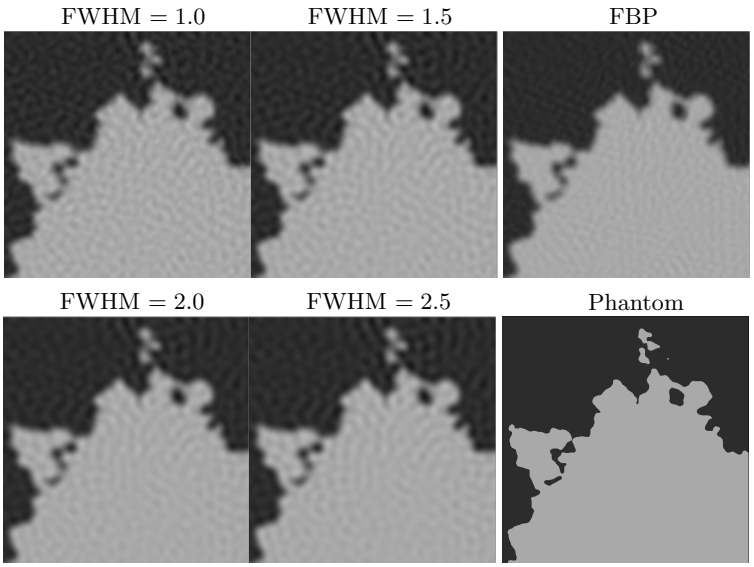

Figure 2.19: Left two columns: minimum RMSE LI-Blur reconstructions from FDBW data at each FWHM. Rightmost column: Minimum RMSE FBP reconstruction and phantom. Display window: $[0.18, 0.26]$

correlate with the observed slight increase in RMSE at small relative pixel sizes.

The LI-Blur and LI-NP reconstruction optimization problems were next investigated with the FDBW data set. The RMSE curves from the LI-Blur reconstructions are shown in Figure 2.18 along with minimum RMSE reconstructions at each FWHM in Figure 2.19. A

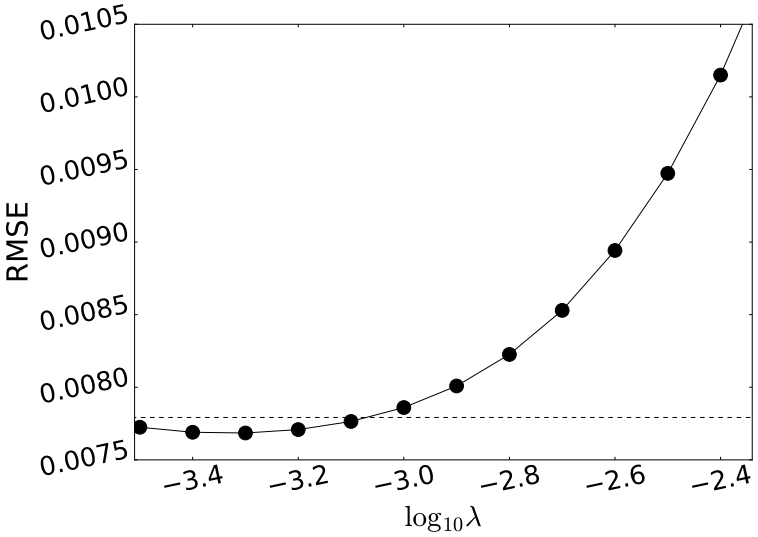

Figure 2.20: Image RMSE as a function of regularization strength for LI-NP reconstruction from FDBW data. Horizontal line indicates minimum RMSE achieved by FBP over varying levels of Hanning window apodization.

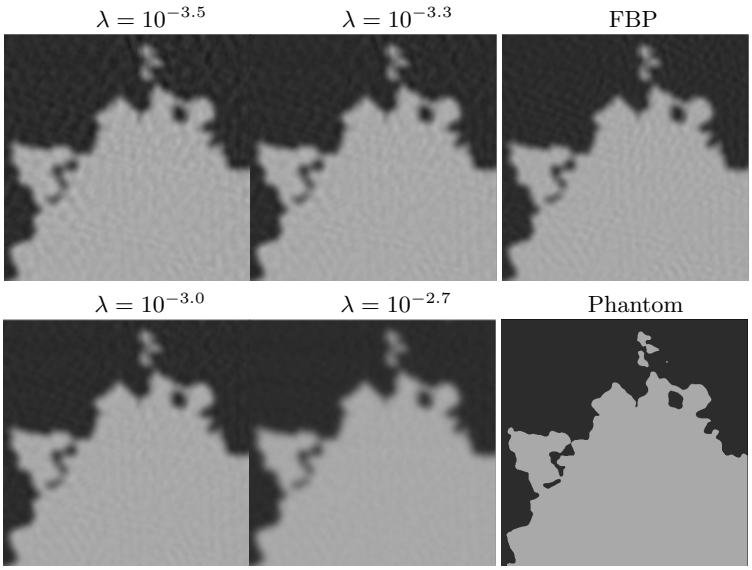

Figure 2.21: Left two columns: ROIs of LI-NP reconstructions from FDBW data at varying regularization strength. Regularization increases from left to right and top to bottom. Rightmost column: ROIs of minimum RMSE FBP reconstruction and phantom.

minimum RMSE of 7.60×10^{-3}, lower than that of FBP, is achieved with a FWHM of 2.0 and $\lambda = 10^{-2.1}$. As in section 2.3, Moire patterns are not observed in the reconstructions with FWHM greater than or equal to 1.0.

The RMSE curve for LI-NP is shown in Figure 2.20 while example reconstructions are

shown in 2.21. The minimum RMSE achieved by the LI-NP reconstructions is 7.685×10^{-3} with $\lambda = 10^{-3.4}$, also lower than that of FBP.

2.4.2 Noisy data

The next study adds further inconsistency to the data by considering Poisson noise. Forward projection of the high-resolution phantom using the FDBW model was performed to generate a mean transmission data set $\bar{g} \in \Re^m$, given by

$$\bar{g}_i = N_0 e^{-\tilde{b}_i}$$

where $\tilde{b} \in \Re^m$ is the forward projection of the high-resolution phantom, and N_0 is the number of incident photons per ray. Noisy transmission data $g \in \Re^m$ was then generated by sampling m independent Poisson random variables with means given by the elements of $\bar{g}$. Noisy sinogram data was then calculated via the equation

$$b_i = -\log \frac{\bar{g}_i}{N_0}$$

where $b \in \Re^m$ is the noisy sinogram data. Data was generated at three different noise levels with N_0 set to $10^{6.0}$, $10^{5.5}$, or $10^{5.0}$, in addition to the noiseless data set, which will be denoted with $N_0 = \infty$. RMSE curves from FBP reconstructions at each noise level are shown in Figure 2.22 and minimum RMSE reconstructions at each noise level in Figure 2.23.

Based on the result that DD-Tik achieved the minimum RMSE among Tikhonov regularized least squares reconstructions in both of the previous studies, this projection model was selected for further investigation with the noisy data. The RMSE curves resulting from reconstructions at the 4 different noise levels are shown in Figure 2.24. Observe that the minimum RMSE Tikhonov regularized least squares reconstruction at each noise level is of higher RMSE than the corresponding minimum RMSE FBP reconstruction.

At constant noise level, the RMSE curves exhibit similar patterns to those observed in the

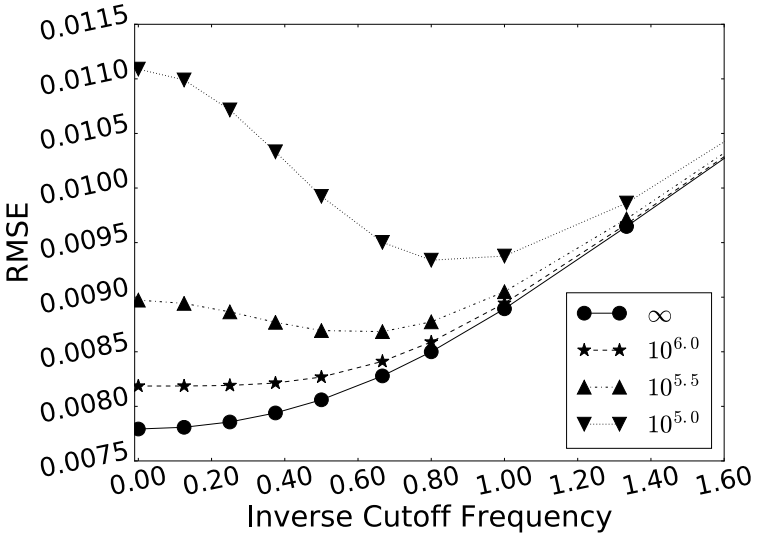

Figure 2.22: Image RMSE as a function of inverse cutoff Hanning window frequency for FBP reconstructions from FDBW data containing four different levels of noise. Legend indicates number of incident photons per ray. Noise level is increased with smaller numbers of incident photons.

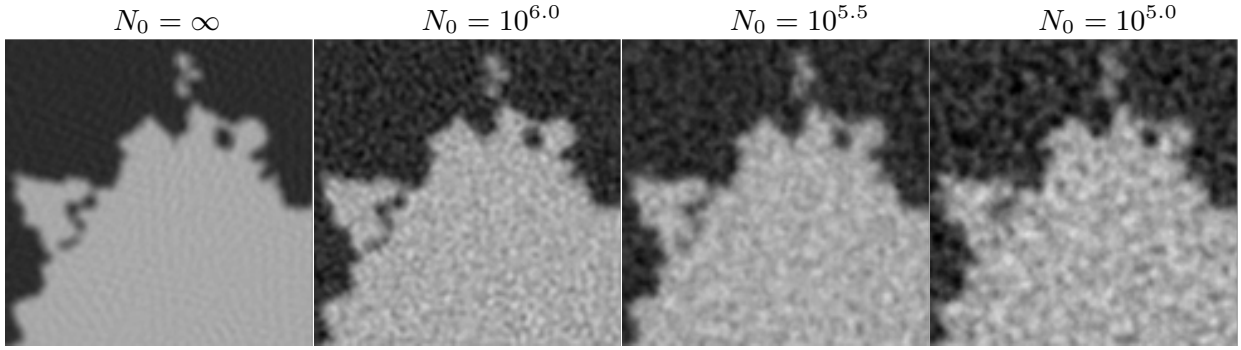

Figure 2.23: ROI of minimum RMSE FBP reconstructions from data with different noise levels. Noise level increases going from left to right. Display window: $[0.18, 0.26]$

previous two studies. If one examines only the curves of regularization strength $\lambda = 10^{-2.0}$ at each noise level, it can be seen that the point at which a minimum RMSE reconstruction is obtained shifts to larger relative pixel sizes with increasing noise. The same phenomenon can be observed in the $\lambda = 10^{-1.7}$ and $\lambda = 10^{-1.5}$ curves. If one instead considers a single relative pixel size, for instance $\Delta x_r = 1.00$, then it can be seen that the minimum RMSE is achieved with larger regularization parameters at higher noise levels. The point in the two dimensional parameter space at which the minimum RMSE is attained shifts to larger regularization parameters as noise level increases, but does not necessarily shift

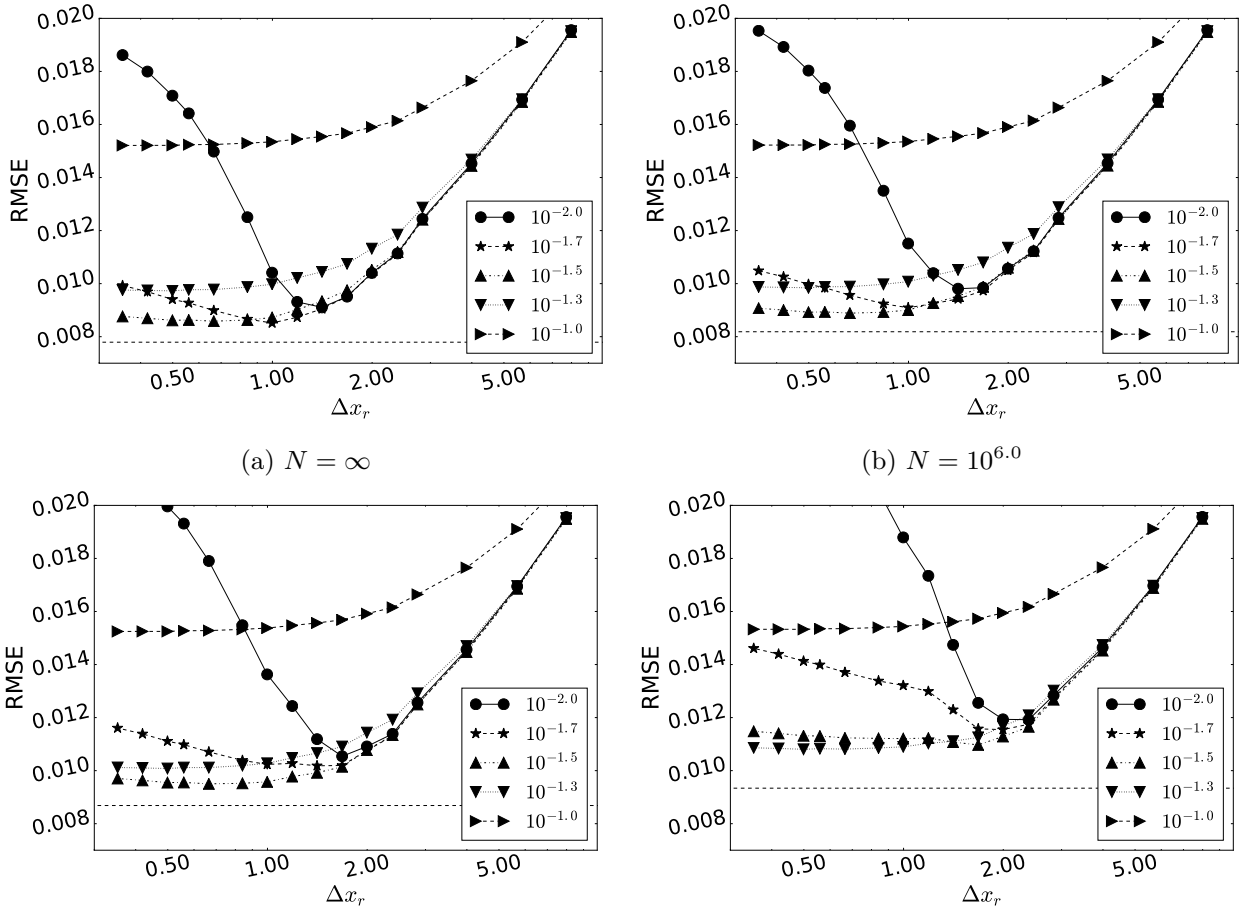

(a) $N = \infty$

(b) $N = 10^{6.0}$

(c) $N = 10^{5.5}$

(d) $N = 10^{5.0}$

Figure 2.24: Image RMSE as a function of relative pixel size for DD-Tik reconstructions from data containing four different noise levels. Legends indicate value of regularization strength λ employed in reconstruction. Horizontal lines indicate minimum RMSE achieved by FBP at each noise level.

to larger pixel sizes since the highly regularized RMSE curves tend to have broad minima around small pixel sizes. This result suggests that one could fix the relative pixel size at a value less than 1.00 and reduce the dimension of the parameter space without incurring a significant penalty in RMSE when using DD-Tik. One can also observe that as the noise level is increased, the RMSE curves corresponding to larger regularization parameters are affected less than those with smaller regularization parameters. This is particularly evident for the $\lambda = 10^{-2.0}$ curves, which are nearly identical at each noise level.

For the purposes of visualization, minimum RMSE reconstructions at each noise level from FBP and DD-Tik are shown in Figure 2.25. In addition, minimum RMSE reconstruc-

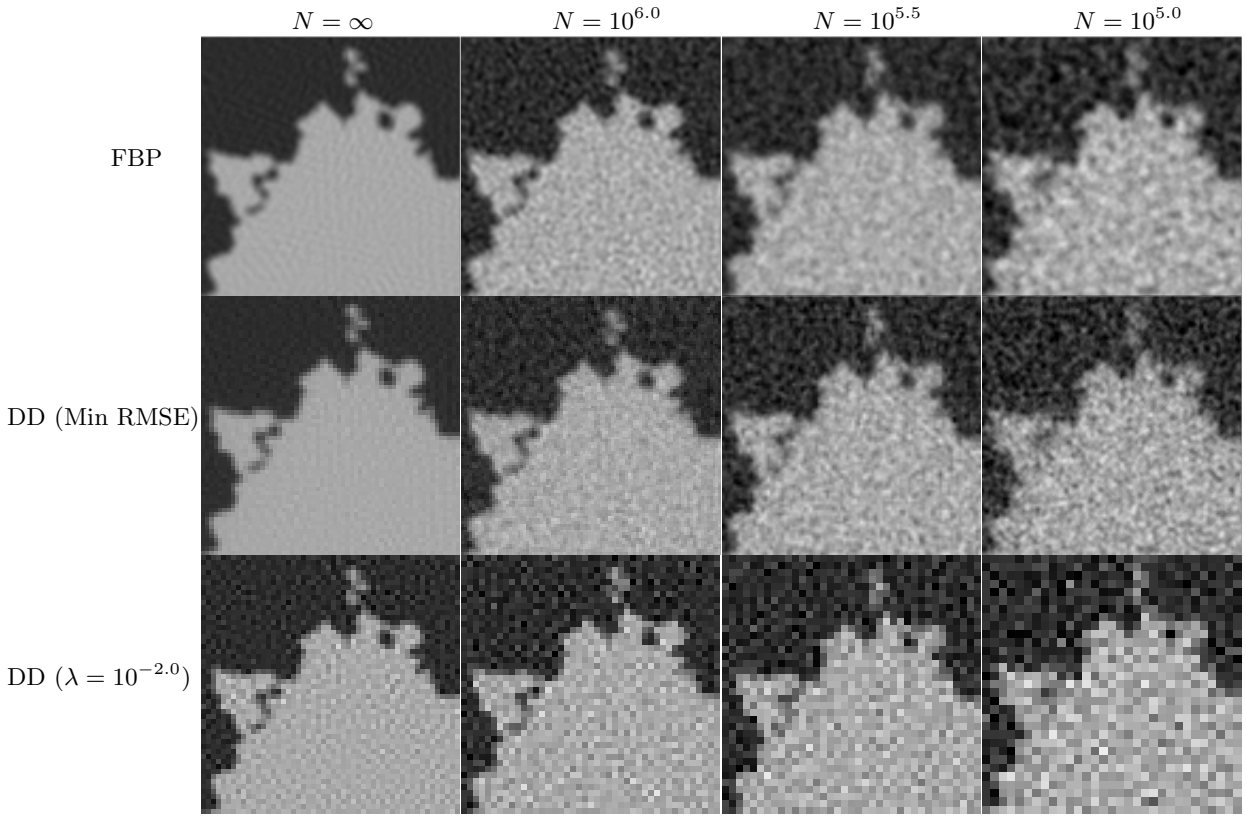

Figure 2.25: Top row: Minimum RMSE FBP reconstructions at each noise level. Middle row: Minimum RMSE DD-Tik reconstructions at each noise level. Bottom row: Minimum RMSE DD-Tik reconstructions with $\lambda = 10^{-2.0}$ at each noise level. Display window: $[0.18, 0.26]$

tions from DD-Tik reconstructions with $\lambda = 10^{-2.0}$ are shown to demonstrate the visual implications of the potential loss in RMSE from using larger pixel sizes to avoid conditioning issues. Note that the minimum RMSE $\lambda = 10^{-2.0}$ reconstructions become more pixelated as noise level increases since the minima lie at larger pixel sizes.

The effect of noise on LI-Blur reconstruction was next investigated. RMSE curves generated with LI-Blur are shown in Figure 2.26. Unlike the DD-Tik reconstructions, the minimum RMSE LI-Blur reconstructions at each noise level achieve a lower RMSE than the FBP reconstructions. As the noise level is increased, the minimum RMSE is achieved using a larger FWHM. The minimum in each curve of constant FWHM is achieved at larger values of λ as the FWHM is decreased.

Minimum RMSE LI-Blur reconstructions at each noise level are shown in Figure 2.27

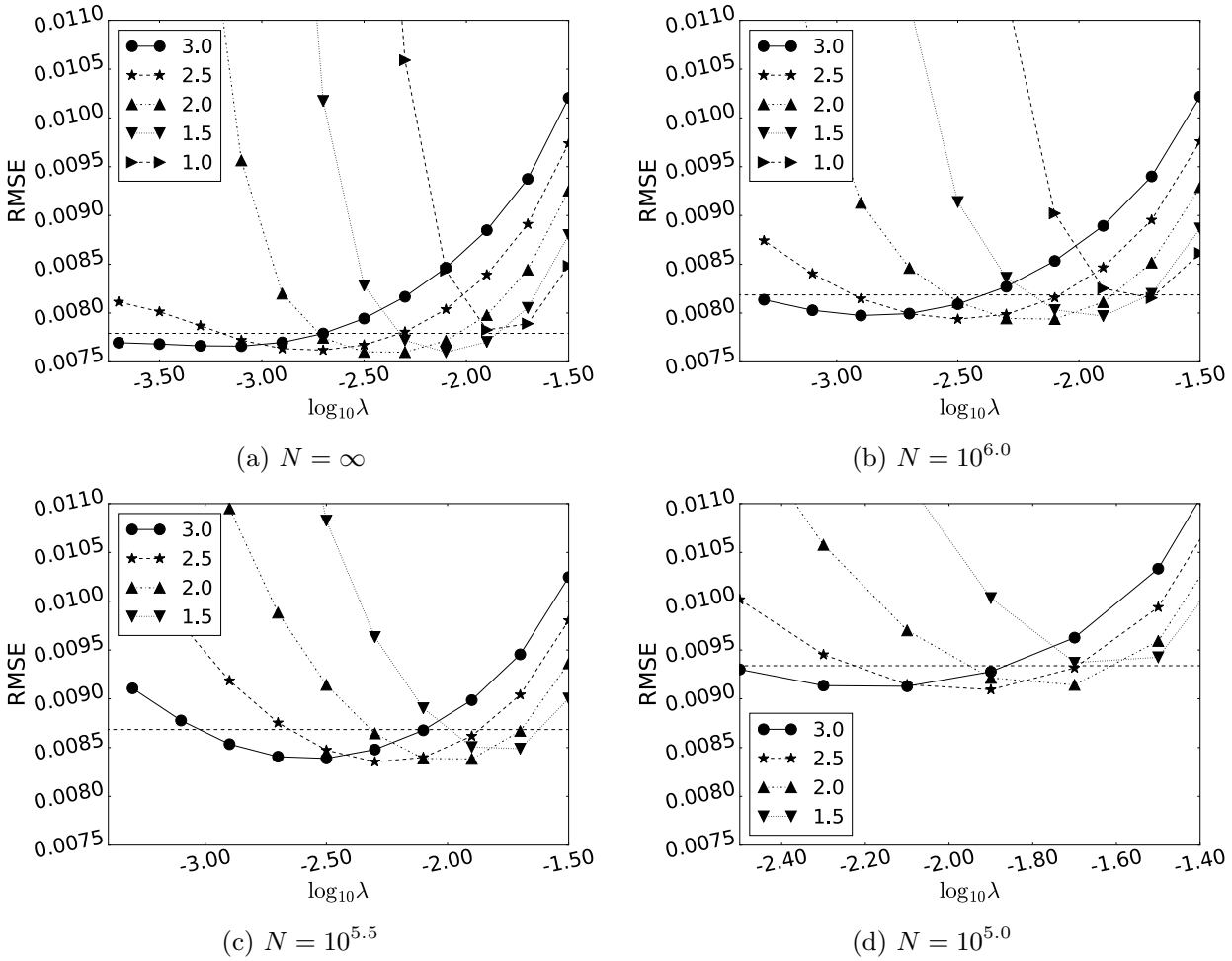

(a) $N = \infty$

(b) $N = 10^{6.0}$

(c) $N = 10^{5.5}$

(d) $N = 10^{5.0}$

Figure 2.26: Image RMSE as a function of regularization strength for LI-Blur reconstructions from data containing four different noise levels. Legends indicate value of FWHM relative to projected detector bin-width Δu_p. Horizontal lines indicate minimum RMSE achieved by FBP at each noise level.

alongside the minimum RMSE FBP reconstructions. Higher frequency texture is observable in the noiseless and $N = 10^{6.0}$ reconstructions, while only lower frequency texture is seen in the $N = 10^{5.5}$ and $N = 10^{5.0}$ reconstructions. This is a result of the fact that the minimum RMSE reconstruction moves to larger values of FWHM as the noise level is increased. Though not shown here, the Gaussian blur reconstructions continue to exhibit Moire pattern artifacts if a FWHM below 1.00 is employed.

The noise properties of the LI-NP formulation were next investigated. The RMSE curves at each noise level are shown in Figure 2.28. The minimum RMSE reconstructions at the

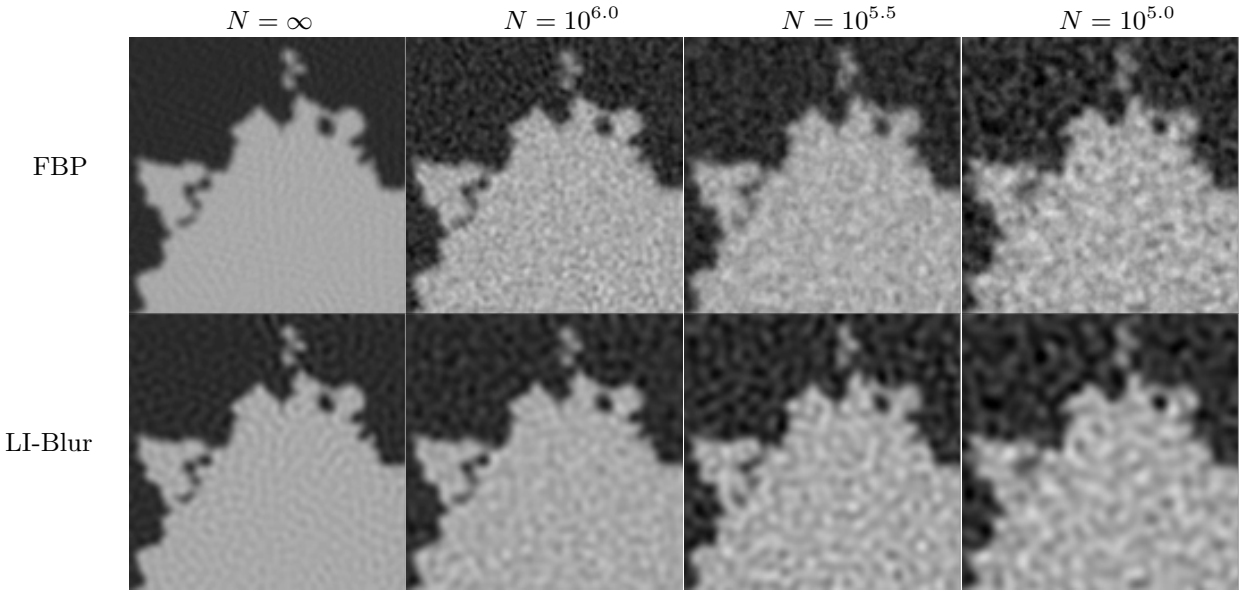

Figure 2.27: Top row: Minimum RMSE FBP reconstruction at each noise level. Bottom row: Minimum RMSE LI-Blur reconstruction at each noise level. Display window: $[0.18, 0.26]$

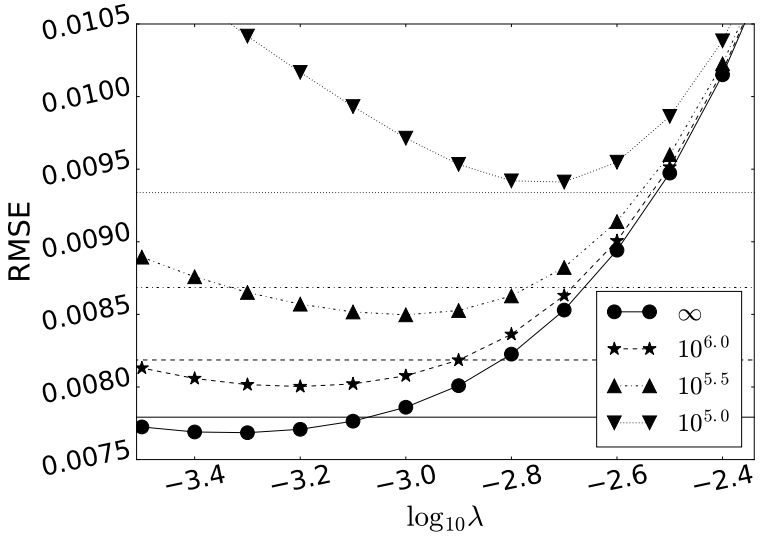

Figure 2.28: Image RMSE as a function of regularization strength for LI-NP reconstructions from data containing four different noise levels. Legend indicates number of incident photons per ray. Noise level increases as number of incident photons decreases. Horizontal lines indicate minimum RMSE achieved by FBP at each noise level.

three lowest noise levels achieve RMSEs slightly lower than the FBP reconstructions. As the noise level is increased, the level of regularization at which the minimum is achieved increases, similar to our previous observations with DD-Tik.

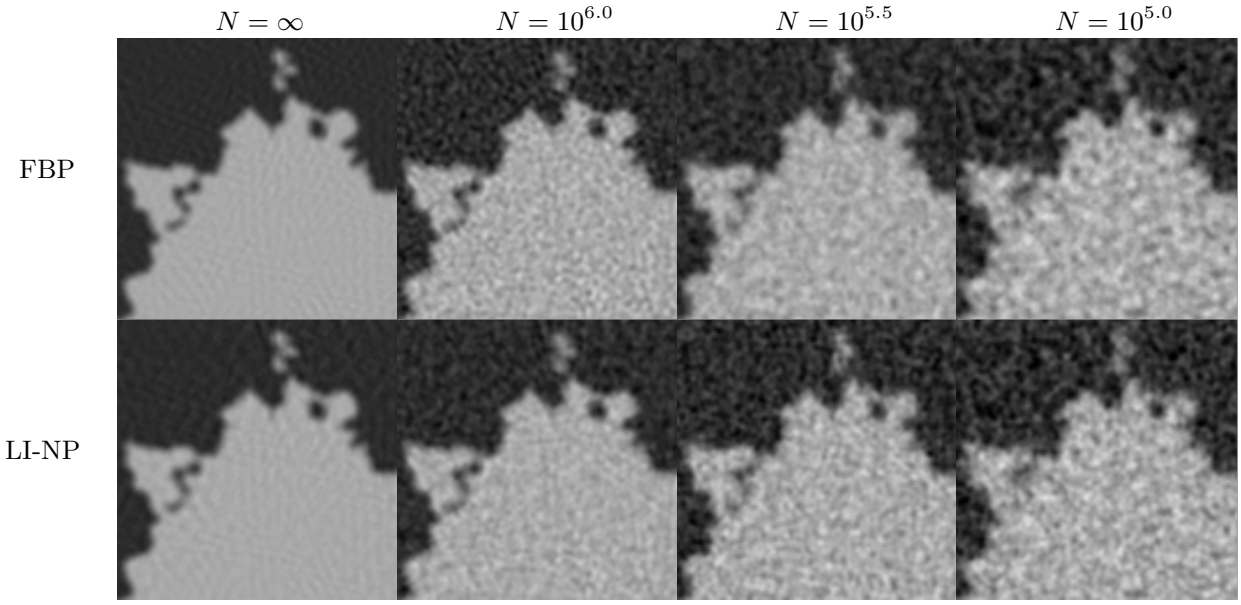

Figure 2.29: Top row: Minimum RMSE FBP reconstruction at each noise level. Bottom row: Minimum RMSE LI-NP reconstruction at each noise level. Display window: $[0.18, 0.26]$

Minimum RMSE LI-NP reconstructions at each noise level are shown in Figure 2.29. As the noise level is increased, the appropriate level of regularization for LI-NP is increased making the reconstructions slightly blurrier.

2.4.3 Summary

To investigate how non-ideal data affects reconstruction behavior as a function of pixel size and regularization parameter, two studies were performed with data generated using a forward model accounting for finite detector bin width. In the first study, Tikhonov regularized least squares reconstructions were performed from noiseless data with four different forward models. Similar trends were observed to the case of Radon transform data in section 2.3. In particular, it was seen that each reconstruction method was less sensitive to regularization parameter at large pixel sizes, but that potential gains in RMSE could be achieved with appropriate choice of regularization parameter and use of a smaller pixel size. The DD-Tik method outperformed the other forward models investigated with regards to minimizing the image RMSE but did not achieve as low an RMSE as FBP. The LI-Blur and LI-NP formu-

lations were both able to achieve a minimum RMSE below that of FBP but exhibited very different textures.

In the second study, the effect of noise on the behavior of reconstructions as a function of image representation and regularization parameter was investigated. At each individual noise level, similar trends were observed in the RMSE curves as in the noiseless case. The appropriate level of regularization for DD-Tik reconstruction increased with increasing noise level, while the appropriate choice of pixel size did not display a clear correlation with the noise level. If attention was limited to a single level of regularization, the appropriate choice of pixel size increased with increasing noise level. The DD-Tik reconstructions were not able to achieve as low an RMSE as FBP at any noise level. The LI-Blur reconstructions achieved a minimum RMSE below that of FBP at every noise level while the LI-NP reconstructions achieved a minimum RMSE below FBP at the three lowest noise levels. For the LI-Blur reconstructions, it was found that the appropriate choice of FWHM increased with increasing noise level. For the LI-NP reconstructions, the appropriate level of regularization increased with increasing noise level.

2.5 Conclusions

In this work, we performed an investigation of pixel size, regularization strength, image representation, and projection model in IIR for breast CT. From the results of the studies we can make the following conclusions: (1) the conditioning of the system matrix, regardless of discrete forward model (among reasonable CT forward models), deteriorates rapidly as the number of pixels approaches the number of detector bins ($\Delta x_r = 1.0$ in the geometry considered) leading to severe distortion in unregularized least squares reconstructions, (2) smaller pixel sizes can be used with appropriate levels of Tikhonov regularization to achieve a further decrease in RMSE compared to unregularized reconstruction but sensitivity to the regularization parameter is more pronounced at these pixel sizes, (3) Moire pattern artifacts in reconstructions at small pixel sizes can be avoided with the DD forward model or by

maintaining the same forward model but changing image representation using the LI-NP and LI-Blur formulations, and (4) as noise level is increased, the appropriate level of regularization increases — in particular, it is appropriate to maintain a small pixel size while increasing the regularization parameter using the DD-Tik reconstruction method. Furthermore, it was found that FBP yielded images of lower RMSE than LI-Tik, JL-Tik, JN-Tik, and DD-Tik in all the scenarios considered, while the LI-NP and LI-Blur formulations yielded reconstructions of comparable or better RMSE than FBP. We stress that these results are specific to the sampling conditions and phantom investigated. A significant change in phantom — for example to an object containing only structures on the scale of two detector bin-widths or greater — could have a large impact on the appropriate choice of regularization parameter and image representation.

It is worth emphasizing that all of the reconstructions shown in this chapter were run to numerical convergence. This means that the results shown here will not in general apply to algorithms meant to solve the same optimization problems but truncated at early iteration. Early truncation adds an extra level of regularization dependent on algorithm parameters that is in no way dependent on the parameters in the reconstruction optimization problem itself. The point of the studies shown here was to probe the space of solutions to the reconstruction optimization problems considered as parameters were varied. This yielded insights into the tradeoff between image representation and system matrix conditioning that would be more difficult to interpret in the presence of variation due to algorithm parameters.

Appendix A: Algorithm Pseudo-code

In this section, we provide pseudo-code for the two implementations of CGLS used throughout this chapter. Algorithm 1 demonstrates how to implement CGLS for unregularized least squares. Note that recurring the residual $r = b - Ax$ as in the algorithm presented here is important for reasons related to numerical stability [44]. Other implementations in which $s = A^T(b - Ax)$ is recurred instead can lead to stability issues. To implement CGLS for the

Gaussian blur or natural pixel methods, one simply needs to replace A with AR everywhere in the algorithm.

Algorithm 1 CGLS

Initialize x^0 to zero
$r^0 \leftarrow Ax^0 - b; \quad s^0 \leftarrow A^T r^0; \quad p^0 \leftarrow s^0; \quad \gamma^0 \leftarrow \|s^0\|^2;$
for $k < k_{max}$ **do**
$q^k \leftarrow Ap^k$
$\alpha^k \leftarrow \frac{(p^k)^T s^k}{\|q^k\|^2}$
$x^{k+1} \leftarrow x^k + \alpha^k p^k$
$r^{k+1} \leftarrow r^k - \alpha^k q^k$
$s^{k+1} \leftarrow A^T r^{k+1}$
$\gamma^{k+1} \leftarrow \|s^{k+1}\|^2$
$\beta^k \leftarrow \frac{\gamma^{k+1}}{\gamma^k}$
$p^{k+1} \leftarrow s^{k+1} + \beta^k p^k$
end for

Algorithm 2 shows the minor modification to CGLS needed to adapt it to Tikhonov regularization. The modification occurs in the update of the normal equations residual s^k and the step size α^k.

Algorithm 2 CGLS for Tikhonov Regularization

Initialize x^0 to zero
$r^0 \leftarrow Ax^0 - b; \quad s^0 \leftarrow A^T r^0 - \lambda^2 \|A\|^2 x^0; \quad p^0 \leftarrow s^0; \quad \gamma^0 \leftarrow \|s^0\|^2;$
for $k < k_{max}$ **do**
$q^k \leftarrow Ap^k$
$\alpha^k \leftarrow \frac{(p^k)^T s^k}{\|q^k\|^2 + \lambda^2 \|A\|^2 \|p^k\|^2}$
$x^{k+1} \leftarrow x^k + \alpha^k p^k$
$r^{k+1} \leftarrow r^k - \alpha^k q^k$
$s^{k+1} \leftarrow A^T r^{k+1} - \lambda^2 \|A\|^2 x^{k+1}$
$\gamma^{k+1} \leftarrow \|s^{k+1}\|^2$
$\beta^k \leftarrow \frac{\gamma^{k+1}}{\gamma^k}$
$p^{k+1} \leftarrow s^{k+1} + \beta^k p^k$
end for

Appendix B: Investigation of Matrix Conditioning

Here we perform a study to further investigate the cause of the peak in RMSE observed in the least squares RMSE curve shown in Figure 2.4. Region-of-interest (ROI) reconstructions of a small disk phantom of radius 0.13cm were performed. In this study only a subset of detector bins, namely those which measure rays passing through the ROI, were used for reconstruction. All views were still considered. By confining focus to a small ROI, the size of the system matrix in the reconstruction optimization problem is reduced, allowing one to calculate the SVD by direct methods. Since the disk phantom has a closed form Radon transform, noiseless data was generated by sampling this expression instead of approximating it via high-resolution forward projection.

Reconstructions were performed by applying the pseudo-inverse, as calculated from the SVD, to the noiseless data. RMSE curves were generated by comparing the reconstructions to a high-resolution sampling of the disk phantom (pixel size 1.3×10^{-4}cm), and the results were compared to the singular value spectra of the system matrices at each pixel size. The condition number, defined as

$$\kappa(A^{\dagger}) = \|A\|\|A^{\dagger}\|$$

was employed as a quantitative metric of the system matrix conditioning at each pixel size. Note this definition of the condition number generalizes to the case where there are more unknowns (n) than measurements (m),and characterizes the minimum norm solution of the least squares optimization problem.

In order to investigate dependence of the RMSE curves and matrix conditioning on ROI size, four different ROIs were considered, intersecting 6, 8, 10, or 12 rays per view (1.56, 2.08, 2.60, and 3.12mm in diameter, respectively). The ROIs were positioned 3.5cm off-axis to avoid nearly overlapping rays from opposing views. The resulting RMSE curves are plotted in Figure 2.30 along with the condition number as a function of relative pixel size. A series

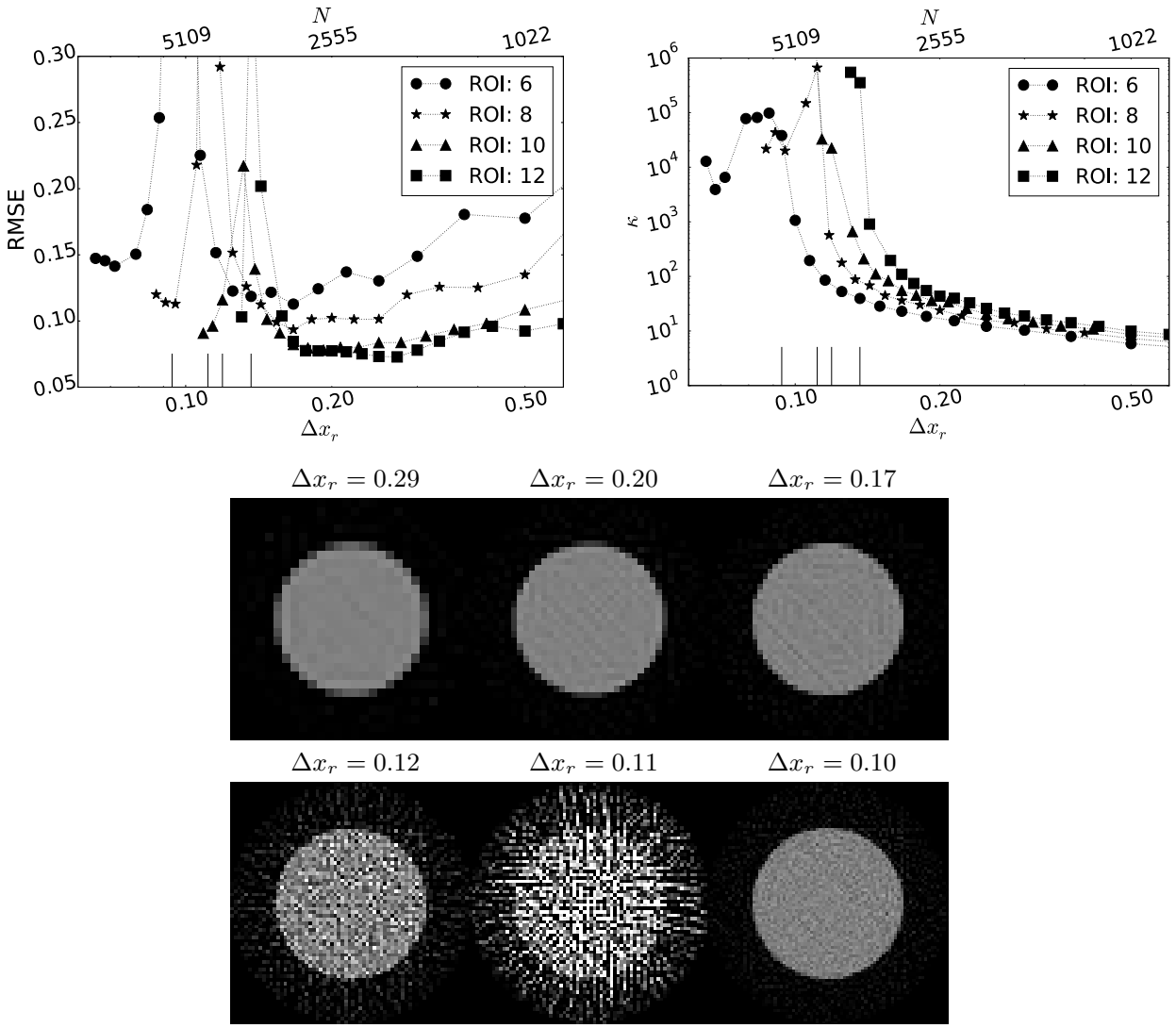

Figure 2.30: Top Left: RMSE curves from least squares reconstructions with different ROIs. Top Right: Condition number as a function of pixel size for different ROIs. Legends denote ROI size in terms of the number of rays per view intersected by the ROI. Large ticks on bottom axis indicate the relative pixel size in which the number of unknowns n is equal to the number of measurements m (going left to right they correspond to increasing ROI sizes). Bottom: Reconstructions of disk phantom for the 8 rays per view ROI. Display window: $[0.0, 2.0]$

of disk phantom reconstructions is also included.

The trends in the ROI RMSE curves are similar to those observed for the full FOV breast phantom reconstructions, though the peak RMSE occurs at much smaller relative pixel sizes. The peak always occurs approximately at the point where the number of unknowns n is equal to the number of measurements m. As the ROI size is increased, the number of unknowns

for a given relative pixel size increases, so the peak shifts to larger relative pixel sizes.

The location the sharp increase in RMSE curves correlates well with a severe deterioration of condition number as the relative pixel size is decreased to the point where the number of unknowns equals the number of measurements. This suggests the increase in RMSE in the full FOV reconstructions is attributable to deterioration of system matrix conditioning near a relative pixel size of $\Delta x_r = 1.0$.

At pixel sizes to the left of the peaks in the RMSE curves, a slight decrease in condition number is observed, but the condition number is still to be greater than 10^3 for all ROI sizes. The decrease in RMSE at smaller pixel sizes is attributable to a combination of this slight improvement in conditioning and the high degree of agreement between the LI forward model and the Radon transform at small pixel sizes. Since the conditioning is still quite poor at these pixel sizes, one should not expect to see this decrease in RMSE if even a slight perturbation of the Radon transform were used to generate the measured data. For example, we observe in section 2.4 that including a model of finite detector bin width removes the drop in RMSE to the left of the peak.

CHAPTER 3

NOISE PROPERTIES OF CT IMAGES RECONSTRUCTED BY USE OF CONSTRAINED TOTAL-VARIATION, DATA-DISCREPANCY MINIMIZATION

3.1 Introduction

In the previous chapter, our focus centered on characterizing the solutions to the optimization problems that motivate IIR design. In practice, however, there can be a large disconnect between iterative algorithms and their motivating optimization problems. As was seen, depending on the pixel size, the linear system model in CT is often ill-conditioned. As a result, the number of iterations required for an accurate solver can be much greater than 1,000. When iteration numbers are this large, the trajectory of image estimates can be quite important because practical application of IIR dictates iteration numbers on the order of ten or one hundred – well short of convergence. In this chapter, we therefore focus on an investigation of practical algorithms truncated at early iteration.

A common strategy for obtaining useful images rapidly is to employ algorithms that process the data sequentially [49,50]. In particular, for sparse-view CT, our lab has developed the adaptive-steepest-descent-projection-onto-convex-sets (ASD-POCS) algorithm [21], which is sequential in that it employs ART for the data agreement step. This algorithm has been shown to yield useful images at low iteration numbers [2]. The version of ASD-POCS reported in Ref. [21] is designed to solve the data-discrepancy-constrained total-variation (TV) minimization problem. For low-dose CT, where the data noise is relatively high, ASD-POCS has been adapted for accurate solution of total-variation (TV) constrained, data-discrepancy minimization [51]. While this algorithm was effective, it required at least 100 iterations and the algorithm had five control parameters, *four* of which required tuning. Using the incremental framework presented in this chapter, useful images can be obtained from the TV

constrained optimization problem with as few as twenty iterations, and only *one* algorithm parameter needs to be tuned.

Recently, an incremental framework [52, 53] has been developed from which sequential iterative algorithms can be derived that both yield useful images at low iteration numbers and converge to the solution of a designed optimization problem. The reason why such a framework can be helpful for IIR algorithm development is that many design principles such as maximum entropy, maximum likelihood (ML), and sparsity exploitation are a form of optimization. It is not clear that truncating the iteration of the optimization problem solver will yield images that reflect the intentions of the designed optimization problem. With the incremental framework, where initial convergence is rapid, there may be a stronger link between early image estimates and the solution to the designed optimization.

In this chapter, we investigate the use of TV-constrained data-discrepancy minimization for sparse-view image reconstruction from noisy breast CT data. The use of the TV semi-norm is motivated by selecting images with a sparse gradient magnitude image (GMI), and TV is known to be effective in reducing artifacts due to view angle under-sampling. Introducing this semi-norm in the form of a constraint allows us to compare different data fidelity objective functions on an equal footing. In particular, we investigate the use of data fidelity terms derived from the maximum likelihood principle. The purpose of the study is to determine whether the statistically motivated design of the optimization problem is reflected in images obtained at early iterations.

Simulated CT data are generated, modeling the low-dose conditions of breast CT, using a Poisson statistics noise model for the transmitted intensity. Image reconstruction is performed with incremental algorithms, which constrain the image TV and minimize: (1) unweighted least-squares (LSQ), (2) weighted least-squares (WLSQ), and (3) Poisson-likelihood (PL) motivated objective functions. The WLSQ objective function is designed to approximate that of PL. The comparisons are performed on estimating statistical properties of the reconstructed images from 1,000 noise realizations of the simulated transmission

intensity data. In Sec. 3.2, the theoretical background for the incremental algorithms is presented along with the algorithms themselves. In Sec. 3.3 extensive simulations are performed comparing the incremental algorithms for IIR from low-dose CT data. In Sec. 3.4, we discuss practical aspects on the use of the various incremental algorithms focusing also on the application of the maximum-likelihood principle.

3.2 Data model and incremental algorithms

3.2.1 Data model

We employ a generic linear model for X-ray projection

$$Ax = b \tag{3.1}$$

where $x \in \Re^n$ represents an image; $b \in \Re^m$ is a sinogram; and $A \in \Re^{m \times n}$ denotes X-ray projection. For the present study, we consider a CT data model where the transmitted X-ray intensity follows a Poisson distribution. Let N_0 be the number of photons incident on the object for each ray and consider modeling the number of photons incident on the detector in the i^{th} ray, $\tilde{y}_i$, as a Poisson random variable with mean $N_0 p_i(x)$. Throughout this chapter, quantities denoted with tildes will be reserved for random variables and the corresponding quantity without a tilde will denote a realization of that random variable. From the definition of $\tilde{y}_i$ we have

$$\Pr(\tilde{y}_i = y_i) = \frac{(N_0 p_i(x))^{y_i}}{y_i!} e^{-N_0 p_i(x)}. \tag{3.2}$$

For transmission tomography we take

$$p_i(x) = \exp\left(-a_i^T x\right), \tag{3.3}$$

where a_i is the ith row of the projection matrix A. We note that it is possible that the measured transmitted intensity y_i for a particular ray could be zero, and in this case the measurement does not contain reliable information on the object and it is simply removed from the data set and A is modified by removing the corresponding row a_i. For the scanning configurations considered here, the projection view angle is under-sampled; namely, there are too few views for (3.1) to specify a unique solution. In designing an IIR algorithm for this noise model and configuration we consider data fidelities motivated by maximum likelihood combined with a constraint capping the image TV.

3.2.2 Optimization problems

TV-constrained PL maximization We formulate a convex optimization problem based on the PL function. Given m measurements N_i, assuming that each random variable $\tilde{N}_i$ is independent, the log likelihood function is given by

$$\mathcal{L}(x|y) = \ln\left(\prod_{i=1}^{m} \Pr(\tilde{y}_i = y_i)\right) \tag{3.4}$$

$$\propto \sum_{i=1}^{m} \left(-y_i a_i^T x - N_0 \exp\left(-a_i^T x\right)\right). \tag{3.5}$$

As opposed to maximizing this expression over x, we minimize its negative subject to a TV constraint. Thus, given a data vector of X-ray transmission measurements $y \in \Re^m$, our goal is to solve the convex optimization problem

$$\min_x \sum_{i=1}^{m} \left(y_i a_i^T x + N_0 \exp\left(-a_i^T x\right)\right) \tag{3.6}$$

$$\text{such that } TV(x) \leq \gamma$$

The parameter γ is the TV constraint parameter.

The total-variation function (TV) is given by

$$TV(x) = \|Dx\|_{1,2} = \sum_{i=1}^{n} \|D_i x\|_2 \tag{3.7}$$

where $D_i \in \Re^{d\times n}$ is a finite differencing matrix approximating the gradient of the d-dimensional image at the i^{th} pixel and $D \in \Re^{nd\times n}$ is given by

$$D = \begin{pmatrix} D_1 \\ \vdots \\ D_n \end{pmatrix} \tag{3.8}$$

Including TV in (3.6) this way has a couple of advantages: comparisons using other data fidelity terms or different sampling schemes can be made on an equal footing, and simulation studies are simplified in that the TV of the test phantom is available to use as γ.

TV-constrained WLSQ When large numbers of photons are detected, the probability distribution in (3.2) can be approximated by a multivariate Gaussian with mean equal to the variance. Working with the negative logarithm of the mean transmission data

$$b = -\ln\left(\frac{y}{N_0}\right),$$

the transformed data are approximately distributed

$$\Pr(\tilde{b} = b) \propto \exp\left(-\frac{1}{2}(Ax-b)^T\Sigma^{-1}(Ax-b)\right), \tag{3.9}$$

where the covariance Σ is diagonal with variance equal to one over the mean transmitted X-ray intensity

$$\Sigma = \operatorname{diag}\left(\frac{1}{N_0\exp(-Ax)}\right). \tag{3.10}$$

To incorporate this likelihood into an optimization, we consider the general TV-constrained

WLSQ problem

$$\min_x \frac{1}{2}(Ax-b)^T W(Ax-b) \tag{3.11}$$
$$\text{such that } TV(x) \leq \gamma$$

The matrix $W \in \Re^{m\times m}$ is a diagonal weighting matrix, and we refer to the individual diagonal elements as w_i for $i = 1, \ldots, m$. The maximum likelihood data fidelity is achieved by setting the weights to Σ^{-1}

$$W = \text{diag}(N_0 \exp(-Ax)).$$

We note that the TV-constrained LSQ problem corresponds to the case where the diagonal elements of W are set to one.

3.2.3 Incremental algorithms

A class of algorithms known as incremental proximal gradient methods (IPG) have been proposed [52] to efficiently solve large-scale, convex optimization problems. The incremental framework of interest applies to an objective function $f : \Re^n \mapsto \Re$ written as the sum of S terms in the following form

$$f(x) = \sum_{i=1}^{S} (g_i(x) + h_i(x)) \tag{3.12}$$

where $g_i, h_i : \Re^n \mapsto \Re$ are convex. The optimization problems of (3.6) and (3.11) fit this form in this sense: each of the data fidelity functions consist of sums of terms depending only on single measurements and the TV constraint, coded as an indicator function, is represented as one term. In these incremental methods, one takes first-order steps seeking to minimize each g_i and h_i individually. Empirically, fast initial convergence rates have been observed with such methods [54].

More recently, relaxed versions of the IPG methods have been proposed [53]. We present the k^{th} update steps for the one of the relaxed incremental proximal gradient (R-IPG) methods for minimization of a function f as in (3.12) subject to a convex constraint set X here:

$$\text{(R-IPG1)} \qquad \begin{aligned} q_k &= \text{prox}_{t_k g_{i_k}}(x_k) \\ z_k &= q_k - t_k \widetilde{\nabla} h_{i_k}(q_k) \\ x_{k+1} &= \mathcal{P}_X(\rho z_k + (1-\rho)x_k) \end{aligned}$$

where $\mathcal{P}_X : \Re^n \mapsto \Re^n$ is the projection onto the convex set X and the proximal mapping is given by

$$\text{prox}_{t_k g_{i_k}}(x) = \underset{u}{\text{argmin}} \left\{ g_{i_k}(u) + \frac{\|x-u\|_2^2}{2t_k} \right\} \tag{3.13}$$

Note the argmin operation returns a unique value since the function in its argument is strongly convex. The symbol $\widetilde{\nabla} h_i(w_k)$ represents a subgradient of h_i at w_k. The value of the relaxation parameter ρ must lie in the interval $(0, 2)$ to ensure convergence.

The value of i_k can chosen in a cyclic fashion such as $i_k = k\%S$ — where we have used % to denote the modulus operation — or in a randomized manner. We refer the interested reader to [52] for more information about convergence rates in both cases. The step-size t_k must be chosen such that

$$\sum_{k=1}^{\infty} t_k = \infty \tag{3.14}$$

$$\lim_{k \to \infty} t_k = 0 \tag{3.15}$$

to ensure the algorithm does not end up in a limit cycle yet can still travel far enough to

reach the optimal set.

Technically, the optimization problems (3.6) and (3.11) do not meet the criteria for convergence proof of R-IPG1 because the indicator function coding the TV constraint is not Lipschitz continuous. We make a modification to these optimization problems, which does not affect the implementation of R-IPG1 when the iteration is truncated. We write both optimizations in the form

$$\min_x \{F(x) + \lambda d_C(x)\}, \tag{3.16}$$

where $F(x)$ represents either of the data fidelity objective functions, λ is a parameter, and $d_C(x)$ is the distance from the point x to the TV constraint set C

$$C \equiv \{x : TV(x) \leq \gamma\}.$$

Formulating the optimization problems in this way, the objective functions are now Lipschitz continuous so that convergence of R-IPG1 is guaranteed. The role of λ will be addressed shortly.

We derive an instance of R-IPG1 for solving TV-constrained PL maximization by defining

$$\begin{aligned} &g_i(x) = y_i a_i^T x + N_0 \exp(-a_i^T x) \text{ for } i = 1, \ldots, m \\ &g_{m+1}(x) = \lambda d_C(x) \\ &h_i(x) = 0 \text{ for } i = 1, \ldots, m+1 \end{aligned} \tag{3.17}$$

and instances of TV-constrained WLSQ and LSQ (if the weights are set to one) by defining

$$\begin{aligned} &g_i(x) = \frac{w_i}{2}(a_i^T x - b_i)^2 \text{ for } i = 1, \ldots, m \\ &g_{m+1}(x) = \lambda d_C(x) \\ &h_i(x) = 0 \text{ for } i = 1, \ldots, m+1 \end{aligned} \tag{3.18}$$

For implementation of these algorithms we need to compute the various proximal mappings.

We start with the proximal mapping of the distance function $d_C(x)$, because this step determines the final form of R-IPG1 used in this work. It is shown in Appendix A that

$$\text{prox}_{t_k g_{m+1}}(x_k) = \begin{cases} x_k + t_k \lambda \frac{(\mathcal{P}_X(x_k) - x_k)}{d_C(x_k)} & \text{if } \; d_C(x_k) \geq \lambda t_k \\ \mathcal{P}_C(x_k) & \text{else} \end{cases}$$

where $\mathcal{P}_C(\cdot)$ denotes projection on the TV constraint set C. We note that the projection in the second case corresponds to the proximal mapping of the original indicator function for C. The modification due to changing this constraint to a distance function comes in the first case when $d_C(x_k) \geq \lambda t_k$. For truncated iteration $t_k > 0$ and λ can be chosen large enough that this inequality is not satisfied over the range of k. In practice, we always take this update step to be $\mathcal{P}_C(x_k)$ and there is no change in the instance of R-IPG1 in switching the TV constraint to a distance function. We can numerically calculate the projection $\mathcal{P}_C(x_k)$ using an efficient primal-dual algorithm such as that of Chambolle and Pock (CP) [55, 56].

Incremental algorithms for TV-constrained PL maximization, WLSQ, and LSQ

The desired form of R-IPG1 is derived by setting λ large enough

$$\lambda > d_C(x_k)/t_k,$$

yielding the following R-IPG1 update steps

$$x_{k+1} = \begin{cases} \text{prox}_{t_k g_{i_k}}(x_k) & \text{if } k\%(m+1) \neq 0 \\ \mathcal{P}_C(x_k) + (1-\rho)x_k & \text{else} \end{cases}. \tag{3.19}$$

The step in first case is derived from the proximal mapping of the data fidelity terms for PL maximization, WLSQ, and LSQ. For this update the projection onto the convex set X does not appear, because we do not include additional constraints. Adding simple constraints, such as bound constraints, can be easily incorporated by specifying the appropriate constraint set X for the image x. In practice, such constraints need to be simple because they are performed at every update step k; for the data fidelity steps the index k specifies each of the terms in the corresponding objective and complex projections after each data term will prohibitively slow down the R-IPG1 algorithm. This is why the projection onto C is taken as an incremental step for $k\%(m+1) = 0$ instead of a projection at every k.

Addressing PL maximization, the corresponding proximal mapping is derived in Appendix B

$$\begin{aligned}\text{prox}_{t_k g_{i_k}}(x_k) &= x_k + t_k(N_0 \exp(-c_k^*) - y_{i_k})a_{i_k} \\ &\text{for } i_k = 1, \ldots, m,\end{aligned}$$

where c_k^* is found by implicit solution of

$$c_k^* = a_{i_k}^T x_k + t_k \|a_{i_k}\|_2^2 (N_0 \exp(-c_k^*) - y_{i_k}). \tag{3.20}$$

We also provide methods for calculating c_k^* in Appendix B. For WLSQ, and LSQ, the proximal mapping can be derived by direct computation, shown in Appendix C

$$\begin{aligned}\text{prox}_{t_k g_{i_k}}(x_k) &= x_k - \frac{a_{i_k}^T x - b_{i_k}}{\|a_{i_k}\|^2 + (t_k w_{i_k})^{-1}} a_{i_k} \\ &\text{for } i_k = 1, \ldots, m.\end{aligned}$$

This WLSQ update step resembles the algebraic reconstruction technique (ART) with a relaxation parameter ρ. The difference is an additional term in the denominator which includes the weights w_i and step-size t_k. In the discussion of the results we label each of the

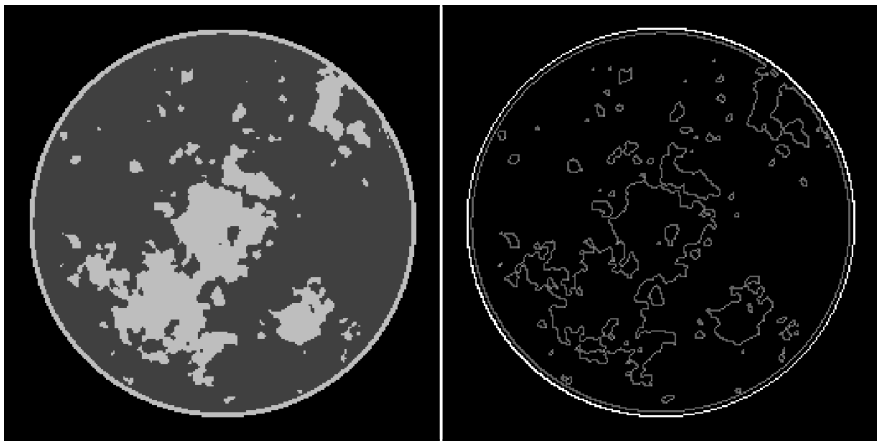

Figure 3.1: Breast phantom for CT and its corresponding gradient-magnitude image (GMI). The fat and fibro-glandular tissue has linear attenuation coefficients of 0.194 cm^{-1} and 0.233 cm^{-1}, respectively. Left is the linear attenuation map of the phantom in the gray scale window [0.174,0.253] cm^{-1}. Right is the GMI [0.0,0.1] cm^{-1} that serves to illustrate that the test phantom is sparse in the GMI.

instances of R-IPG1 by the corresponding optimization problem: TV constrained (TVC) - PL maximization or TVC-PL, TVC-WLSQ, and TVC-LSQ.

For the present work, we refer to a sub-iteration as an update step based in a single row of A and an iteration as a full cycle through all of the data followed by a single TV projection. Because we are interested in using few iterations, we choose $\rho = 1$ so that all x_k for which $k \bmod (m+1) = 0$ are guaranteed to have a total-variation of γ or less.

3.3 Results

To demonstrate the incremental algorithms with the various data fidelity objective functions, we conduct image reconstruction studies with noisy sparse-view projection data. The digital phantom shown in Fig. 3.1, consisting of a 256×256 pixel array, models a slice of a breast for the dedicated breast CT application. Because we wish to isolate the issue of the impact of noise, we do not introduce additional data inconsistency and the projection data are generated using the same linear operator as that used in the image reconstruction. The projection data consist of 100 projections onto a 512-bin linear detector array. The source-detector and source-isocenter distances are modeled to be 72cm and 36cm, respectively. The

sampling of this configuration is clearly not sufficient for direct or implicit inversion of (3.1) because the number of image pixels exceeds the number of measurements.

Noisy study For all of the results image reconstruction is performed on simulated data including noise. The same discrete-to-discrete model (3.1) generates the mean sinogram, and noise realizations for the transmitted X-ray intensity employ the Poisson model in (3.2). The integrated incident number of photons per view per detector bin is modeled to be uniform at two intensity levels: $N_0 = 2 \times 10^4$ and 2×10^5. The latter value corresponds to a fairly low intensity that might be used in an actual breast CT scan. In this simulation the only source of inconsistency is due to the noise model, and we know exactly what probability distribution function governs the noise realization selection. All other sources of inconsistency: continuous object model, beam hardening, scatter, partial volume averaging, etc., which would be present in actual CT data are suppressed. In this way, we can isolate and address the issue of the impact of maximum likelihood data fidelity terms for sparse-view CT using the incremental algorithms with truncated iteration.

Incremental algorithm parameter optimization In the implementation of TVC-PL, TVC-WLSQ, and TVC-LSQ, we employed a decreasing step-size

$$t_k = \frac{t_0}{(\lfloor k/(m+1) \rfloor)^\alpha}, \tag{3.21}$$

where $\lfloor \cdot \rfloor$ is the floor operation, and the parameter $\alpha \in (0, 1]$ is the decay exponential designed according to (3.15). The R-IPG1 instances presented in Sec. (3.2.3) depend on three algorithm parameters: t_0, α, and ρ. We consider running R-IPG1 with one hundred iterations or less under the restriction that the TV projection respect the TV constraint $TV(x_k) \leq \gamma$ after every iteration. This latter restriction forces $\rho = 1$, and for such low iteration numbers the impact of α is weak. Accordingly, we set $\alpha = 0$, and consider only variation in t_0. Each of the optimization problems depend on the TV constraint parameter

γ and, in the case of TVC-WLSQ, on the choice of weights w_i. For the present study we assume access to the phantom TV, γ_0, and for TVC-WLSQ we assume knowledge of the object dependent variance in (3.10). While such knowledge is not realistic in actual application with unknown subjects, it serves to illustrate upper bound performance of the algorithms of interest.

Because the image TV constraint is satisfied at every iteration, it is sufficient to optimize t_0 based only on the corresponding value of the data fidelity objective function. Shown in Fig. 3.2 is the average data fidelity as a function of t_0 at iteration numbers 20, 50, and 100 for the three algorithms of interest setting $\gamma = \gamma_0$. The optimal value of t_0 is the one which minimizes the particular data fidelity for a given number of iterations. In all cases optimal t_0 occurs at smaller values when more iterations are performed. The curves for TVC-WLSQ and TVC-LSQ are fairly similar, while those of TVC-PL show rapid increase as t_0 decreases. The TVC-WLSQ and TVC-LSQ algorithms appear to be less sensitive to t_0 than TVC-PL.

For obtaining reconstructed images, we record the optimal value of t_0 for each algorithm at 20, 50, and 100 iterations. In Fig. 3.3 single images are shown for each case and for $N_0 = 2 \times 10^5$. Interestingly, even at 20 iterations the reconstructed images in all cases resemble the test phantom without any obvious artifacts due to truncated iteration. There is a slight sharpening of the TVC-PL images in going from 20 to 50 iterations; otherwise there is no clear difference between images for different iteration numbers. The images corresponding to TVC-PL and TVC-WLSQ appear to have less noise particularly toward the middle of the image. This is an indication that exploiting maximum likelihood does potentially have a beneficial impact in reducing noise variance without sacrificing bias.

Image statistics To investigate the noise properties in more depth, we focus on the 50 iteration case and perform 1,000 noise realizations using the Poisson model for the X-ray transmission data and reconstruct images with TVC-PL, TVC-WLSQ, and TVC-LSQ. From the 1,000 reconstructed images a mean image is estimated along with a map of the pixel

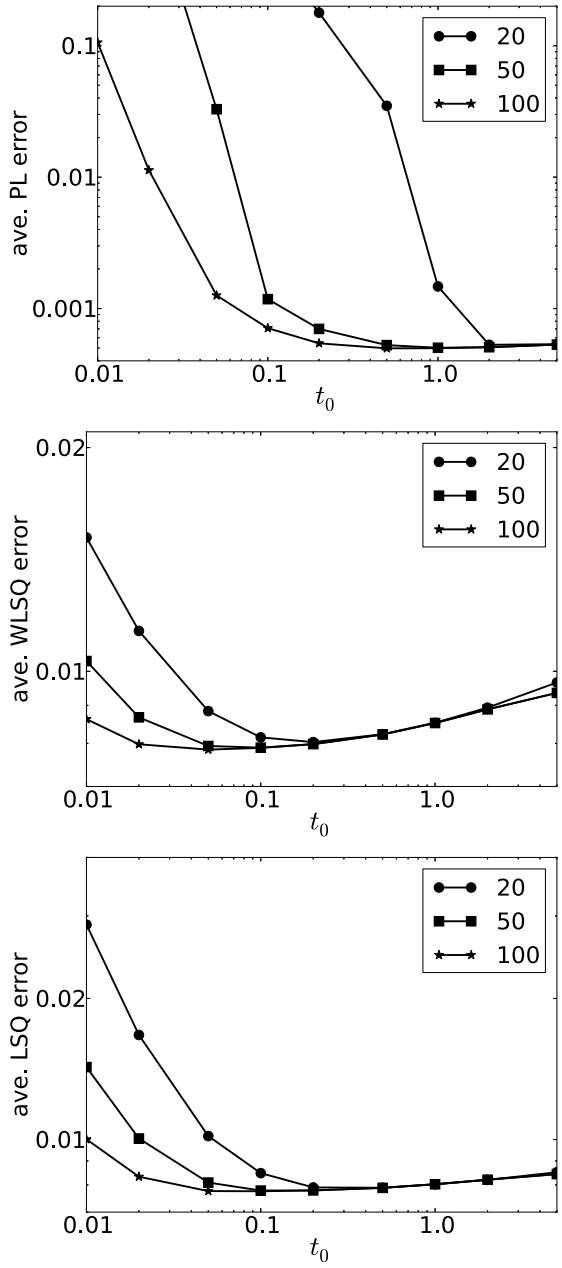

Figure 3.2: Log-log plots of the average value of the data fidelity objective function for TVC-PL, TVC-WLSQ, and TVC-LSQ as a function of the incremental algorithm parameter t_0. Different curves in each graph correspond to different numbers of iterations, and these numbers appear in the legend. The average objective values are computed by evaluating the respective objective functions for the final image x_k and dividing by the number of measurements m. In the case of the PL objective, the minimum possible value is not zero. As a result, the plotted average PL data-discrepancy represents the average over the PL data fidelity minus this fidelity evaluated with the phantom itself. It is also important to note that only the numbers within each graph can be compared; it is not meaningful to compare the values of different data fidelity objective functions.

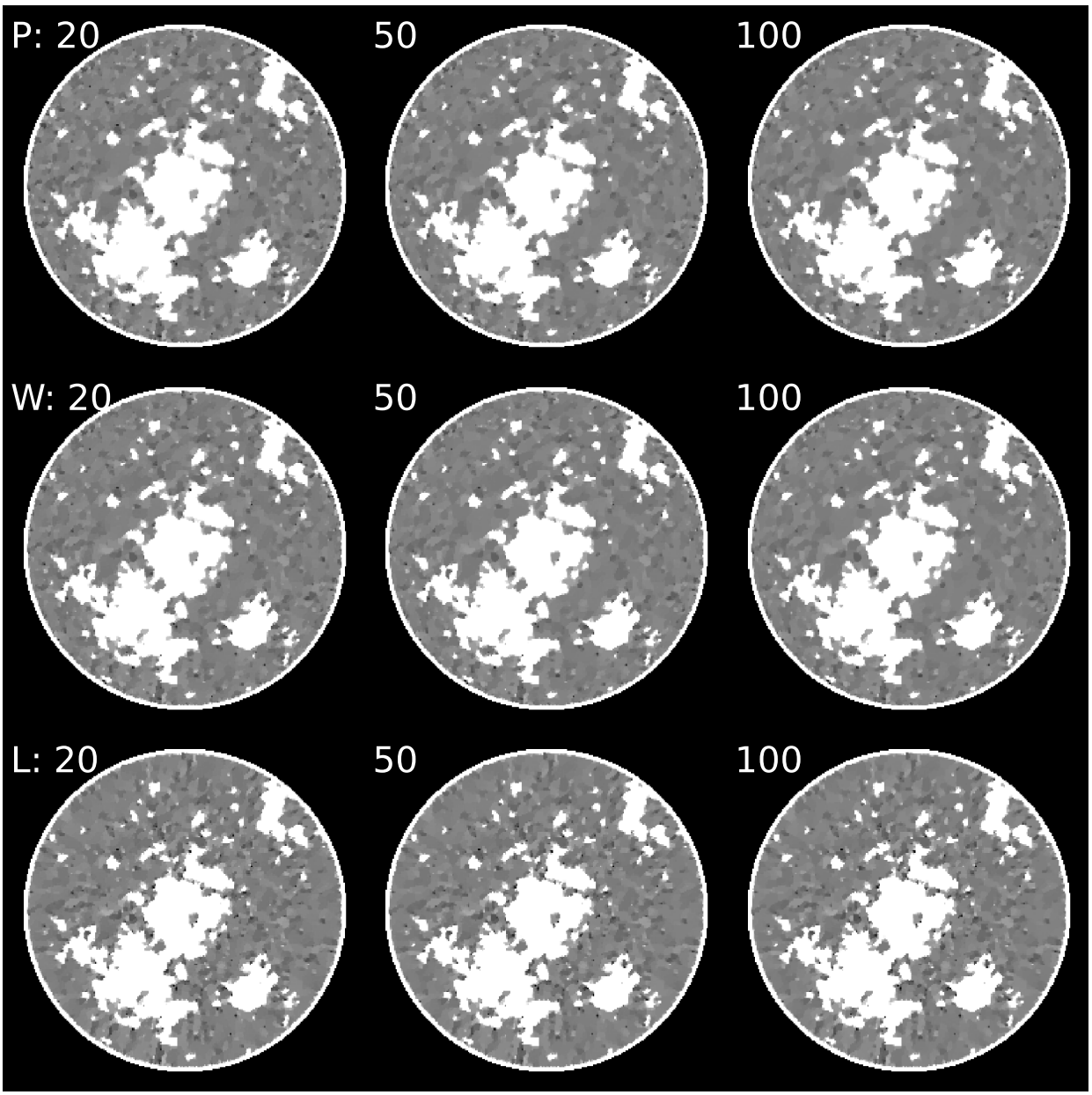

Figure 3.3: Single images corresponding to the minima of each curve in Fig. 3.2. The top, middle, and bottom rows correspond to TVC-PL (denoted "P"), TVC-WLSQ (denoted "W"), and TVC-LSQ (denoted "L"), respectively. The left, middle, and right columns are the images at iteration number 20, 50, and 100, respectively. The display window is selected to be [0.184,0.204] cm^{-1}, centered on the background fat tissue. In this way, the noise level on the fat portion of the image is clearly depicted.

standard deviations all shown in Fig. 3.4 for the case of $N_0 = 2 \times 10^5$. The mean image is quite close to the test phantom, but subtracting the phantom from the mean images does highlight some differences between the results of the three algorithms. The standard

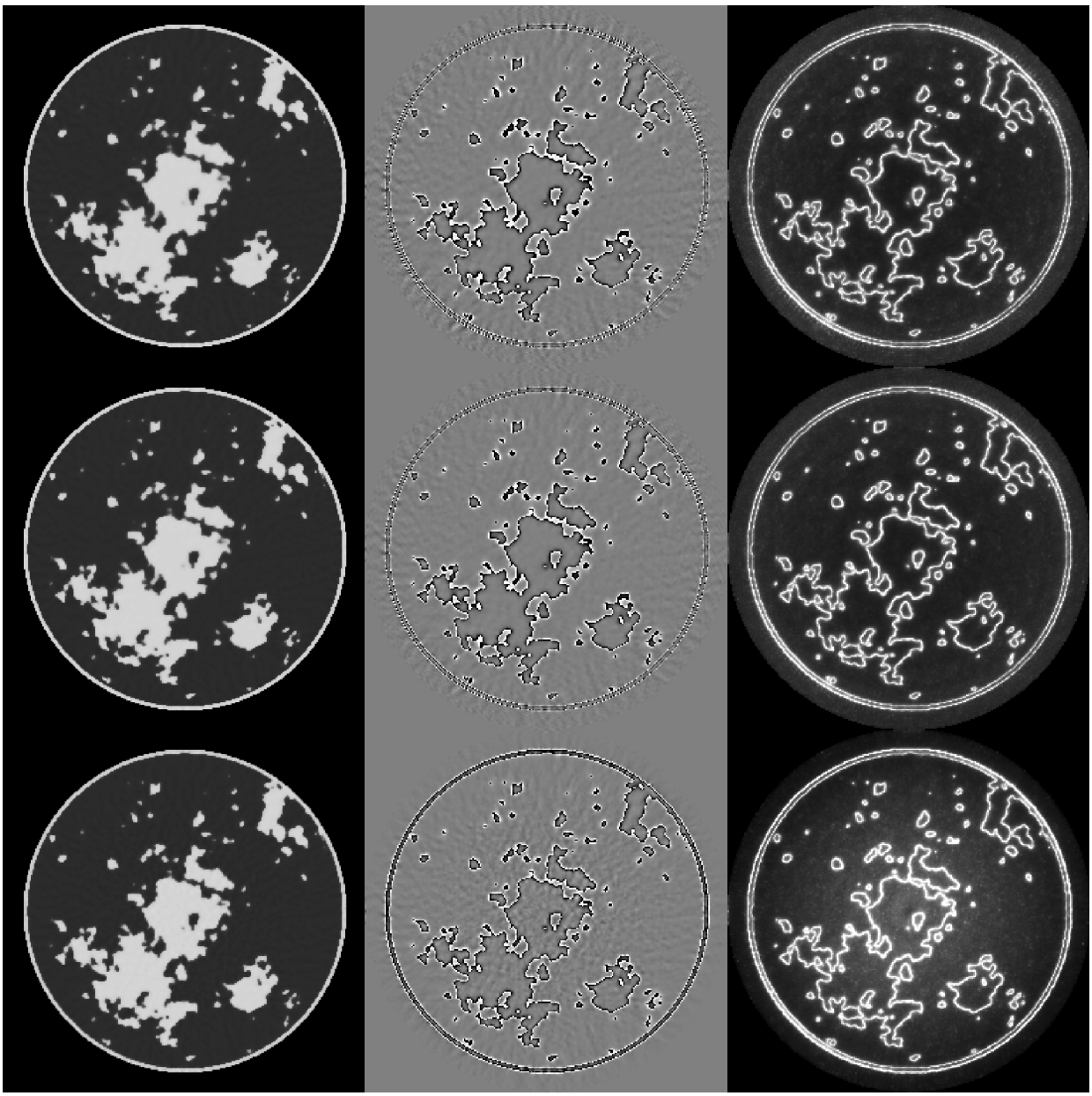

Figure 3.4: Statistical properties of reconstructed images by TVC-PL (top row), TVC-WLSQ (middle row), and TVC-LSQ (bottom row) estimated from the images at 50 iterations for 1,000 noise realizations of the data model. The left column is the mean image in the gray scale [0.184,0.243] cm^{-1}. The middle column is the breast phantom subtracted from the mean image in the gray scale [-0.005,0.005] cm^{-1}. Finally, the right column is the estimated image standard deviation also in the gray scale window [0.0,0.005] cm^{-1}.

deviation images are interesting in that the distributions are quite non-uniform as the standard deviation appears to be amplified near the borders between tissue types. A similar phenomenon was observed in Ref. [57] with the use of edge-preserving regularization. Also,

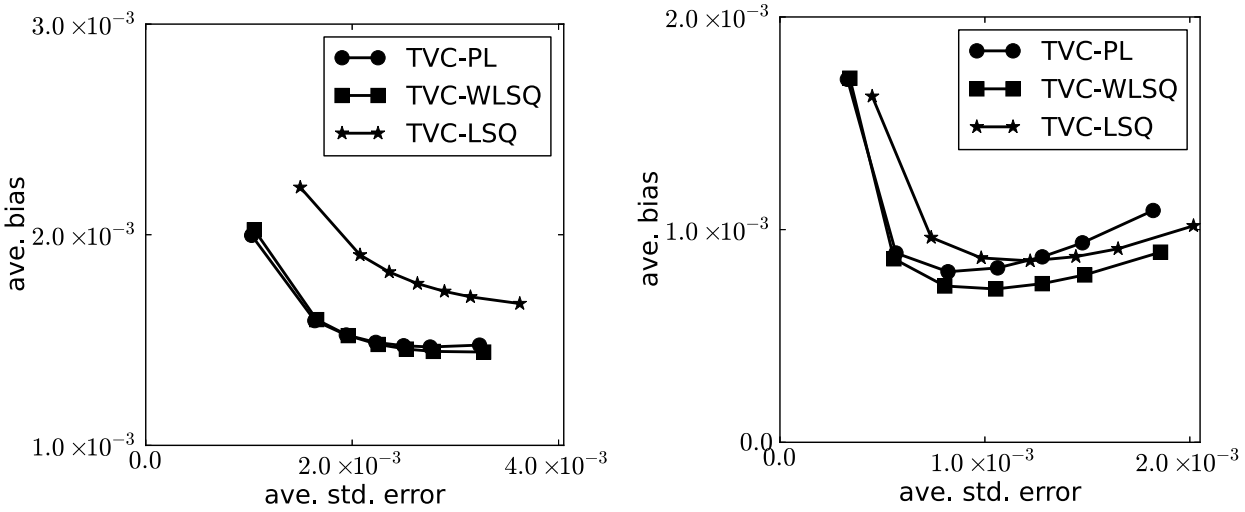

Figure 3.5: Average bias versus average standard deviation curves generated by image reconstruction with each of the incremental algorithms at 50 iterations for (left) $N_0 = 2 \times 10^4$ and (right) $N_0 = 2 \times 10^5$. The curves are generated by varying the TV constraint parameter γ among seven values. These TV values are computed as the fractions $[0.8, 0.9, 0.95, 1.0, 1.05, 1.1, 1.2]$ of the phantom TV, γ_0. The curve values are indicated by the various symbol dots with the one corresponding to the lowest fraction, 0.8, appearing on the leftmost point of each curve.

the standard deviation of the image ensembles reconstructed by TVC-PL and TVC-WLSQ appear to have lower amplitude than that of TVC-LSQ particularly toward the middle of the image. This result strengthens the observation from the single images shown in Fig. 3.3 that use of maximum likelihood leads to lower amplitude noise in the reconstructed image than that corresponding to the unweighted data fidelity term.

To further investigate the reconstructed image noise properties we generate standard deviation-bias curves by varying the TV constraint parameter γ and computing the mean standard deviation and bias over the corresponding images. The results for both intensity settings are shown in Fig. 3.5. For $N_0 = 2 \times 10^4$ the TVC-WLSQ and TVC-PL curves are similar with both results having lower variance and bias than the corresponding points of the TVC-LSQ results. The results for $N_0 = 2 \times 10^5$ appear quite different. The TVC-WLSQ and TVC-LSQ curves show a minimum average bias at $\gamma = \gamma_0$. While for TVC-PL the minimum average bias is obtained when $\gamma = 0.95\gamma_0$. The average image standard deviations are quite close for TVC-PL and TVC-WLSQ indicating that the Gaussian approximation of

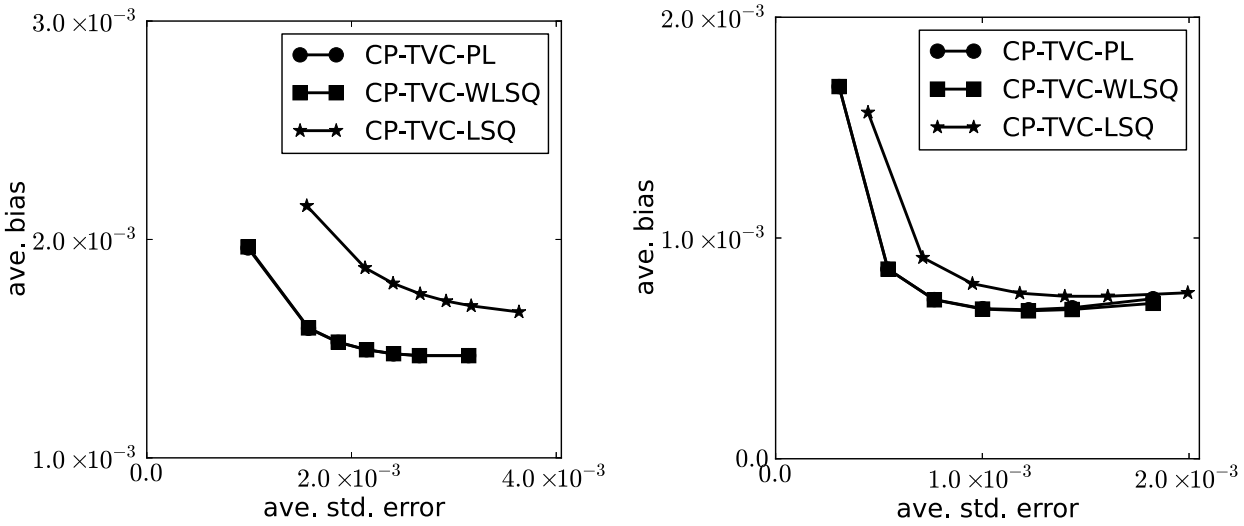

Figure 3.6: Same as Fig. 3.5 except that curves are generated from an ensemble of 100 images obtained by solving the respective optimization problems with the CP algorithm.

the Poisson model and the linearization of the data variance through the negative natural logarithm operation are quite good approximations. The TVC-LSQ curve shows significantly higher standard deviation than the other two for all selected γ. There is a surprisingly large gap between the average bias of TVC-PL and TVC-WLSQ with the latter below the former. In order to determine whether or not the gap between TVC-PL and TVC-WLSQ for the $N_0 = 2 \times 10^5$ case is due to a discrepancy in convergence, we estimate image statistics from an ensemble of 100 images, which are converged solutions to the respective optimization problems. The converged images are obtained from 2,000 iterations of the CP [55,56] algorithm, and the resulting plots are shown in Fig. 3.6. For the case of $N_0 = 2 \times 10^4$ the agreement between the R-IPG1 and CP results is close and both sets of results show similar curves. For $N_0 = 2 \times 10^5$, however, there is a larger discrepancy between the R-IPG1 and CP results. The CP results show close agreement between CP-TVC-WLSQ and CP-TVC-PL, while the R-IPG1 results do not. Thus the latter disagreement can be attributed to slower convergence of TVC-PL relative to TVC-WLSQ.

Another interesting phenomenon in the $N_0 = 2 \times 10^5$ results of Fig. 3.5 is that both the standard deviation and bias increase for each curve as γ increases beyond γ_0. In order to see why this happens we focus on mean and standard deviation maps, shown in Fig. 3.7, for

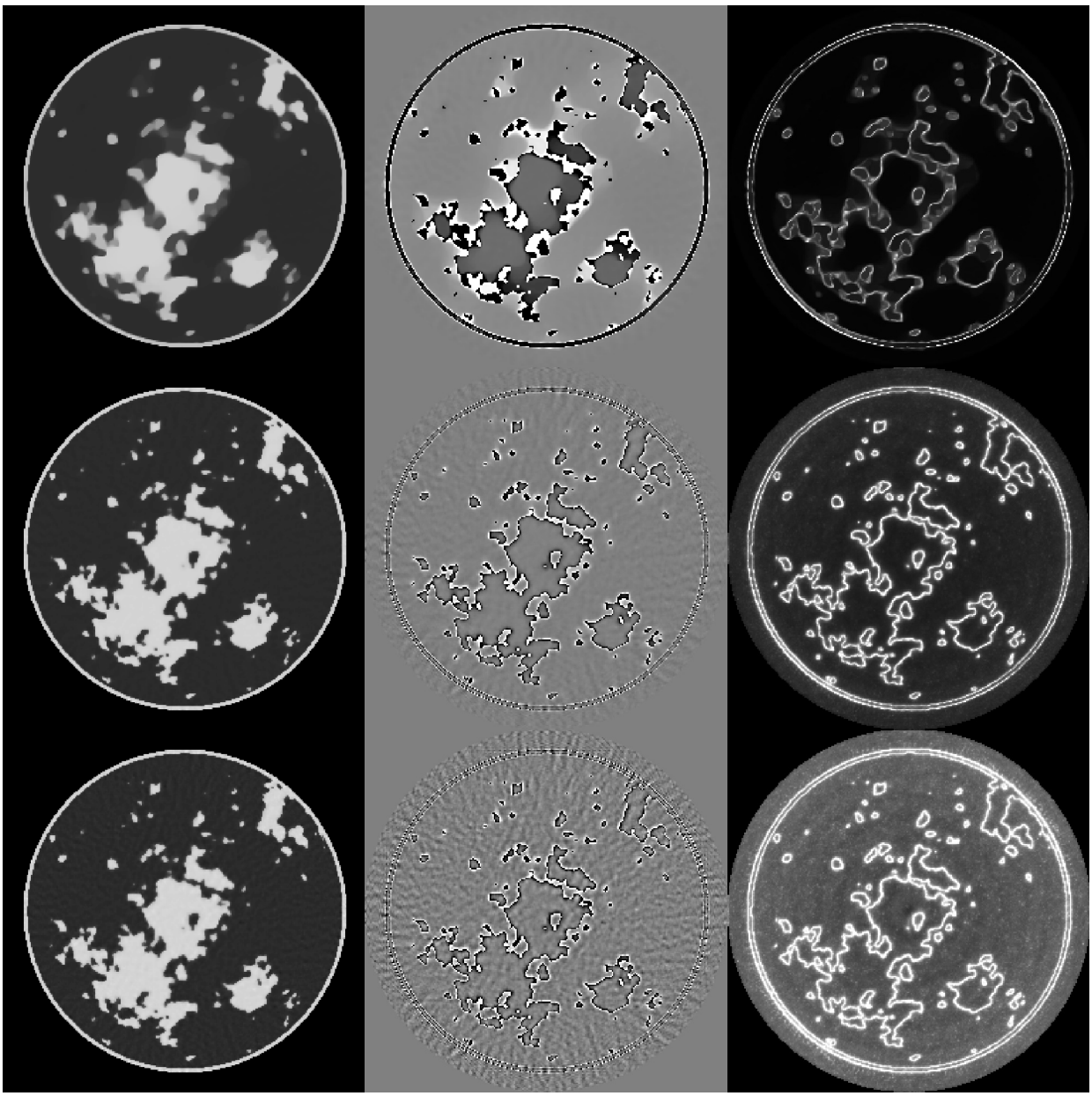

Figure 3.7: Same as Fig. 3.4 except that the rows all correspond to 50 iterations of TVC-WLSQ for the TV constraint parameters: $\gamma = 0.8\gamma_0$ (top row), $\gamma = \gamma_0$ (middle row), and $\gamma = 1.2\gamma_0$.

TVC-WLSQ for three different values of γ. For the case of $\gamma = 0.8\gamma_0$ the standard deviation map has clearly lower amplitude than that of $\gamma = \gamma_0$, but the bias is visually larger as the mean image is significantly blurred for the lower value of γ. For the $\gamma = 1.2\gamma_0$ results the standard deviation map has larger amplitude as expected. The bias map in this case reflects a situation unique to view angle under-sampling. For such conditions the TV constraint

not only serves to regularize the image against noise, but it also assists the image recovery in the noiseless case. As the TV constraint is loosened the phantom is no longer recovered from ideal under-sampled data. As a result streak artifacts become apparent in the bias map and the average bias rises relative to that of $\gamma = \gamma_0$. This effect is less pronounced in the $N_0 = 2 \times 10^4$ results because data noise is more dominant.

3.4 Practical advantages of each of the R-IPG1 algorithms

First, we point out that the performance of TVC-PL, TVC-WLSQ, and TVC-LSQ is remarkable considering the simple structure of these algorithms. Over the 1,000 noise realizations each algorithm achieved the TV constraint to within 0.01% of the target γ and the final data fidelity varied less than 0.1% over the ensemble of realizations. Most importantly the visual appearance of the reconstructed images is close to the test phantom for low numbers of iterations.

Use of TVC-PL appears to reduce noise variance in the reconstructed image relative to TVC-LSQ provided that the noise model matches the Poisson distribution of the X-ray transmission data. TVC-PL is slightly more complicated to implement than TVC-LSQ, but the difference in implementation and algorithm efficiency is minor. Moreover, TVC-PL does not introduce more optimization parameters than TVC-LSQ. As a result, if the assumed data model applies, or is a close approximation, TVC-PL provides the better option to obtain images with reduced noise amplitude without sacrificing image bias.

In the performed simulation studies it appears at first glance that TVC-WLSQ is the best option even though the data realizations are generated with the Poisson model. We point out, however, that the achieved performance in terms of bias versus standard deviation assumed knowledge of the ideal weights for the quadratic data fidelity. In practice, such weights are not available. If the existing data are used to obtain an estimate for the weights, the advantage in terms of image variance will be lost because the existing data contain noise. A smoothed version of the data may provide a better estimate of the weights. Also, the TVC-

WLSQ algorithm may have further advantage when other sources of noise are considered such as detector electronic noise.

The TVC-LSQ algorithm may also have advantages in some situations. As pointed out noise is not the only form of data inconsistency, and if other physical factors are more important than the difference in noise modeling then TVC-LSQ is a good option. It appears also that the convergence of TVC-LSQ is slightly faster than that of TVC-PL at least for the CT system investigated here.

3.5 Conclusion

We have applied the incremental framework of Refs. [52,53] to generate algorithm instances of TV constrained, data-discrepancy minimization for CT image reconstruction. The algorithm yields an accurate solution to the designed optimization problem at large iteration numbers and can provide a useful image at low iteration numbers. The TVC-PL, TVC-WLSQ, and TVC-LSQ are all run at low iteration numbers, yet the resulting images appear to reflect the design considerations of the corresponding optimization problem. Each of the optimization problems contains the TV constraint for mitigating streaking due to angular under-sampling. Indeed, each of the reconstructed images appear to be free from this artifact with $\gamma \leq \gamma_0$. Furthermore, the results of the noise studies with each algorithm indicate that the maximum likelihood data fidelity terms have an impact even though the iteration number is severely truncated.

Appendix A: proximal mapping of distance from a convex set

Let $g(x) = \lambda d_C(x)$. Our goal is to find

$$\text{prox}_{tg}(x) = \underset{u}{\text{argmin}} \{\lambda d_c(u) + \frac{1}{2t}\|u - x\|_2^2\} \tag{3.22}$$

We shall use the optimization condition for unconstrained convex minimization that u^*

is an optimal point if and only if $0 \in \partial_c(u^*)$. For proof of this fact we refer the reader to [58]. We thus need the subdifferential of $d_c(x)$ which is given by

$$\partial d_c(u) = \begin{cases} N_C(u) \cap \{v : \|v\|_2 \leq 1\} & \text{if } u \in C \\ \left\{ \frac{u - \mathcal{P}_C(u)}{\|u - \mathcal{P}_C(u)\|_2} \right\} & \text{else} \end{cases}$$

where for a convex set, the normal cone, $N_C(u)$ can be written as

$$N_C(u) = \{y : y^T(z - u) \leq 0 \ \ \forall z \in C\} \tag{3.23}$$

we thus see that at an optimal point u^*, one of two conditions must hold

$$1) \ \ x - u^* = \frac{\lambda t}{d_c(u^*)}(u^* - \mathcal{P}_c(u^*)), \ \ u^* \notin C$$
$$2) \ \ x - u^* \in \lambda t N_C(u^*) \cap \{v : \|v\|_2 \leq 1\}, \ \ u^* \in C$$

If condition 1) holds, we see that x, u^*, and $\mathcal{P}_C(u^*)$ all fall along a line, which, along with $u^* \notin C$ and the convexity of C, implies that $\mathcal{P}_C(u^*) = \mathcal{P}_C(x)$. In addition, if $\lambda t \leq d_C(x)$, we see that u^* is a convex combination of x and $\mathcal{P}_C(x)$, namely

$$u^* = x + \lambda t \frac{\mathcal{P}_C(x) - x}{d_C(x)} \ \ \text{if } d_C(x) \geq \lambda t \tag{3.24}$$

On the other hand, if condition 2) holds, then we have

$$\|x - u^*\|_2 \leq \lambda t \tag{3.25}$$
$$(x - u^*)^T(z - u^*) \leq 0 \ \ \forall \ \ z \in C \tag{3.26}$$

It is clear that $\mathcal{P}_C(x)$ satisfies both conditions assuming $\lambda t \geq d_C(x)$. We have thus found points satisfying the optimality condition in two cases: when $\lambda t < d_c(x)$ and when $\lambda t \geq$

$d_c(x)$. Since the minimization is performed on a strongly convex function, we know these points are the unique minima of the function in the two cases. We have thus obtained the desired result.

Appendix B: proximal mapping for linear plus exponential

Let $g(x) = ya^T x + N\exp(-a^T x)$ where $y \in \Re$, $a \in \Re^n$, $x \in \Re^n$, and $N \in \Re$. Our goal is to find

$$\text{prox}_{tg}(x) = \underset{u}{\text{argmin}} \{g(u) + \frac{1}{2t}\|u - x\|_2^2\} \tag{3.27}$$

Noting that the argument is everywhere differentiable, we may simply set the gradient equal to zero to obtain our optimality condition, yielding

$$ya - N\exp(-a^T u^*)a + t^{-1}(u^* - x) = 0 \tag{3.28}$$

Dotting both sides with a and rearranging terms we find

$$a^T(u^* - x) = t\|a\|_2^2(N\exp(-a^T u^*) - y) \tag{3.29}$$

We suggest two methods to solve for $a^T u^*$ in (3.29). First, one can use a root finding method such as the Newton-Raphson method. Second, one can rearrange (3.29) further to yield

$$(a^T(u^* - x) + t\|a\|_2^2 y)e^{a^T(u^*-x)+t\|a\|_2^2 y} = t\|a\|_2^2 N e^{t\|a\|_2^2 y - a^T x} \tag{3.30}$$

from which one can see the solution is

$$a^T u^* = W_0(t\|a\|_2^2 N e^{t\|a\|_2^2 y - a^T x}) - t\|a\|_2^2 y + a^T x \tag{3.31}$$

where W_0 is the Lambert W-function (we confine our attention here to the real-valued

principle branch W_0) which is defined to be the inverse of the function

$$g(z) = ze^z \tag{3.32}$$

and is a single-valued mapping of the non-negative reals. This solution may be useful because methods for calculating the Lambert W-function are provided in many standard programming libraries.

Denoting the solution to (3.29) as $c^* = a^T u^*$, we then have from equation (3.28)

$$\text{prox}_{tg}(x) = x + t(N \exp(-c^*) - y)a \tag{3.33}$$

Appendix C: proximal mapping of weighted quadratic

Let $g(x) = (a^T x - b)^2 w$ where $a \in \Re^n$, $b \in \Re$ and $w \in \Re$. Our goal is to find

$$\text{prox}_{tg}(x) = \underset{u}{\text{argmin}} \{(a^T u - b)^2 w + \frac{1}{2t}\|u - x\|_2^2\}$$

Since the argument is differentiable everywhere, our optimality condition is found simply by setting the gradient to zero, yielding

$$w(a^T u^* - b)a + \frac{1}{t}(u^* - x) = 0 \tag{3.34}$$

Dotting both sides with a and rearranging terms we find

$$a^T u^* = \frac{a^T x + b\|a\|_2^2 wt}{1 + \|a\|_2^2 wt} \tag{3.35}$$

Plugging this result back into the original expression yields

$$u^* = x - \frac{a^T x - b}{(wt)^{-1} + \|a\|_2^2} \tag{3.36}$$

which is the desired result.

CHAPTER 4

INVESTIGATING SIMULATION-BASED METRICS FOR CHARACTERIZING LINEAR ITERATIVE IMAGE RECONSTRUCTION IN DIGITAL BREAST TOMOSYNTHESIS

4.1 Introduction

In chapters 2 and 3 simulation-based metrics were employed to characterize parameter trends of IIR algorithms for breast CT. For the next two chapters, we shift focus to a different X-ray imaging modality, namely digital breast tomosynthesis. As in CT, image reconstruction for DBT, whether direct or iterative, invariably involves a variety of parameters and implementation choices, such as voxel size, voxel aspect ratio, and regularization strength [19]. While experience from CT provides some insight into the parameter dependence of these algorithms, this experience alone is insufficient for the tailoring of algorithms to DBT. As in CT, exhaustive exploration of implementations and parameter settings is warranted for every algorithm, task, and DBT system design under consideration. Efficiently computable objective image quality metrics are necessary to facilitate this task.

Numerous authors have investigated metrics addressing this issue, some quantifying image artifacts specific to DBT, [16, 59] some using DBT tailored versions of traditional CT metrics, [60–62] and others calculating task-specific detectability indices. [62–69] A number of these works focus on optimization of system acquisition parameters, [59–61, 63, 65, 67–69] or assessment of reconstruction algorithms. [16, 64, 66]

Metrics for DBT imaging fall into two categories: those that are applied to actual DBT scans, and those that are applied to DBT simulations. Metrics for real data are clearly more direct and are useful for DBT systems characterization and optimization, but there is the potential for error due to the fact that the truth is unknown. In particular, for subtle features such as small spiculations or calcifications, error in assessing their detectability or

morphology can be large. It is also precisely for these subtle DBT features where image reconstruction parameters can have the greatest impact. For this reason, it is also desirable to have metrics that summarize qualities of DBT image reconstruction from simulated data.

In this chapter, we follow the latter approach and seek to establish additional metrics for DBT image reconstruction parameter characterization based on simulation, where the underlying true object is known. To establish relevance of the proposed metrics, we compare the metric trends with trends in the visualization of reconstructed DBT images from simulation and actual scanner data.

Due to the limited scanning angular range, DBT cannot provide an accurate 3D reconstructed volume. This basic feature of DBT imaging can limit the usefulness of image quality metrics based on tomographic image fidelity. We illustrate this problem with studies based on image RMSE. While absolute image fidelity is not achievable for image reconstruction in DBT even under ideal simulation with no noise, there are features of the scanned object which are recovered. We modify image RMSE in such a way that the new RMSE-based measure is sensitive only to features of the scanned object that are recoverable in a DBT scan. We also investigate an image quality metric based on a signal detection task. Such metrics reflect an important imaging task for DBT and their applicability is not hindered by the inability to obtain accurate tomographic image reconstruction in DBT.

In this chapter, we investigate three image quality metrics for DBT image reconstruction, two based on image fidelity and one based on a detection task. The task-based metric extends on our lab's previous work in the context of analytic reconstruction algorithms in breast CT and DBT [66, 70–73] and constitutes a region of interest (ROI) based implementation of the Hotelling observer (HO). For brevity, we refer to it as an ROI-HO metric. Investigation of the image fidelity metrics extends our work on breast CT [73], presented in chapter 2, to a limited angular scanning geometry. Our studies focus on the behavior of these metrics with respect to voxel aspect ratio and regularization strength for Tikhonov-regularized least-squares optimization.

The chapter is organized as follows. In section 4.2, the reconstruction optimization problems, image quality metrics, and study designs are described. In section 4.3 we present the results of our investigation. The results are separated into three studies: (1) a simulation study investigating the behavior of the two image fidelity metrics with varying voxel aspect ratio and regularization strength (2) a simulation study investigating the task-based metric with reconstructions of varying regularization strength, and (3) a real data study using reconstructions of the ACR mammography phantom for visual assessment of realistic reconstructions using parameters in the ranges investigated in the simulation studies. In section 4.4 we discuss our results in greater depth. Lastly, we conclude in section 4.5.

4.2 Methods

4.2.1 Image Reconstruction Problems

LSQI - The first of two optimization reconstruction problems investigated in this manuscript is a least squares problem with identity Tikhonov regularization, referred to as LSQI. The same optimization reconstruction problem was investigated in chapter 2 in the context of breast CT, but we provide a brief review here. The optimization problem for this reconstruction formulation can be written as

$$\underset{x}{\operatorname{argmin}} \left\{ \|Ax - b\|^2 + (\lambda \|A\|)^2 \|x\|^2 \right\} \tag{P4}$$

where $x \in \Re^n$ is a pixelized image, $b \in \Re^m$ is a sinogram data vector, $A \in \Re^{m \times n}$ is a matrix modeling forward projection, and $\lambda \in \Re$ is a scalar regularization parameter. The notation $\|\cdot\|$ will be used to denote the ℓ_2 (Euclidean) norm throughout. When the argument of $\|\cdot\|$ is a matrix, it is defined to return the maximum singular value of its argument.

Identity Tikhonov regularization can be interpreted in terms of the singular value decomposition (SVD) of the system matrix A. Let $A = U\Sigma V^T$ be an SVD of A, where $\Sigma \in \Re^{m \times n}$

is a diagonal matrix with elements σ_i. The solution to P4 can be written [46]

$$x^* = V\Gamma U^T b,$$

where the diagonal matrix $\Gamma \in \Re^{n \times m}$ has elements

$$\Gamma_{ii} = \frac{\sigma_i}{\sigma_i^2 + \lambda^2 \sigma_1^2}$$

As $\lambda \to 0$, the matrix $V\Gamma U^T$ limits to the pseudo-inverse of A. The parameter λ can be interpreted as the fraction of the maximum singular value of A below which the effects of the singular value spectrum on the reconstruction are significantly diminished.

A second important observation is that

$$\lim_{\lambda \to \infty} \frac{x^*}{\|x^*\|} = \frac{A^T b}{\|A^T b\|}$$

meaning that in the limit of infinite regularization the LSQI reconstruction is visually equivalent to back-projection.

LSQD - The second problem considered is a least squares optimization with derivative Tikhonov regularization, referred to as LSQD. The optimization problem can be written

$$\underset{x}{\operatorname{argmin}} \left\{ \|Ax - b\|^2 + (\lambda \|A\| / \|D\|)^2 \|Dx\|^2 \right\} \tag{P5}$$

where $D \in \Re^{dn \times n}$ is a finite difference matrix approximation of the gradient operator, and d is the spatial dimensionality of the image array (2-D or 3-D). The ratio $(\|A\|/\|D\|)$ is employed in the regularization term to normalize the strengths of the data fidelity and regularization terms.

$$\lim_{\lambda\to\infty} \frac{x^*}{\|x^*\|} = \frac{(D^TD)^{-1}A^Tb}{\|(D^TD)^{-1}A^Tb\|}$$

meaning the reconstruction is visually equivalent to the inverse Laplacian of the back-projection image. This limit holds if the image boundary conditions are such that boundary pixels are set to zero. In our implementation of LSQD, we enforce this boundary condition.

Linearity - The solutions of problems P4 and P5 can be written as linear functions of the data vector b. Specifically, let the matrix C represent the scaled linear operator involved in regularization

$$C = \begin{cases} \lambda\|A\|I & \text{if LSQI} \\ (\lambda\|A\|/\|D\|)\, D & \text{if LSQD} \end{cases}$$

Formulate the matrix $\tilde{A}$ and the vector $\tilde{b}$ as

$$\tilde{A} \coloneqq \begin{pmatrix} A \\ C \end{pmatrix}; \quad \tilde{b} \coloneqq \begin{pmatrix} b \\ 0 \end{pmatrix} \tag{4.1}$$

Then the solution to each reconstruction problem can be written

$$x^* = \tilde{A}^\dagger \tilde{b}$$

where $\tilde{A}^\dagger$ is the pseudo-inverse of $\tilde{A}$. Since only the first m elements of $\tilde{b}$ are non-zero, we can simplify this expression by writing $\tilde{A}^\dagger$ in block-form

$$\tilde{A}^\dagger = \begin{pmatrix} R & H \end{pmatrix}$$

where $R \in \Re^{n \times m}$ and $H \in \Re^{n \times n}$ for LSQI or $H \in \Re^{n \times dn}$ for LSQD, so that

$$x^* = Rb$$

Implementation - The conjugate gradient least squares (CGLS) (ref. [44, p.289]) — see Appendix A of chapter 2 for pseudocode — algorithm was used for reconstruction for both LSQI and LSQD. The algorithm was run to numerical convergence in all cases. Direct inversion was employed in implementing the ROI-HO metric. Further details will be provided later in the manuscript when the ROI-HO metric is discussed in greater detail. The matrix A was defined using a distance driven forward projection model. [45]

FBP - In previous work we investigated parameter selection for filtered back-projection (FBP) reconstruction with a Hanning apodizing window in DBT. [66] Here we include FBP results as a reference for comparison in simulation studies. The cutoff frequency parameter for the Hanning window is specified as a fraction of the Nyquist frequency

$$\nu_{max} = \frac{1}{2\Delta u}$$

where Δu is the detector bin size. Note that decreasing the cutoff frequency in FBP reconstruction is analogous, though not equivalent, to increasing regularization strength in LSQI and LSQD reconstruction in the sense that it reduces sensitivity of the reconstruction to high-frequency components in the data. For this reason, we will refer to decreasing the Hanning window cutoff frequency as increasing the regularization strength.

In the limit of infinite regularization, the Hanning window becomes an impulse at zero frequency. In our implementation of FBP, as is common, the zero frequency value of the ramp filter is actually a small nonzero number (ref. [6, p. 74]). In the limit of infinite regularization, each projection is therefore filtered by a scaled impulse at zero frequency in the Fourier domain. This is equivalent to convolving with a constant function in the spatial domain. Each filtered projection is a constant as a function of detector bin, and the

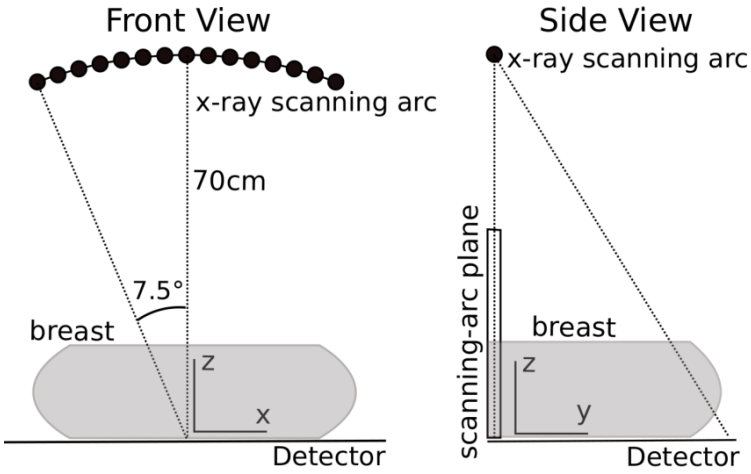

Figure 4.1: Diagram illustrating system geometry and the scanning-arc plane used for RMSE and the ROI-Hotelling observer calculations.

reconstruction is the backprojection of these “flat" projections.

4.2.2 Simulation-based Image Quality Metrics

Three image quality metrics were investigated in our studies: (1) image RMSE, (2) gradient image RMSE, and (3) an ROI-based implementation of the HO. For each of the three image quality metrics we restrict the DBT system model to a 2D plane perpendicular to the detector containing the X-ray source trajectory which we refer to throughout as the scanning-arc plane, illustrated in Figure 4.1. The idea of using the scanning-arc plane for computing the simulation-based image quality metrics is that the principle imaging properties of DBT can be captured in this plane. Use of this 2D-model also significantly decreases computation time facilitating parameter-dependence studies for accurate solution of LSQI and LSQD.

Image RMSE - Given an image vector $x_{true} \in \Re^n$ and a reconstruction $x \in \Re^n$, the image RMSE is defined as

$$\text{RMSE} = \frac{\|x - x_{true}\|}{\sqrt{n}}$$

This global image fidelity metric is a normalized version of the Euclidean distance between two image vectors. It is sensitive to the mean pixel values of the image, and in DBT, since

the reconstruction is only quasi-3D, the mean pixel values of the reconstruction can be quite different than those of the true image.

Gradient Image RMSE - In an attempt to obtain a metric with less sensitivity to the mean pixel values of reconstructions, we study the gradient image RMSE, defined as

$$\text{gradient RMSE} = \frac{\|D(x - x_{true})\|}{\sqrt{n}}$$

where, as before, $D \in \Re^{d \times n}$ is a finite differencing operator. This metric can be interpreted as the summed RMSE of the d gradient images.

ROI-HO Metric - The last metric we investigate focuses on how effectively a given task can be performed using the information within a specified ROI of a reconstruction. The figure of merit for a detection task performed by the ROI-HO is a signal-to-noise ratio (SNR), which quantifies the ability of the ROI-HO to classify a given image into one of two cases: signal-present, i.e. signal plus background, or signal-absent, i.e. background only. We apply the ROI-HO metric to two different types of detection tasks: SKE/BKE and SKE/BKS.

For the SKE/BKE detection task, the confounding physical factor is quantum noise, and the noise model is taken to be additive, zero-mean Gaussian with variance proportional to the noise-free projection of the background object. The signal is assumed small, and we employ the same noise model for signal-present and signal-absent cases.

For the SKE/BKS detection task, in addition to quantum noise, the presence of random nonuniform background structure is considered, further complicating signal detection. A statistical distribution is used to model this background variability. The model used here assumes the background structure can be described by a nonuniform component, modeled as a zero-mean stationary random process, added to a uniform background component of known attenuation. [74] A radially symmetric noise power spectrum of the form

$$h_{bg}(\nu) = \alpha|\nu|^{-\beta} \tag{4.2}$$

is considered for the nonuniform component, [75–77] with $\beta = 1.581$. [78] The value of α is chosen so that the full width at half maximum of each pixel's marginal distribution is equal to the difference between attenuation coefficients of fibroglandular and fatty breast tissue at 20keV.

The SNR for signal detection in the image is given by

$$\mathrm{SNR}_x^2 = w_x^T s_x$$

where w_x is the image domain Hotelling template, and s_x is reconstruction of the signal of interest. The Hotelling template is defined implicitly through the equation

$$K_x w_x = s_x \tag{4.3}$$

where K_x is the reconstructed image covariance matrix.

The ROI-HO is a form of the Channelized Hotelling Observer where the channels are the pixels within an ROI. In defining the ROI-HO, we perform a decimation operation $M \in \Re^{p \times n}$ which removes pixels outside of a specified ROI. The ROI is referred to as $\mathrm{ROI}_{\mathrm{HO}}$ and is illustrated schematically (ROI sizes in the Figure are not reflective of what was used in experiments) in Figure 4.2. This restricts the observer to a 0.42cm region (30 pixel width) of a single row of the reconstructed image containing the true volume of the physical signal. The resulting task is analogous to the case in 3D DBT image reconstruction of determining whether or not a signal is present from an ROI within a single axial slice of the reconstruction.

Denoting the linear reconstruction operator by $R \in \Re^{n \times m}$, the image covariance matrix after decimation can be expressed

$$K_x = MRK_b R^T M^T \tag{4.4}$$

where $K_b \in \Re^{m \times m}$ is the data covariance matrix. Due to the low dimensionality of K_x

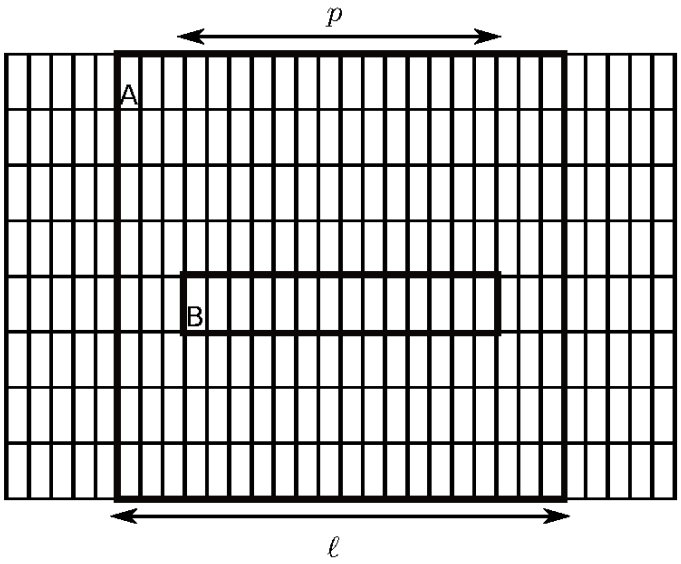

Figure 4.2: Schematic illustrating ROIs within the scanning-arc plane used in calculating the ROI-HO template. A) $\mathrm{ROI}_{\mathrm{recon}}$ used for calculating reconstruction operator. B) $\mathrm{ROI}_{\mathrm{HO}}$ used for computing signal detection signal-to-noise ratio.

resulting from the decimation operation, direct inversion of the matrix can be performed for calculation of the Hotelling template.

While decimation conveniently allows for efficient direct inversion of K_x, calculation of the reconstruction matrix R still poses a problem. Doing so directly requires pseudo-inversion of the concatenated matrix $\tilde{A}$, defined in equation 4.1. The large dimensionality of $\tilde{A}$ makes this a time consuming step. The idea of exploiting local shift invariance may help with this issue. [79, 80] For this work, however, we calculate an approximation of R using a subset of image pixels and detector bins. [72, 81] In particular, in calculating the forward projection operator A we consider only the middle $l > p$ columns of the image and, correspondingly, only the middle l detector bins in each projection. This is illustrated by $\mathrm{ROI}_{\mathrm{recon}}$ in figure 4.2. The evaluation of the regularization matrix C is similarly confined in the image space. This defines a matrix $A^{(l)} \in \Re^{m_l \times n_l}$ and a corresponding matrix $\tilde{A}^{(l)}$ of low enough dimensionality for efficient direct inversion, yielding a reconstruction operator $R^{(l)} \in \Re^{n_l \times m_l}$. The scalars m_l and n_l refer to the number of measurements and image pixels when considering only the middle l detector bins and image columns, respectively.

Referring to equation 4.4, the question of how well this approximation holds is dependent on how well the matrix $R^{(l)}K_b^{(l)}R^{(l)T}$ approximates the elements of RK_bR^T within the middle l columns of the image. As the reconstruction operator $R^{(l)}$ can vary significantly with the size of l, it is important to check that l is large enough for the approximation to be reasonable. This was done by calculating the ROI-HO metric for a range of values of l.

Instead of reporting SNR_x directly, we report the efficiency ϵ which relates SNR_x to the HO SNR for signal detection in the projection data domain

$$\text{SNR}_b^2 = s_b^T(K_b^{-1}s_b),$$

where s_b is the projection of the signal of interest. The expression in the parenthesis is the data domain Hotelling template.

The efficiency [82] is then written as

$$\epsilon = \frac{\text{SNR}_x^2}{\text{SNR}_b^2}.$$

The efficiency is less than or equal to one for linear image reconstruction and it is a measure of how well the relevant information for performing a given task was preserved through the reconstruction and decimation procedure.

In order to compare detection performance for SKE/BKE and SKE/BKS tasks directly, we will report the relative efficiency for SKE/BKS tasks, which we define as

$$\epsilon_r = \frac{\text{SNR}_{x,bg}^2}{\text{SNR}_b^2}.$$

where $\text{SNR}_{x,bg}^2$ is the image domain ROI-HO SNR for an SKE/BKS task and SNR_b is the data domain HO SNR for an SKE/BKE task. The relative efficiency ϵ_r for a SKE/BKS task will always be less than the efficiency ϵ for the corresponding SKE/BKE task. Due to the common normalization factor, comparison of the SKE/BKE efficiency ϵ with the SKE/BKS

relative efficiency ϵ_r is equivalent to comparing their image domain squared SNRs.

Subjective visualization - Along with plots of the image quality metrics, we show reconstructed images corresponding to some investigated parameter settings to allow for comparison of metrics with subjective visualization of the 2D-model DBT reconstructions. In addition, we also show 3D DBT images reconstructed from phantom data acquired with a DBT scanner.

4.2.3 DBT simulation studies

We present two specific DBT simulation studies that characterize parameter dependences of image reconstruction by LSQI and LSQD. The simulation studies have two purposes: (1) to demonstrate applicability of the presented image quality metrics, and in the process, (2) to reveal important characteristics of linear iterative image reconstruction for DBT. The simulation studies are not meant to be comprehensive as the main purpose is the development and demonstration of the image quality metrics.

Simulation System Geometry - For the real data studies, projection data was acquired using a Hologic Selenia Dimensions unit. For simulation studies, the 2D system geometry was defined to mimic the geometry of the measurements taken by a single detector row of the Hologic system. Specifically, the radius of the source trajectory and source-to-detector distance were both taken to be 70 cm and 15 simulated projections were acquired in 1 degree increments. The detector bin size was taken to be 0.14 mm.

Simulation study 1: Pixel anisotropy and regularization strength

The first study aims at characterizing image reconstruction by LSQI and LSQD as a function of pixel anisotropy and regularization strength for a pseudo-continuous model of mean DBT data. The dominant feature of the DBT scanning system is its limited scanning angular range. This causes the inherent resolution of the DBT system to be highly anisotropic. Accordingly, this first study focuses on setting the pixel aspect ratio and the impact of

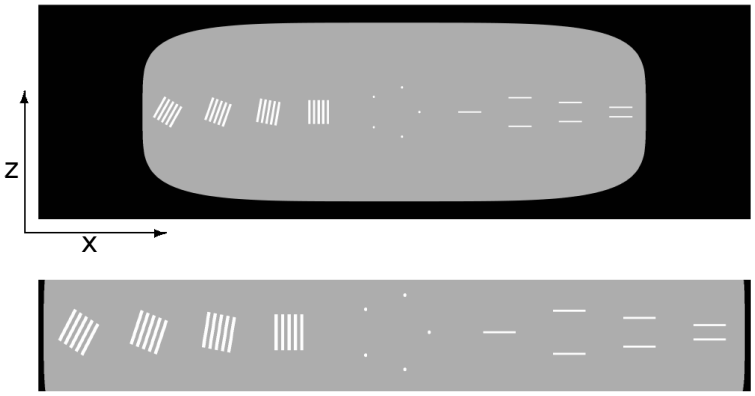

Figure 4.3: Simulation phantom used for RMSE studies (top) and ROI for visualization (bottom). Coordinate axis directions are also shown. Attenuation coefficients for each part of the phantom were evaluated at 20 keV. The background is fatty tissue, while the bars on the left and lines on the right are fibroglandular. The lines on the right are interpreted as cross sections of disks in the plane parallel to the detector in 3D. The specks in the center are calcium and are displayed at 5 times actual size for ease of visualization. Display window: [0.15, 0.60] cm^{-1}.

regularization, isolating the limited scanning angular range aspect of the DBT system. The idea is to characterize what features of the test object can be recovered from the DBT sampling conditions and how well the RMSE-based metrics reflect the recovery of visual features.

For this first study, akin to the studies in chapter 2, a discrete phantom is defined on a high-resolution grid with pixels much smaller than the detector bins so that its projection yields pseudo-continuous data. The pixel grid is 4096×4096 with x × z dimensions 20.5 cm × 4.5 cm and pixel dimensions of 50 µm × 11 µm. An image of the phantom is shown in Figure 4.3 along with the axis directions. The x axis lies parallel to the detector plane. The bars on the left provide visual assessment of resolution at small angles from the horizontal axis. The disks on the right are meant for both evaluating detection of large, low contrast signals and assessing resolution in the vertical direction. This phantom is defined in the scanning-arc plane and its use for visualization is non-standard, because it is oriented perpendicular to the usual 3D DBT slice images. Visualization of reconstructions in this non-standard orientation is simplified by the phantom's uncomplicated design.

Data was generated by projecting the phantom onto the detector line at 100 times the de-

tector bin resolution using the line-intersection method. This high-resolution projection was subsequently converted to X-ray transmission employing Beer's law, assuming monochromatic X-rays at 20 keV. The transmission factors were then averaged within each detector bin, then converted back to projection data by taking the negative logarithm. Reconstruction was performed onto grids covering the same region as the high resolution grid on which the phantom was defined. The x pixel dimension of reconstructions was held constant at 0.14mm — matched to the detector bin size — while the z pixel dimension was varied.

The image RMSE was calculated by first resampling, via nearest-neighbor interpolation, the reconstructed image to the high-resolution grid, then calculating the RMSE. The gradient RMSE was evaluated by calculating a finite difference approximation of the gradient at the reconstructed resolution then resampling the x and z direction gradient images to the high resolution grid. Resampled gradient images were compared to the gradient images of the phantom to calculate the gradient image RMSE. Both metrics were plotted as a function of the pixel aspect ratio, defined as the ratio of z to x pixel dimension. This process was repeated to obtain RMSE curves at different regularization strengths. For reference, FBP reconstructions were performed at an aspect ratio of 1.0. This aspect ratio for FBP was picked because it yielded the minimum gradient image RMSE.

Simulation study 2: ROI-HO detection efficiency as a function of regularization strength

The second study improves on the data model realism of the first study by including quantum noise and characterizes image reconstruction as a function of regularization strength for LSQI and LSQD. The impact of the regularization strength is quantified by the ROI-HO detection efficiency ϵ.

We investigate two types of detection tasks as defined in section 4.2.2: SKE/BKE and SKE/BKS. For SKE/BKE tasks, observer performance is purely quantum limited, and the task does not challenge the reconstruction to resolve the signal of interest from other nearby

structures which can differ between data sets. An SKE/BKE task only challenges the reconstruction to keep the signal distinguishable from the quantum noise. An SKE/BKS task with nonuniform background further challenges the reconstruction to resolve the signal from variable background structure. In DBT, background structure is of particular importance due to blur in the depth direction.

Two signals were considered for investigation in both SKE/BKE and SKE/BKS detection tasks. The first signal was a 0.25 cm disk lying parallel to the detector plane with X-ray attenuation coefficient equal to that of fibroglandular breast tissue at 20keV. As the study was performed in 2D with a slice perpendicular to the detector plane, a cross section of the disk — i.e. a rectangle — was used as the signal. The second signal was a 0.32 mm micro-calcification modeled as a Gaussian with full width at half maximum (FWHM) equal to the calcification's width.

For the SKE/BKE tasks, a uniform 4.2 cm $\times$ 4.2 cm background was considered using the attenuation coefficient of fatty tissue at 20 keV. For the SKE/BKS tasks, the average of the attenuation coefficients of fatty and fibroglandular tissues at 20 keV was used for the known uniform component of the background.

The size of $\mathrm{ROI}_{\mathrm{HO}}$ was held at $p = 30$ throughout (see Figure 4.2), while the size of $\mathrm{ROI}_{\mathrm{recon}}$ was varied from 40 to 70 or 70 to 100 for LSQI and LSQD reconstruction, respectively. The x pixel dimension of reconstructions was 0.14 mm and the aspect ratio was 9.2.

The quantum noise model is based on a Gaussian approximation to Poisson noise. The variance of the sinogram data for the SKE/BKE tasks is (ref. [83, p. 542])

$$\mathrm{Var}(b_i) = \frac{1}{\bar{N}_i} + \frac{1}{\bar{N}_0}$$

where $\bar{N}_0$ denotes the average number of incident X-rays and $\bar{N}_i$ denotes the mean number of detected photons in the i^{th} ray after passing through the object. The mean X-ray

transmission is

$$\bar{N}_i = \bar{N}_0 \exp(-\bar{b}_i),$$

where the mean projection is computed in the same way described in Sec. 4.2.3. The data was assumed to be a vector of identically independently distributed (i.i.d.) Gaussian random variables, and accordingly, off-diagonal elements of the covariance are zero. Explicitly, the data domain covariance for the SKE/BKE task is

$$(K_{b,\mathrm{BKE}})_{ij} = \begin{cases} \frac{1}{\bar{N}_i} + \frac{1}{\bar{N}_0} & \text{if} \quad i = j \\ 0 & \text{if} \quad i \neq j \end{cases}. \tag{4.5}$$

To calculate K_b for the SKE/BKS task, the image domain background noise model given in equation 4.2 is propagated through the projection model and added to the quantum noise via the equation

$$K_{b,\mathrm{BKS}} = A K_{bg} A^T + K_{b,\mathrm{BKE}}$$

where K_{bg} is the covariance matrix of the variable background. The fact that the contributions of the quantum noise and background variability to the data covariance matrix are additive has been demonstrated in ref. [74]. The image covariance matrix K_{bg} is calculated from the variable background noise power spectrum via the equation

$$K_{bg} = W^* \,\mathrm{diag}(u) W$$

where W is the matrix representation of the discrete Fourier transform (DFT), u is a vector with elements equal to discrete samples of h_{bg}, and $\mathrm{diag}(u)$ is a diagonal matrix with diagonal elements u.

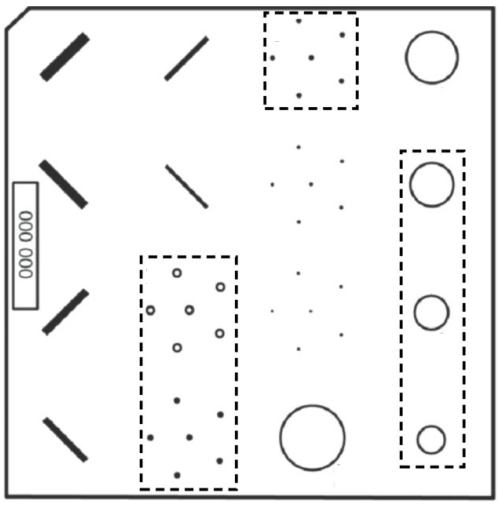

Figure 4.4: Diagram of ACR phantom. Dashed ROIs are used for visualization in the ACR study.

4.2.4 Real data study: ACR phantom data

In order to show the potential relevance of the 2D ROI-HO metric to the actual 3D DBT system we present 3D DBT reconstructed images by LSQI and LSQD for physical phantom data. Projection data were acquired for the mammography accreditation phantom listed by the American College of Radiology (ACR) for measuring the physical standards baseline in mammography since the beginning of the Mammographic Quality Standards Act (MQSA). Reconstruction was performed onto a grid of pixels with $\mathrm{x} \times \mathrm{y} \times \mathrm{z}$ pixel dimensions $0.14\,\mathrm{mm} \times 0.14\,\mathrm{mm} \times 1.3\,\mathrm{mm}$, where z is the direction perpendicular to the detector plane. Note the same x pixel dimension was used in the simulation studies. The three ROIs indicated in Figure 4.4 were chosen for visual evaluation of reconstructions.

To obtain reconstructions more representative of the 2D SKE/BKS detection tasks, a realization of nonuniform background structure was simulated, projected, and added to the measured data prior to reconstruction. The realization of nonuniform background was simulated by filtering white noise with the square root of h_{bg} in equation 4.2 as described in detail in ref. [84].

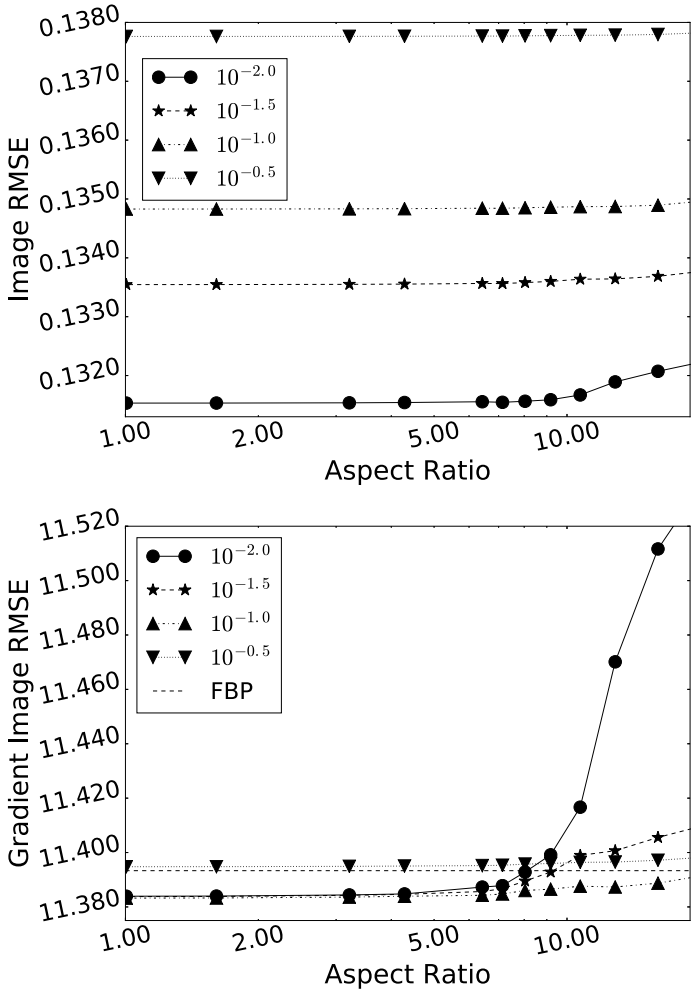

Figure 4.5: Image RMSE (top) and gradient image RMSE (bottom) as a function of relative pixel size at four regularization strengths for LSQI reconstruction. Legends indicate value of regularization parameter λ.

4.3 Results

4.3.1 Simulation study 1: Pixel anisotropy and regularization strength

LSQI - Image and gradient image RMSE curves from LSQI reconstructions are shown in Figure 4.5. The image RMSE of the FBP reconstruction is not shown in the top panel because it lies at value of 0.289, far above the RMSE of the LSQI reconstructions. This results from the FBP reconstruction having almost no DC component. Image RMSE is seen to be relatively insensitive to aspect ratio while increasing with increasing regularization

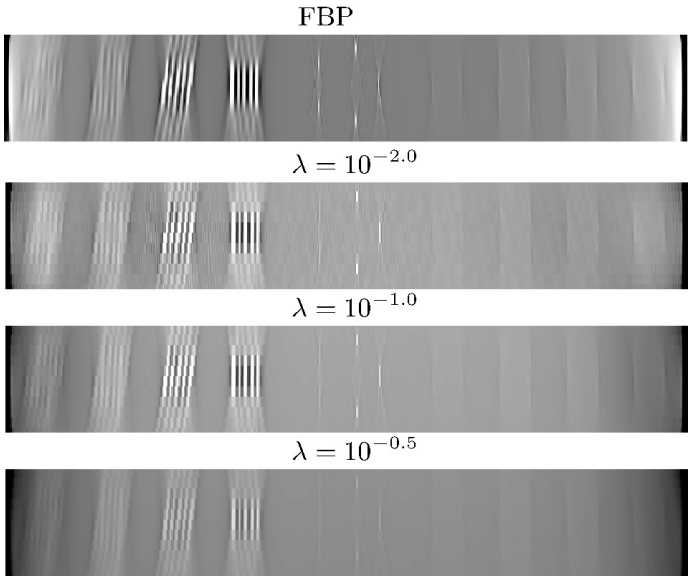

Figure 4.6: FBP reference and LSQI reconstructions at three different regularization strengths at an aspect ratio of 10.7. LSQI display window: [0.15, 0.55] cm^{-1}. FBP display window: [-0.05,0.06] cm^{-1}

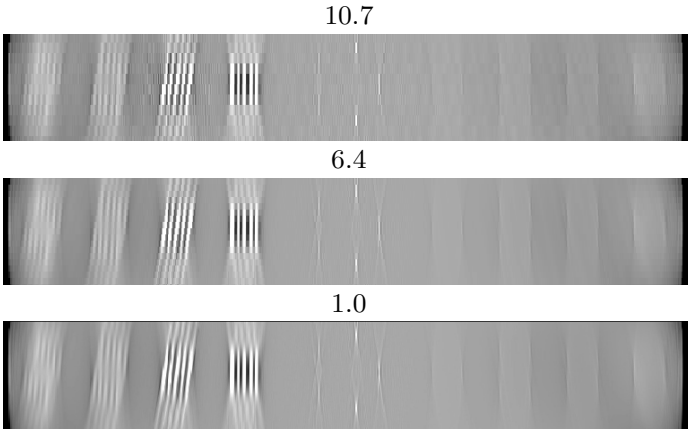

Figure 4.7: LSQI reconstructions at $\lambda = 10^{-2.0}$ and three aspect ratios. Aspect ratios are displayed above each image. Display window: [0.15, 0.55] cm^{-1}.

strength. The gradient image RMSE shows a decreasing trend with decreasing aspect ratio for each level of regularization, noting that the curves for $\lambda \leq 10^{-1.0}$ exhibit more of a plateau for aspect ratios ≤ 5.0.

The rank order of the curves appears to switch rapidly for aspect ratios in the range of 8.0 to 10.0, and the sensitivity of this metric with regularization strength appears to increase with aspect ratio during and beyond this critical range. We note that, for all aspect ratios,

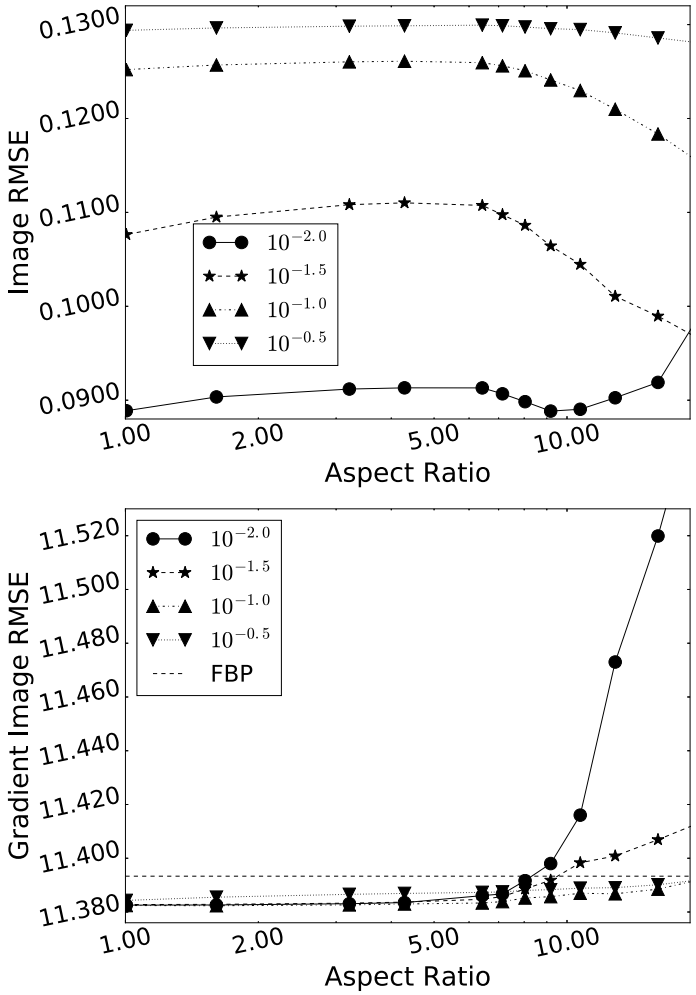

Figure 4.8: Image RMSE (top) and gradient image RMSE (bottom) as a function of relative pixel size at four regularization strengths for LSQD reconstruction. Legends indicate value of regularization parameter λ.

image RMSE favors the smallest shown regularization strength of $\lambda = 10^{-2.0}$, while gradient image RMSE favors $\lambda = 10^{-1.0}$.

The image dependence of the regularization strength is seen in Figure 4.6 in which reconstructions at a fixed aspect ratio of 10.7 are shown. This aspect ratio is chosen for visualization because both RMSE measures show sensitivity to regularization strength at 10.7. At the lowest shown regularization strength $\lambda = 10^{-2.0}$, there are clear high frequency artifacts. These artifacts decrease in conspicuity with increasing regularization. The reconstructed images also show increased blur and decreased mean value as regularization strength increases. We also note that the FBP image appear to be of comparable image quality to the

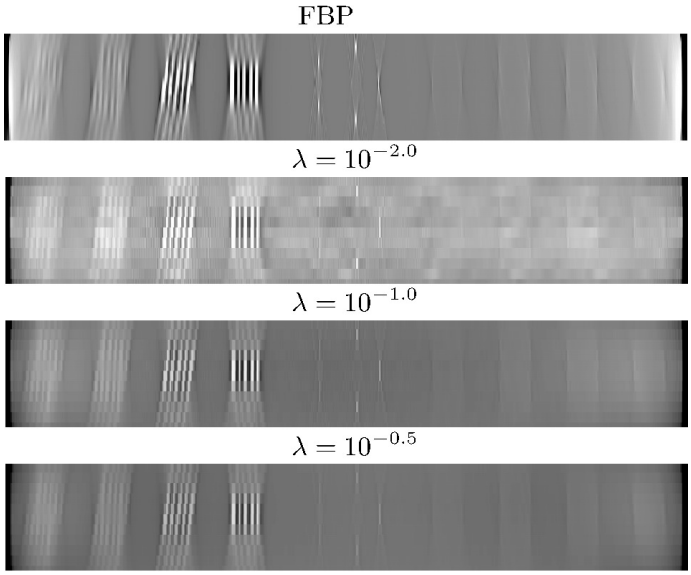

Figure 4.9: LSQD reconstructions at three different regularization strengths at an aspect ratio of 10.7. Display window: [0.15, 0.65] cm^{-1}. FBP display window: [-0.05,0.06] cm^{-1}

LSQI images. Image RMSE ranks these images in the order of best to worst as $\lambda = 10^{-2.0}$, $10^{-1.0}$, $10^{-0.5}$, and FBP, with FBP being "off-the-charts" bad. Gradient image RMSE ranks the images in the order $\lambda = 10^{-1.0}$, FBP, $\lambda = 10^{-0.5}$, and $10^{-2.0}$. The latter ordering of gradient image RMSE appears to be more in line with subjective visualization of the images in Figure 4.6.

In Figure 4.7, reconstructions at three aspect ratios are shown at a constant level of regularization for $\lambda = 10^{-2.0}$. This value is chosen because image RMSE dependence of aspect ratio is nearly constant, while gradient image RMSE shows much variation particularly for large aspect ratios. Again, subjective visualization agrees more with the gradient image RMSE trend.

LSQD - Image and gradient image RMSE curves for LSQD reconstruction are shown in Figure 4.8. The trends of these curves are quite similar to those of LSQI shown in Figure 4.5. The main difference is that the image RMSE curve for LSQD does actually show some non-trivial dependence on aspect ratio as opposed to the nearly constant dependence shown for LSQI. Again, the FBP image RMSE value is not indicated in Fig. 4.8, because it is much larger than the shown values for LSQD.

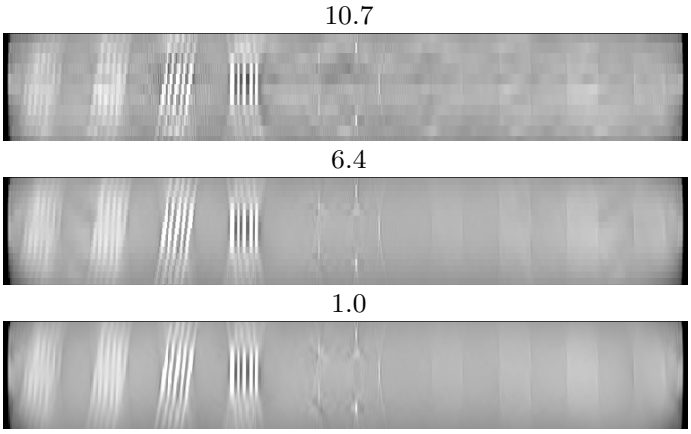

Figure 4.10: LSQD reconstructions at $\lambda = 10^{-2.0}$ and three aspect ratios. Aspect ratios are displayed above each image. Display window: [0.15, 0.65] cm^{-1}

For the same fixed values of pixel aspect ratio and regularization strengths used for the LSQI, Figures 4.9 and 4.10 show reconstructed image dependences on λ and pixel aspect ratio, respectively. As before with LSQI, the visual subjective image quality trend in both figures aligns more with image gradient RMSE than it does with image RMSE.

4.3.2 Simulation study 2: ROI-HO detection efficiency as a function of regularization strength

SKE/BKE Tasks

LSQI - Figure 4.11 shows the ROI-HO detection efficiency ϵ in LSQI reconstruction as a function of regularization strength for the two SKE/BKE detection tasks and 4 values of the $\text{ROI}_{\text{recon}}$ size parameter l. Recall from section 4.2.3 that $\text{ROI}_{\text{recon}}$ is used to estimate the reconstruction operation R, and does not change the decimation operator M, which is held constant throughout. The efficiency curves appear to approach a limiting curve as the value of l is increased, suggesting that the largest value employed ($l = 70$) provides a good approximation of the behavior of the ROI-HO. We therefore limit our discussion to this value of l for the LSQI results.

The efficiency curves are monotonically increasing with increasing regularization strength

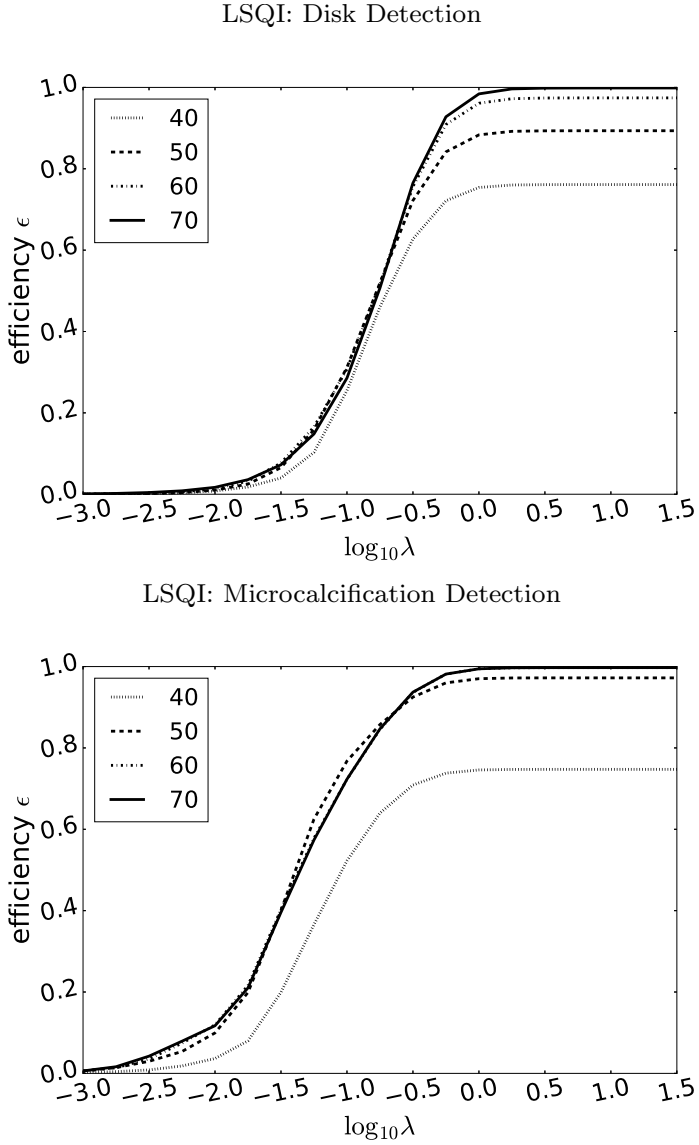

Figure 4.11: Hotelling observer efficiency ϵ for LC disk (top) and HC calcification (bottom) SKE/BKE detection tasks as a function of regularization strength for LSQI reconstruction. Legends indicate size of ROI (value of l) used for estimating the reconstruction operator.

for both tasks, starting from a low-efficiency plateau, then rising and saturating at a large efficiency which is close to the theoretical maximum of $\epsilon = 1.0$. The location and width of the transition as a function of λ clearly depends on the characteristics of the signal. The saturation of the efficiency curves suggests that there is a point beyond which increasing regularization does not further improve preservation of task relevant information through the reconstruction. Also, there is no penalty in terms of HO SNR for detection for increasing

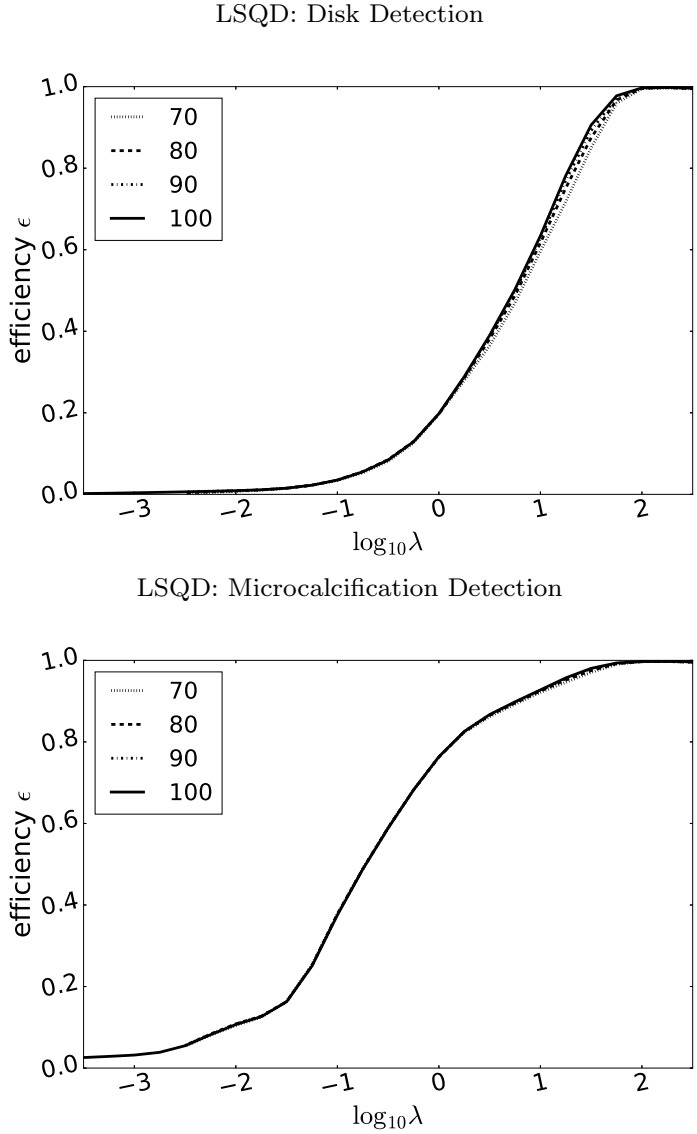

Figure 4.12: Hotelling observer efficiency ϵ for LC disk (top) and HC calcification (bottom) SKE/BKE detection tasks with variable background as a function of regularization strength for LSQD reconstruction.

the regularization strength arbitrarily. Recall from section 4.2.1 that the LSQI reconstructed image approaches the back-projection image as $\lambda \to \infty$.

LSQD - Figure 4.12 shows the efficiency curves for LSQD reconstruction. The efficiency curves again approach a limit with increasing values of l, in this case suggesting the value of $l = 100$ yields a reasonable approximation of the ROI-HO. Similar to LSQI, the efficiency saturates with increasing regularization strength in a signal-dependent manner.

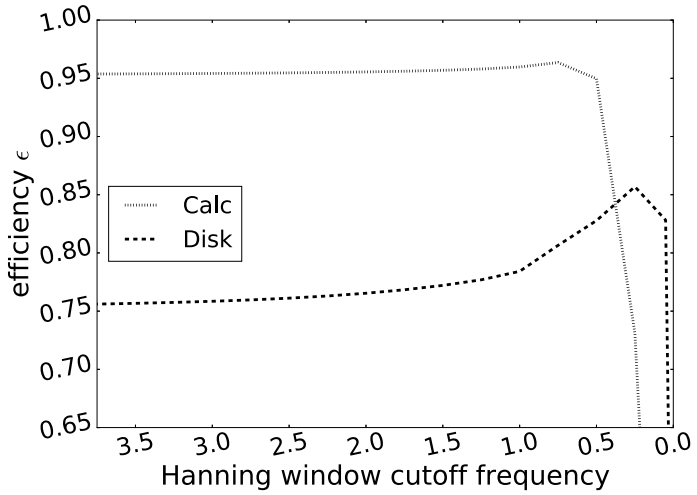

Figure 4.13: Hotelling observer efficiency ϵ for LC disk and HC calcification SKE/BKE detection tasks as a function of spectral filter cutoff frequency for FBP reconstruction. Note the x-axis is inverted so regularization strength increases from left to right.

FBP - Figure 4.13 shows the efficiency for FBP reconstructions of varying cutoff frequency for the Hanning apodizing window. The x-axis of the plot has been inverted so that regularization increases from left to right, consistent with the LSQI and LSQD efficiency curves.

By contrast to the LSQI and LSQD efficiency curves, the FBP efficiency curves do not display saturating behavior with increasing regularization strength, instead indicating that an SNR penalty is incurred for apodizing too heavily for a quantum noise limited task. Recall that in the limit of infinite regularization, the FBP algorithm convolves each projection with a constant function prior to back-projection.

In the limit of decreasing regularization strength, a plateau in efficiency is observed. In this limit the reconstruction algorithm approaches FBP with a pure ramp filter, so the level of the plateau is representative of the efficiency of FBP with no apodization. Moving further to the right, a monotonic increase in efficiency is observed prior to a peak. The location of the peak appears to be signal dependent, paralleling the signal-dependent location of the transition region in the efficiency curves for LSQI and LSQD. Note that in both cases, the location the of the peak/transition region for calcification detection occurs at lower

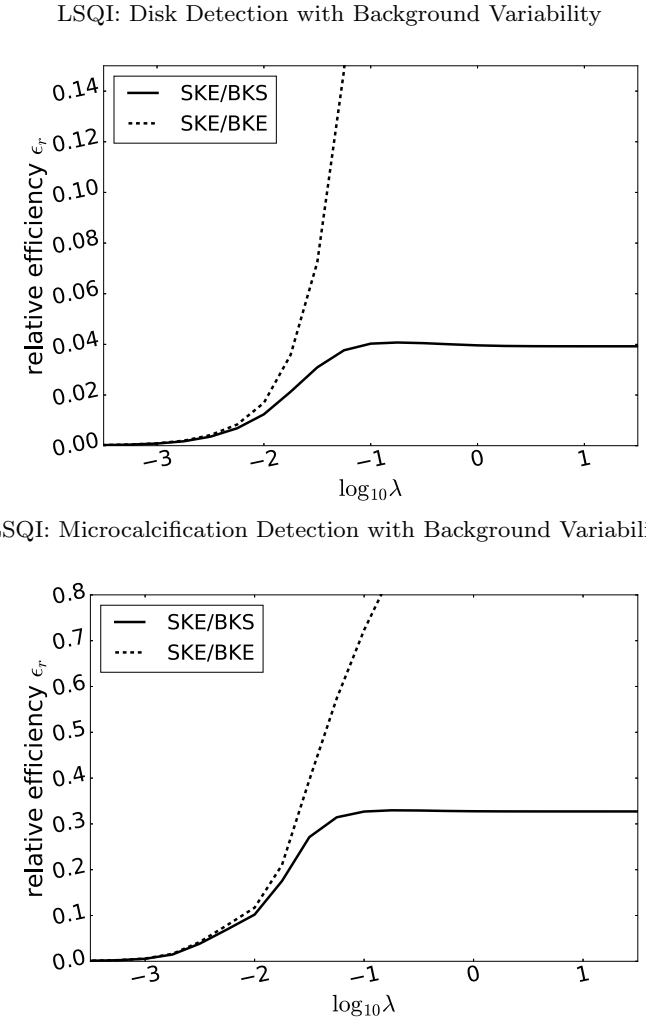

Figure 4.14: Hotelling observer relative efficiency ϵ_r for LC disk (top) and HC calcification (bottom) SKE/BKS detection tasks as a function of regularization strength for LSQI reconstruction. Dashed lines show HO efficiency ϵ for the corresponding SKE/BKE task.

regularization strength than for disk detection.

SKE/BKS Tasks

LSQI - Figure 4.14 shows the ROI-HO relative detection efficiency ϵ in LSQI reconstruction as a function of regularization strength for the two SKE/BKS detection tasks alongside the ROI-HO detection efficiencies for the corresponding SKE/BKE tasks. Based on the limiting behavior observed in the SKE/BKE tasks, only the $l = 70$ $\text{ROI}_{\text{recon}}$ results are shown.

The relative efficiencies show a clear decrease in task performance relative to the quantum

Figure 4.15: Hotelling observer relative efficiency ϵ_r for LC disk (top) and HC calcification (bottom) SKE/BKS detection tasks as a function of regularization strength for LSQD reconstruction. Dashed lines show HO efficiency ϵ for the corresponding SKE/BKE task.

limited SKE/BKE case for both tasks, though the magnitude of the drop in SNR due to the presence of background variability is greater for the disk detection task than for the calcification detection task. Aside from this decrease in task performance, the overall trends in the efficiency curves are quite similar to their SKE/BKE counterparts. That the curves plateau at large regularization strengths indicates that the SNR is not penalized for increasing regularization strength arbitrarily, even in the presence of a variable, nonuniform background.

At low regularization strengths, the relative efficiency curves of the SKE/BKS tasks track well with the efficiency curves of the SKE/BKE tasks. The curves separate at intermediate

regularization strengths suggesting that the main contributing factor to SKE/BKS task performance at low regularization strengths is quantum noise while at large regularization strengths it is background variability. The nonuniform background variability limits the extent to which increasing regularization can improve task performance, as indicated by the lower regularization strengths at which the curves saturate for SKE/BKS tasks relative to SKE/BKE tasks.

LSQD - Figure 4.15 shows the corresponding results for LSQD reconstruction for the two SKE/BKS detection tasks. The observed behavior is largely similar to the LSQI results, with saturating behavior again occurring at large regularization strengths and a signal dependent transition region. We do note that the SNR drop for disk detection is again greater than that for calcification detection.

4.3.3 Real data study: ACR phantom data

No added background

LSQI - ROIs of reconstructions of the ACR phantom with LSQI at three different levels of regularization, alongside a back-projection reconstruction, are shown in Figures 4.16 and 4.17. The ROIs are shown on a diagram of the ACR phantom in Figure 4.4 for reference. Display windows for each reconstruction were manually chosen based on subjectively maximizing visibility of the disks or specks. We note that the values of λ used in the real data reconstructions may not precisely match those used in the 2D simulation studies.

As a general trend the reconstructed disks and specks appear more conspicuously as the noise-level is reduced by increasing regularization strength for the shown values of λ. Furthermore, there is good correspondence between the LSQI image for the largest shown λ-value and the back-projection image.

The background noise texture differs significantly between the four reconstructions, with the magnitude of fluctuations decreasing with increasing regularization strength. It is evident

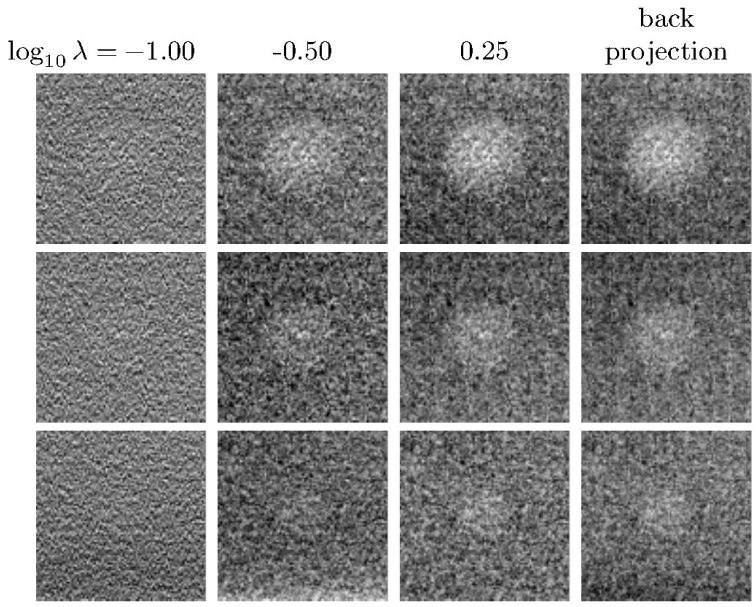

Figure 4.16: ROIs of LSQI reconstructions containing 0.25, 0.5, and 0.75cm disks of ACR phantom. Regularization increases from left to right. Back projection image is shown for reference.

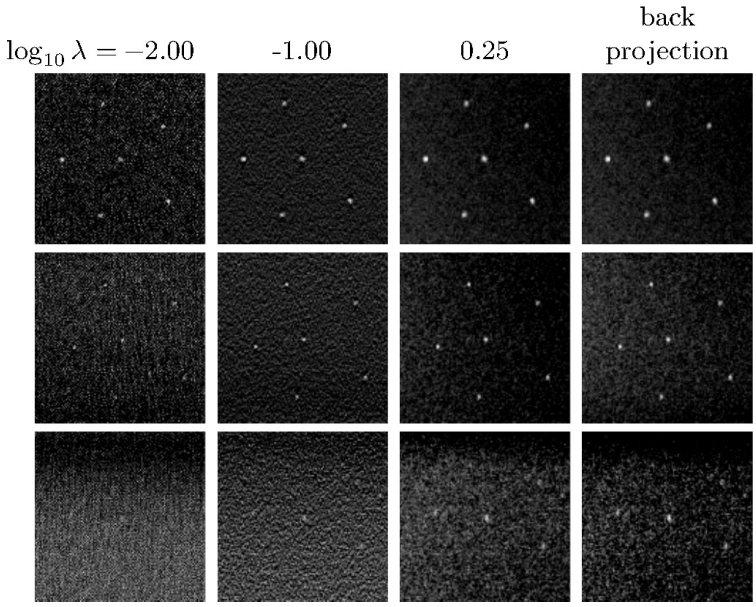

Figure 4.17: ROIs of LSQI reconstructions containing 0.54, 0.40 , and 0.32 mm specks of ACR phantom. Regularization increases from left to right. Back projection image is shown for reference.

from the figures how the detection of large low-contrast and small high-contrast objects could be complicated by this texture in under-regularized reconstructions.

LSQD - Figures 4.18 and 4.19 show the analogous results for LSQD reconstruction except

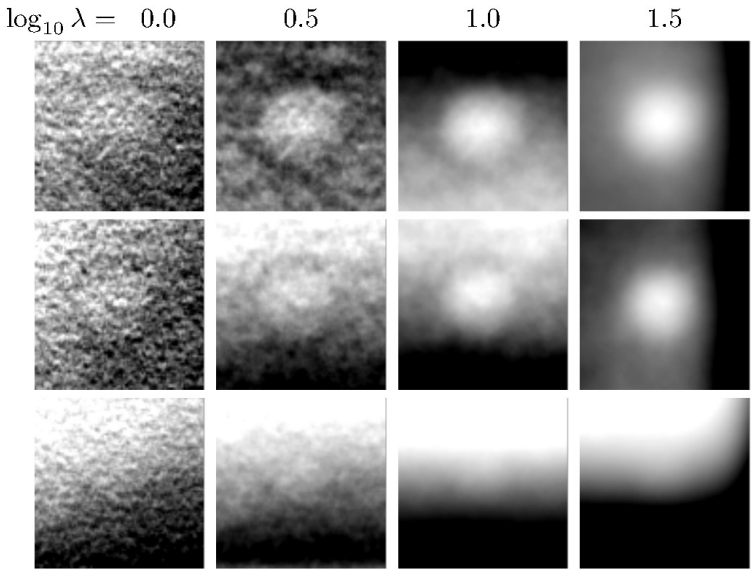

Figure 4.18: ROIs of LSQD reconstructions containing 0.25, 0.5, and 0.75cm disks of ACR phantom. Regularization increases from left to right.

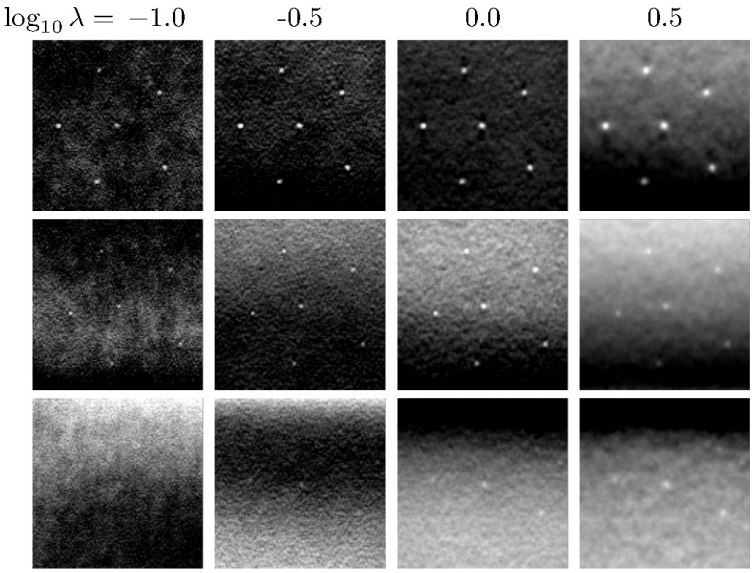

Figure 4.19: ROIs of LSQD reconstructions containing 0.54, 0.40 , and 0.32 mm specks of ACR phantom. Regularization increases from left to right.

that no back-projection image is shown. As with LSQI, higher levels of regularization reduce the magnitude of background noise variation; however, there is a clear difference in noise texture. Increasing regularization of course also blurs the disk and speck signals.

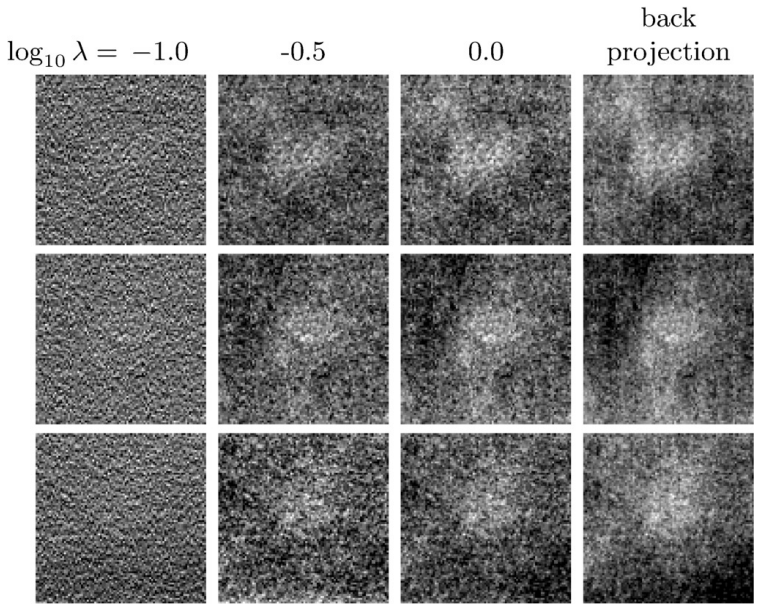

Figure 4.20: ROIs of LSQI reconstructions of altered ACR phantom data with added nonuniform background. ROIs contain 0.25, 0.5, and 0.75cm disks of ACR phantom. Regularization increases from left to right. Back projection image is shown for reference.

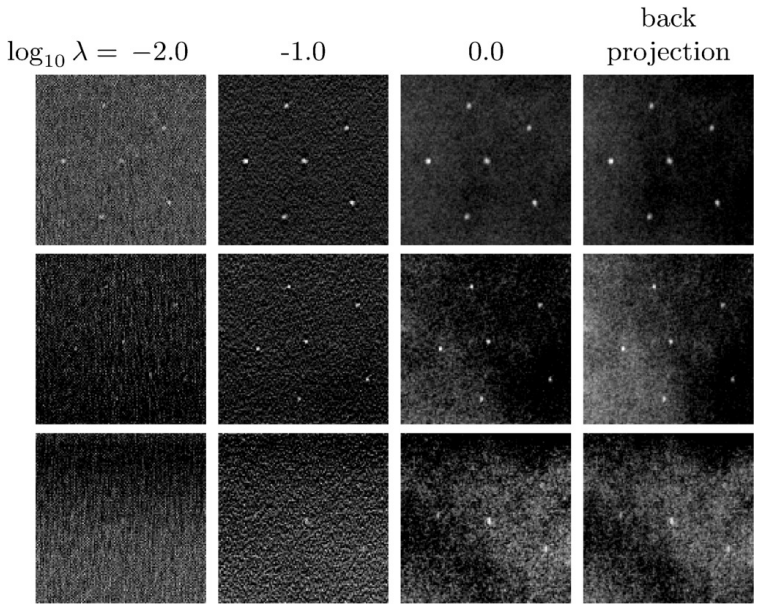

Figure 4.21: ROIs of LSQI reconstructions of altered ACR phantom data with added nonuniform background. ROIs contain 0.54, 0.40 , and 0.32 mm specks of ACR phantom. Regularization increases from left to right. Back projection image is shown for reference.

Added nonuniform background

LSQI - Figures 4.20 and 4.21 show ROIs of reconstructions of the ACR phantom in which the projection of a nonuniform background was added to the data as described in section .

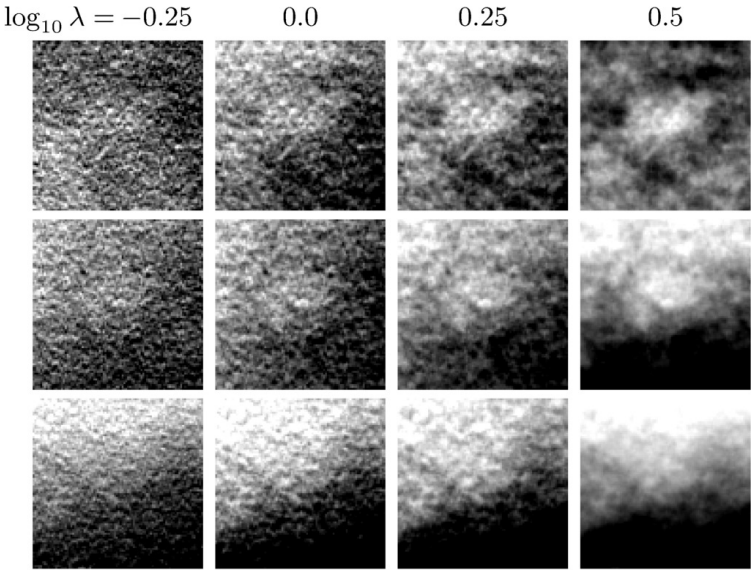

Figure 4.22: ROIs of LSQD reconstructions of altered ACR phantom data with added nonuniform background. ROIs contain 0.25, 0.5, and 0.75cm disks of ACR phantom. Regularization increases from left to right.

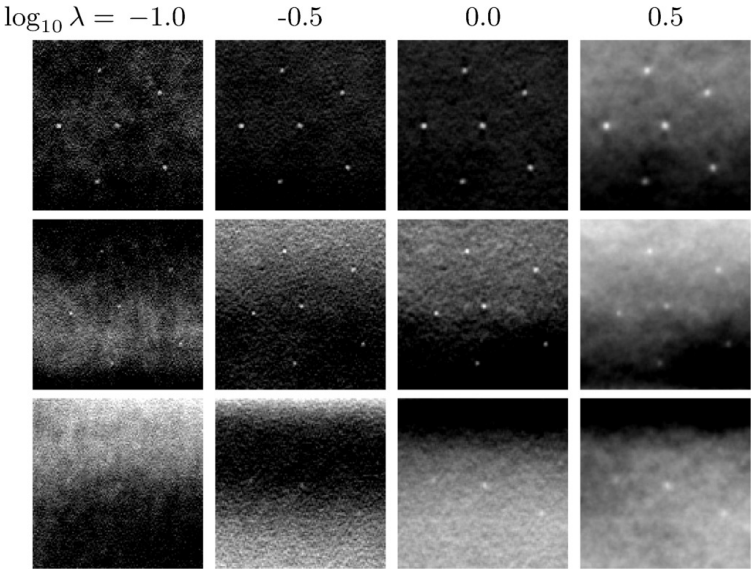

Figure 4.23: ROIs of LSQD reconstructions of altered ACR phantom data with added nonuniform background. ROIs contain 0.54, 0.40 , and 0.32 mm specks of ACR phantom. Regularization increases from left to right.

Note the the regularization parameter values for the displayed images are not identical to those shown in the corresponding results of Figures 4.16 and 4.17.

A general trend of increasing conspicuity with increasing regularization is still apparent in the presence of nonuniform background structure. Relative to the unaltered data recon-

structions, the background texture, particularly at large regularization strengths, contains more low-frequency structure, hindering visualization of the disk and speck signals. These observations are consistent with trends observed in the ROI-HO SKE/BKS simulation studies.

LSQD - Figures 4.22 and 4.23 show the corresponding results for LSQD reconstruction. As with LSQI, the trend of increasing conspicuity with regularization strength is maintained in the presence of a nonuniform background, though there is an apparent reduction in conspicuity of the disks relative to the unaltered data case. Conspicuity of the specks appears to be less affected by the nonuniform background (compare Figures 4.19 and 4.23).

4.4 Discussion

image RMSE - The sensitivity of image RMSE to changes in mean pixel value appears to make it inappropriate for meaningful characterization of image reconstruction parameters for DBT. From the results shown the image RMSE does not follow the subjective visual quality of the reconstructed images from the 2D DBT simulation. Perhaps the most egregious discrepancy occurs in the image series comparing use of various regularization strengths for LSQI, in Figure 4.6, and LSQD, Figure 4.9, with FBP. The FBP result has an image RMSE which is more than twice that of any of the shown LSQI or LSDQ images, yet it is subjectively competitive with any of these images.

gradient image RMSE - We observe that the gradient image RMSE is not as sensitive to changes in mean pixel value and appears to reflect visual changes between different regularization strengths and aspect ratios. In particular, an increase in gradient image RMSE is observed at large aspect ratios for $\lambda = 10^{-2.0}$, reflecting the appearance of high frequency artifacts in both the LSQI and LSQD images shown in Figures 4.7 and 4.10, respectively. Moreover, in the image sequences varying regularization strength in Figures 4.6 and 4.9, the rank ordering suggested by the gradient image RMSE seems plausible even including the FBP images.

We caution, however, that these studies are preliminary and that many more empirical studies are needed to support the utility of the gradient image RMSE metric for image reconstruction parameter characterization in DBT. One peculiar aspect of this metric is that the relative magnitude of the variations of gradient image RMSE shown in Figures 4.5 and 4.8 amount to 1% to 2% over the shown parameter ranges. Yet, the preliminary results from subjective visualization seem to indicate that these small variations are meaningful. That gradient image RMSE exhibits such behavior for DBT image reconstruction is perhaps not too surprising, because the metric is still essentially comparing reconstructed images from very limited angular-range scanning with perfect tomographic image reconstruction. By its design, the gradient image RMSE is most sensitive to discrepancy at edge discontinuities at the borders of various tissues within the subject. It is known that image reconstruction from a limited scanning-angular range such as in DBT can only recover a small subset of these edges [85].

ROI-HO efficiency for signal detection - The results of the second simulation study demonstrate that the proposed ROI-HO implementation can be used to accurately calculate ROI-HO efficiencies for the SKE/BKE and SKE/BKS detection tasks in linear optimization-based image reconstruction for the 2D-DBT model in the scanning-arc plane. Due to non-locality of image reconstruction in general, it is not obvious that restricting the image reconstruction operator to an ROI with the image will yield accurate image domain HO SNR values. That we observe a saturation of efficiency values (hence image domain SNR) with ROI length ℓ in Figures 4.11 and 4.12 indicates that the ROI approximation can yield accurate results. We expect that ROI-HO efficiency for the 2D DBT model should reflect HO efficiency for 3D DBT, because the 2D model captures the most important scanning geometry features of 3D DBT. This correspondence, however, needs to be demonstrated, and we will do so in future work.

Examining the SKE/BKE task efficiency curves in more detail, both Figures 4.11 and 4.12 indicate low efficiency at low regularization strength. This efficiency loss is primarily

due to the fact that we are modeling single-slice viewing with the decimation operation that limits the reconstruction to the line in the 2D DBT model (corresponding to a plane in 3D DBT), where the signal for detection exists. In this line, the signal is reconstructed at an amplitude lower than the true signal due to DBT depth blur, yet noise from the data model is amplified in the viewing line due to low regularization. Both LSQI and LSQD saturate at nearly a perfect efficiency of 1.0 with increasing λ, where LSQI and LSQD images limit to back-projection and the inverse Laplacian of back-projection images, respectively.

In comparing FBP and LSQI/LSQD for the SKE/BKE detection task, there are substantial differences in how the respective regularization parameters impact signal detection efficiency, highlighting the differences between these algorithms.

Turning to the SKE/BKS tasks, one might expect that with the incorporation of a nonuniform background variability model, the need for the reconstruction algorithm to resolve the signal from the background would cause a penalty to SNR at large regularization strengths for LSQI and LSQD. Contrary to this expectation, we observed monotonically increasing efficiency with increasing regularization as in the SKE/BKE tasks. The nonuniform background variability instead appeared to play the role of limiting the extent to which increasing regularization could improve task performance, while not penalizing the SNR for further increases in regularization beyond the point at which efficiency saturates.

We also noted that the decrease in SNR relative to the SKE/BKE tasks was much greater for disk detection than calcification detection. This result suggests that the stationary process used to model nonuniform background variability interferes more with detection of large, low-contrast objects than small, high-contrast objects. This is consistent with the slowly spatially varying appearance of realizations of this background model (see, e.g., ref. [84]).

In relation to other work on using the HO for image quality assessment in DBT, which employ noise realizations [62–65, 67, 69] and/or assumptions of stationary noise [65, 67, 68] in estimating image statistics, the current approach yields highly accurate values subject only

to minor numerical error due to computer precision. The drawback of our ROI-HO implementation is that it is based on simulation and cannot be applied directly to reconstructed images from actual DBT systems.

3D DBT image reconstruction of the ACR phantom- The ACR phantom study provides a realistic visual assessment of images reconstructed in the parameter ranges investigated in the second simulation study for the ROI-HO signal detection efficiency. The viewing conditions for the unaltered data reconstructions are similar to the SKE/BKE signal detection task design. The properties of the signals, disks and speck clusters, are known to the observer, see Figure 4.4; also the background is uniform and therefore also known to the observer. The properties of the signals of the 2D simulation study are modeled loosely on the disk and speck objects of the ACR phantom.

The main trend seen in the unaltered ACR data reconstructions for LSQI and LSQD is that increasing regularization appears to increase the conspicuity of both disk and speck cluster signals. This trend appears to coincide with the SKE/BKE ROI-HO efficiency trends for LSQI and LSQD. For ACR results with LSQI, in particular, the $\lambda = \infty$ images, a.k.a. back-projection, appear to show similar conspicuity for both disks and specks as the results from the largest finite regularization strength of $\lambda = 10^{0.25}$ in Figures 4.16 and 4.17. This result is somewhat indicative of the detection efficiency plateau seen at large λ in Fig. 4.11. We do point out, however, that the growing magnitude of background variations relative to the blurred signal complicates visualization at high regularization strengths for LSQD.

The apparent trend of increasing conspicuity with regularization for both disk and speck cluster signals is also observed in the ACR reconstructions in which a nonuniform background was incorporated into the data. This observation is consistent with the SKE/BKS ROI-HO efficiency trends. We note in particular that the conspicuity of the signals does not appear to be reduced at large regularization strengths, contrary to what one may expect with a nonuniform background.

We note that the correspondence between the 2D DBT ROI-HO results and 3D DBT ACR

reconstructed images represent only preliminary indications as many more empirical results are needed. Again, the connection between the 2D DBT ROI-HO with a 3D DBT ROI-HO needs to be established. We also point out the SKE/BKS results represent a single parameter setting of a single background variability model. Other background variability models [65,86] may yield different detection efficiency curves. Another important point is that the ROI-HO yields image domain signal detection SNR, while for the results with the ACR phantom we only discussed signal conspicuity. Signal conspicuity and detection, although related, are not the same thing. Closer visual correspondence with ROI-HO SNR can be investigated by designing and performing two-alternative forced choice experiments [70](ref. [32, p. 819]). We also note that LSQI and LSQD are not commonly used in the clinic.

Application of image quality metrics - The metrics adapted and investigated here yield useful information for setting parameters in linear iterative image reconstruction, but they alone do not provide a complete picture and they are meant to compliment other image quality metrics developed for DBT systems parameter characterization/optimization. In particular, consider the results of the ROI-HO SKE/BKE signal detection task efficiency for LSQD and LSQI; following the curves shown in Figures 4.11 and 4.12 alone suggests use of LSQI and LSQD with extremely large regularization parameter λ. We point out, however, that the ROI-HO signal detection efficiency exhibits a plateau at large λ, and considering these curves together with other metrics such as the gradient image RMSE suggests instead to employ a regularization strength at the low λ end of the plateau.

4.5 Conclusions and Future Work

We have investigated three simulation-based image quality metrics for use in the selection of parameters for linear iterative image reconstruction in DBT. In the process, we have adapted an RMSE-based metric to DBT, and developed a task-based metric for linear iterative image reconstruction in DBT. The imaging properties of DBT led us to modify image RMSE to a gradient image RMSE. We have also extended our work on ROI-HO signal detection efficiency

for filtered back-projection [72] to linear iterative image reconstruction. Finally, we showed images reconstructed from simulated 2D DBT data and ACR phantom 3D DBT data to provide a subjective visual assessment of image reconstruction algorithm parameter trends. The results demonstrated that sensitivity to mean pixel value is a weaknesses of the image RMSE in the context of DBT. Eliminating dependence on mean pixel value by the proposed gradient image RMSE appears to rectify the short-comings of image RMSE. The results also demonstrated a signal-dependent saturating behavior of the ROI-HO efficiency for two SKE/BKE and SKE/BKS signal detection tasks with increasing regularization strength.

Future work will focus on extending the simulation studies from 2D to 3D in order to quantify the correspondence of the 2D DBT model in the scanning arc plane with full 3D DBT. While the RMSE-based metrics can be applied to any image reconstruction algorithm including non-linear iterative image reconstruction, the current version of the ROI-HO applies only to linear image reconstruction. Methodology on developing noise properties for non-linear image reconstruction, [87, 88] may allow extension of the ROI-HO to non-linear image reconstruction algorithms. Finally, we intend to extend the ROI-HO to more realistic signal detection models where only statistical knowledge is available for the signal is available. Such a model is expected to be more sensitive to DBT depth resolution than the ROI-HO for a SKE/BKE or SKE/BKS detection task.

CHAPTER 5

ORIENTATION DEPENDENCE OF FIBER-LIKE SIGNAL CONSPICUITY IN DIGITAL BREAST TOMOSYNTHESIS

5.1 Introduction

In the last chapter, we investigated simulation-based metrics for characterizing iterative image reconstruction in DBT. In one of the presented studies, a model observer metric, referred to as the ROI-HO, was used to investigate the detectability of two rotationally-symmetric signals: (1) a small, high-contrast speck and (2) a large, low-contrast disk. Among the work devoted the optimization of acquisition [17, 59–61, 63, 65, 67–69, 89–94] and reconstruction [16, 17, 62, 64, 89, 95–97] parameters in DBT, the vast majority has focused on these two canonical tasks.

Since DBT is an inherently anisotropic imaging modality, it is also important to characterize parameter dependence for signals without rotational symmetry. This is especially the case since there are a number of clinically relevant tasks for which the signal of interest is asymmetric. The detection and visual assessment of spiculated lesions, Cooper's ligaments, and blood vessel all fall into this category. Many of these tasks involve the detection and visualization of thin, fiber-like signals, which can exhibit orientation dependent variations in conspicuity in DBT. [98] It remains unclear how this orientation dependence varies with different reconstruction algorithms and parameter settings.

In this chapter we seek to characterize the interplay between reconstruction parameter selection and orientation dependent signal conspicuity for the task of detecting a thin, fiber-like signal in DBT. Our studies focus on the regularization strength dependence of two iterative reconstruction methods and two methods of regularization in filtered backprojection (FBP). We perform simulation studies to characterize performance of the four algorithms with respect to signal appearance, signal conspicuity, and resolution. To establish relevance of the simulation results we compare with visualization of reconstructed images from physical

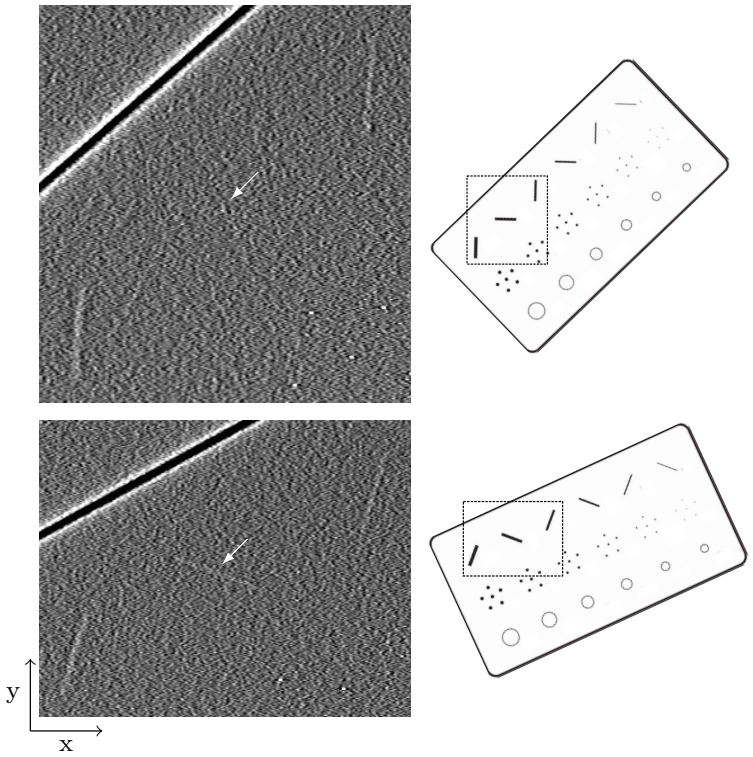

Figure 5.1: FBP reconstructions of the ACR digital mammography accreditation phantom at two orientations. In the top image the rods are oriented at approximately 0° and 90° with respect to the x-axis. In the bottom they are oriented at approximately 20° and 70°. Data for both orientations was acquired using the same technique. Arrows in each ROI point to second thickest fiber, which exhibits improved conspicuity in the 20° orientation.

phantom and patient data.

The chapter is organized as follows. In section 5.2, we provide a brief example to illustrate the extent to which orientation dependence can be present in DBT and motivate the studies that follow. In section 5.3 the data model, reconstruction algorithms, and study design are described. In section 5.4 we present the results of our investigation. The results are separated into three studies: (1) a simulation study investigating the orientation dependence of signal conspicuity as a function of regularization strength, (2) a physical phantom study employing the ACR digital mammography accreditation phantom for visual assessment of fibers using regularization strengths determined from simulation, and (3) a breast data study investigating orientation dependent conspicuity in the presence of realistic background structure. The results are discussed further in section 5.5, and conclusions are presented in section 5.6.

5.2 Orientation Dependence in DBT

As mentioned in the previous section, fiber-like structures are involved in a number of clinically relevant tasks in DBT, including the detection of Cooper's ligaments, spiculated lesions, and blood vessels. To illustrate the importance of orientation dependence on fiber conspicuity in DBT, Figure 5.1 shows reconstructions of three fibers from the ACR digital mammography accreditation phantom at two orientations. The second largest diameter fiber in particular exhibits orientation dependent conspicuity, being barely visible in the top panel but clearly identifiable in the bottom. The orientation dependent reduction in conspicuity even causes the third thickest fiber to appear more conspicuous than the second thickest in the top panel.

This example clearly demonstrates that fiber-like signals can exhibit orientation dependent conspicuity in DBT. Note that fibers do not exhibit orientation dependent conspicuity in X-ray projection data, so this orientation dependence is introduced by the reconstruction algorithm. The purpose of this work is to investigate the extent to which reconstruction algorithm design can be tailored to remove this orientation dependence.

5.3 Methods

5.3.1 System Geometry

Data for both physical phantom and patient studies was acquired using a Hologic Selenia Dimensions tomosynthesis unit. Refer to Figures 1.2 or 4.1 for a schematic of the system. For ease of reference we repeat the system parameters here. The radius of the source trajectory and the source-to-detector distance are both 70 cm and 15 projections are acquired in 1 degree increments. The detector bin size is 0.14 mm.

In the present studies, calibration matrices [99] — matrices mapping 3D spatial coordinates to 2D detector coordinates for a given view — were obtained from geometric calibration of the system and used to define the system geometry for both simulation and real data reconstructions.

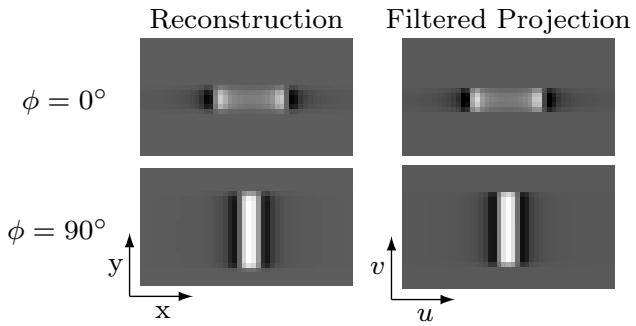

Figure 5.2: FBP reconstruction (left) and filtered central projection (right) of a rod signal at two orientations. The ramp filter was apodized by a Hanning window with $\nu_c = 1.0$ in generating the filtered projection data and the reconstruction.

5.3.2 Image Reconstruction Methods

In the previous chapter, we performed studies characterizing the parameter dependence of one analytic — FBP — and two linear iterative — LSQI and LSQD — algorithms with respect to detection of small, high-contrast specks, and large low-contrast disks. [96, 97] We consider these algorithms again in addition to a variant of FBP designed to mitigate the loss of DC component common to FBP reconstructions in DBT [17]. As this loss of DC component results from the filtering operation, which causes the orientation dependence of FBP reconstructions (see Figure 5.2), the expectation is that this variant will exhibit reduced orientation dependence compared to FBP.

In the following discuss the four reconstruction algorithms investigated in this manuscript: FBP, mFBP, LSQI, and LSQD. We begin with a detailed description of FBP and an explanation of why FBP reconstructions can exhibit orientation dependent conspicuity in DBT. We subsequently describe a modified version of FBP intended to mitigate this orientation dependence. We refer the readers to chapter 4 for a detailed description of the two iterative methods, LSQI and LSQD.

FBP - The first algorithm investigated is FBP with a Hanning apodizing window

$$H(\nu) = \begin{cases} \frac{1}{2}\left(1 + \cos\left(\pi \frac{\nu}{\nu_H}\right)\right) & |\nu| < \nu_H \\ 0 & \text{else} \end{cases}$$

where H is the definition of the Hanning window and ν_H is the cutoff frequency of the window.

We specify the cutoff frequency ν_H as a fraction of the detector's Nyquist frequency ν_{max}

$$\nu_{max} = \frac{1}{2\Delta u}$$
$$\nu_c = \frac{\nu_H}{\nu_{max}}$$

where ν_c is the fractional cutoff frequency and Δu is the detector bin size. The cutoff frequency controls the noise-resolution tradeoff in FBP reconstruction, analogous, though not equivalent, to the regularization parameter in iterative methods. Decreasing cutoff frequency is analogous to increasing regularization strength, and we will therefore often refer to decreasing the cutoff frequency as increasing the regularization in FBP.

For FBP, the reconstruction operation can be expressed in the form

$$R_{\text{FBP}} = A^T S$$

where A^T denotes the backprojection operation and $S \in \Re^{m \times m}$ performs the ramp filter with Hanning window apodization. In discrete form, the ramp filter can be implemented in the discrete Fourier transform (DFT) domain via multiplication with a diagonal matrix Ω containing the DFT domain ramp kernel. The Hanning window can be implemented similarly with a diagonal matrix Λ. Denoting the DFT operator by W, we have

$$S = W^{-1}\Omega\Lambda W$$

For further details, see ref. [6, ch. 3].

Note the filter in FBP is applied only in the direction on the detector parallel to the direction of source travel, which we label the u-direction. It is this one-dimensional filtering that can cause orientation dependence in FBP. This is illustrated in Figure 5.2 where we show noiseless FBP reconstructions of a fiber at two orientations alongside the central view of the filtered projection data. Due to the extremely limited angular range of DBT, the reconstructed signals and filtered projection data appear almost identical. This demonstrates that the orientation dependence is primarily attributable to the filter. In the results, we further characterize the orientation dependence of FBP as a function of the width of the Hanning apodizing window. We also investigate a modification to the low frequency response of the filter, which is described next.

mFBP - FBP reconstructions in DBT have almost no DC component due to the low-frequency response of the ramp filter [97]. In an attempt to mitigate this effect, the next algorithm investigated is a variant of FBP in which the ramp filter is modified to take higher values at low frequencies. The modified ramp filter takes the form

$$R_\tau(\nu) = \begin{cases} \tau + \frac{1}{4\tau}\nu^2 & |\nu| \leq 2\tau \\ |\nu| & \text{else} \end{cases}$$

We specify the parameter τ as a fraction δ of the detector's Nyquist frequency

$$\delta = \frac{\tau}{\nu_{max}}$$

We also employ Hanning window apodization in the mFBP implementation with a cutoff frequency of $\nu_c = 1.0$. We note that similar modifications to the ramp filter have been proposed in the context of increasing the signal to noise-ratio of large, low-contrast objects [20] and reducing metal artifacts [100].

The modified filter is shown with different values of δ in Figure 5.3. Note that increasing

the value of δ, and thereby increasing the low-frequency response of the filter, increases blurring in the sinogram domain and is therefore, in some sense, a form of regularization. We will therefore refer to increasing δ as increasing the regularization in mFBP.

Implementation - As in the previous chapter, for LSQI and LSQD, the conjugate gradient least squares (CGLS) (ref. [44, p. 289]) algorithm was used for reconstruction. The algorithm was run to numerical convergence in all cases.

Pyramidal image volume - The Hologic system reconstructs images onto a pyramidal volume to correct for the effects of magnification due to the extremely limited angular range. Denoting the x, y, and z indices of each voxel by i, j, and k, respectively, the location of the center of each voxel is given by

$$\begin{aligned}
\mathrm{x}(i,j,k) &= \frac{(C - k\Delta\mathrm{z})}{C}\,(i\Delta\mathrm{x} - L/2) \\
\mathrm{y}(i,j,k) &= \frac{(C - k\Delta\mathrm{z})}{C}\,(j\Delta\mathrm{y}) \\
\mathrm{z}(i,j,k) &= k\Delta\mathrm{z}
\end{aligned}$$

where Δx, Δy, and Δz are the x, y, and z voxel dimensions, respectively, in the detector plane, C is the radius of the source trajectory, and L is the length of the detector in the u direction. Note the x and y voxel dimensions decrease in planes further from the detector while the z voxel dimension remains constant. Note also that in this formulation the $k = 0$ index corresponds to the detector plane. Each in-plane slice — slices parallel to the detector plane — is displayed at the same size for viewing despite the difference in x-y voxel dimensions between planes.

In our studies, reconstructions were performed onto a pyramidal volume with $\Delta\mathrm{x} = \Delta\mathrm{y} = 0.14\,\mathrm{mm}$, matched to the detector bin size, and $\Delta\mathrm{z} = 1.3\,\mathrm{mm}$.

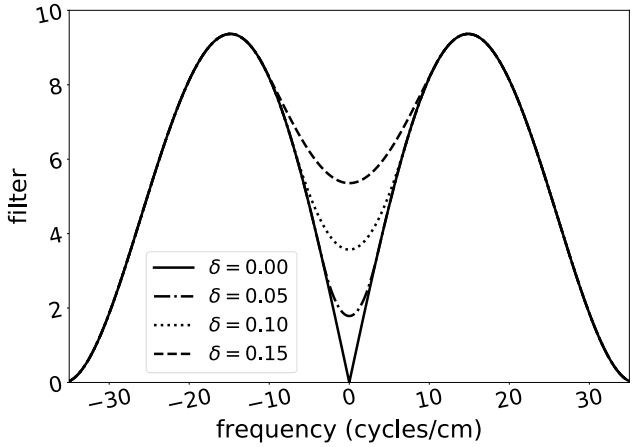

Figure 5.3: Filter used in mFBP reconstruction at four settings for the parameter δ. Note the setting $\delta = 0.0$ corresponds to regular FBP reconstruction with a Hanning apodizing window with cutoff frequency $\nu_c = 1.0$.

Figure 5.4: In-plane slice of simulation phantom employed in characterization studies of FBP, LSQI, and LSQD, and mFBP.

5.3.3 Simulation Studies

Simulation studies were performed to characterize the interplay between orientation and regularization strength dependence of reconstructed fiber signals in DBT for each of the reconstruction methods. The signal of interest in the study is a rod of 1.9 mm length and 0.61 mm width. The rod was chosen to be relatively short based on the observation that fiber-like objects in the breast — lesion spiculations, Cooper's ligaments, blood vessels, etc. — often follow tortuous paths. The rod is intended to represent a small section of a fiber-like signal in the breast with the idea being that orientation dependent conspicuity of such a section could cause a fiber signal to appear "disconnected" in a reconstructed image.

The studies can be broken down into two parts. First we generate reconstructions of the fiber-like signal from noisy data to allow for visual assessment of the orientation dependence of signal conspicuity. Next, we utilize simulation-based metrics to characterize the resolution

of reconstructions and shape of reconstructed signal profiles as a function of signal orientation and regularization strength.

Reconstructions from Noisy Data

For the noisy data study, a discrete phantom containing 10 rotated rod signals, illustrated in Figure 5.4, was defined on a high-resolution grid with isotropic voxels 20 time smaller than the detector bins so that projection would approximate that of a continuous object. The rod signals were oriented in angular increments of 10° over a range of 0° to 90° with respect to the x-axis. The attenuation coefficient of the signals was taken to be that of fibroglandular tissue at 20keV. A uniform background having the attenuation coefficient of fatty tissue at 20keV was included in the phantom.

Noiseless data was generated from the high-resolution sampling of the phantom. The noiseless sinogram data was then converted to mean transmission data employing Beer's law and assuming 1.5×10^4 incident photons per ray. Mathematically, denoting the noiseless sinogram data by $\bar{b}$, the mean transmission data $\bar{g}$ is given by

$$\bar{g} = I_0 e^{-\bar{b}}$$

where $I_0 = 1.5 \times 10^4$ is the number of incident photons per ray and the exponent is taken element-wise. Noisy data g was generated by sampling a Poisson distribution with mean $\bar{g}$. The noisy transmission data g was then converted back to sinogram data via the equation

$$b = -\log \frac{g}{I_0}$$

Reconstructions from the noisy data were run at varying levels of regularization for each of the four algorithms.

Simulation-based Metric Studies

Assessment of Resolution- Resolution was assessed by calculating point response functions for each reconstruction algorithm. A 0.14mm diameter speck was defined on a high-resolution volume, as described in the noisy data study. The speck was forward projected and reconstructed using each of the algorithms at varying regularization strengths to obtain point response functions. No noise was added to the data prior to reconstruction.

Resolution Metrics - To assess x resolution, profiles of the point response function along the x-axis were plotted and normalized to the value of the signal in the voxel in which it was physically contained. Denoting the unnormalized point response function by p we have

$$\mathrm{PRF(x)} = \frac{p(\mathrm{x}, \mathrm{y}_0, \mathrm{z}_0)}{p(\mathrm{x}_0, \mathrm{y}_0, \mathrm{z}_0)}$$

where PRF denotes the normalized point response function and $(\mathrm{x}_0, \mathrm{y}_0, \mathrm{z}_0)$ is the location of the true physical signal.

Assessing the z-resolution in tomosynthesis is complicated by the fact that the (x, y) coordinates of the maximum value of the point response in each z-plane can vary. This is related to the so-called ghosting artifact in which objects appear out of focus in planes not containing the object. [16] To address this issue, we the take the maximum value of the point response function over each z-plane and normalize to the value of the signal in the voxel in which it is physically contained. The resulting quantity is equivalent to one common variant of the artifact spread function (ASF) applied to a 0.14 mm diameter speck. [59] Since the ASF is often applied to extended objects, we denote the quantity by pASF to emphasize that it is the ASF applied to a point source. The pASF can be mathematically expressed

$$\mathrm{pASF(z)} = \frac{\max_{\mathrm{x,y}} p(\mathrm{x}, \mathrm{y}, \mathrm{z})}{p(\mathrm{x}_0, \mathrm{y}_0, \mathrm{z}_0)}$$

Orientation Dependence of Signal Profiles - This portion of the simulation study aims at characterizing reconstructed in-plane signal profiles as a function of signal orientation and regularization strength for each of the reconstruction methods. The limited angular scanning range of the DBT system can cause reconstructed objects to have considerably different profiles than the true underlying objects they represent. The idea of this study is to isolate the impact of the limited angular scanning range on the orientation dependence of signal profiles and quantify the extent to which signal profiles match the underlying objects they are meant to capture.

The simulation phantom shown in Figure 5.4 was again employed in this study, except the fatty tissue background was removed. The phantom was sampled onto a high-resolution grid as described in the previous studies. Data was generated by distance driven forward projection of the high-resolution phantom. Reconstructions were performed onto pyramidal volumes as described in section 5.3.2. The in-plane slice of the reconstruction containing the true signal volume was extracted and resampled, via nearest-neighbor interpolation, to the high-resolution grid. Regions of interest (ROIs) were placed around each reconstructed rod signal. The voxel values of the reconstructed ROI were then compared to the corresponding ROIs in the high resolution phantom using a modified version of the root mean square error (RMSE). We describe this metric below.

Scaled Image RMSE Metric - The absolute voxel values in tomosynthesis reconstruction typically differ quite significantly from the attenuation coefficients of the underlying true object, rendering the image RMSE ineffective for quantifying the extent to which an object has been recovered. In previous work, we proposed a gradient RMSE to remove the DC component of the image, thus avoiding this issue. [97]

As we are interested here in quantifying the resemblance of the reconstructed signal profiles to the underlying signal, we propose another variant of the RMSE in which we compare the underlying signal and a scaled version of the reconstructed signal. This scaling is performed separately for each ROI. We denote this quantity by $s(\phi)$ for emphasis that

the scaling is different for each signal angle. Mathematically, denoting the vector of true and reconstructed voxel values within an ROI containing a single of angle ϕ by $f_{\text{true}}(\phi)$ and $f_{\text{recon}}(\phi)$, respectively, we have

$$s(\phi) = \frac{\|f_{\text{true}}(\phi) - \alpha(\phi) f_{\text{recon}}(\phi)\|}{\sqrt{n_{\text{ROI}}}}$$

where n_{ROI} is the number of voxels in the ROI and $\alpha(\phi)$ is the scaling parameter. The value of $\alpha(\phi)$ is determined by minimizing the norm of the difference between the true and scaled reconstructed voxel values

$$\alpha(\phi) = \underset{\alpha}{\text{argmin}} \{\|f_{\text{true}}(\phi) - \alpha f_{\text{recon}}(\phi)\|\}$$

It can be shown that the appropriate value is given by

$$\alpha(\phi) = \frac{f_{\text{recon}}(\phi)^T f_{\text{true}}(\phi)}{\|f_{\text{recon}}(\phi)\|^2}$$

5.3.4 Real Data Studies

Two real data studies were performed using data acquired with a Hologic Selenia Dimensions unit. The purpose of the studies is to demonstrate that the orientation dependence of signal detectability observed in the idealized simulation studies is still observed in the presence of other physical factors and more realistic background structures.

For the physical phantom study, projection data were acquired with the American College of Radiology (ACR) digital mammography accreditation phantom. The phantom was scanned at two orientations with a 29 kVp tube voltage and 45 mAs tube current. The nylon fibers in the phantom were positioned at 0° and 90° with respect to the x-axis in the first orientation and 20° and 70° in the second. In the second study, we reconstructed breast data scanned in the mediolateral oblique (MLO) orientation. Reconstructions were performed onto a pyramidal grid of pixels with x × y × z dimensions 0.14 mm × 0.14 mm ×

1.3 mm in the detector plane.

Nonuniform background correction - With breast data, raw mFBP, LSQI, and LSQD reconstructions exhibit a nonuniform background in which the reconstruction has higher values near the middle of the breast and lower values near the skin line. Regular FBP reconstructions do not exhibit this same phenomenon because the ramp-filter removes low-frequency variations in the background. The slowly varying background in mFBP, LSQI, and LSQD reconstructions make it impossible to view sizable regions of the breast in as narrow a viewing window as possible with an FBP reconstruction.

A polynomial background correction was performed to allow for better visual comparison of the mFBP, LSQI, and LSQD reconstructions. First, the breast volume was segmented by thresholding. Then, in a slice by slice fashion, the segmented volume was fit to a 2D 4^{th} order polynomial via linear least squares. Each slice of the image was divided by the corresponding polynomial fit. Such a background correction was only performed in the breast data reconstructions.

5.4 Results

The results are organized as follows. In section 5.4.1, we present the results of the simulation studies, which investigate the tradeoff between orientation dependence and resolution for each of the four algorithms. The results of these studies are used to inform the selection of regularization strengths for reconstructions from real data in sections 5.4.2 and 5.4.3. In particular, the simulation studies are used to determine a regularization strength for each algorithm for which z-resolution is matched but orientation dependence is reduced for LSQI, LSQD, and mFBP relative to FBP. The real data studies are then used to corroborate this simulation result.

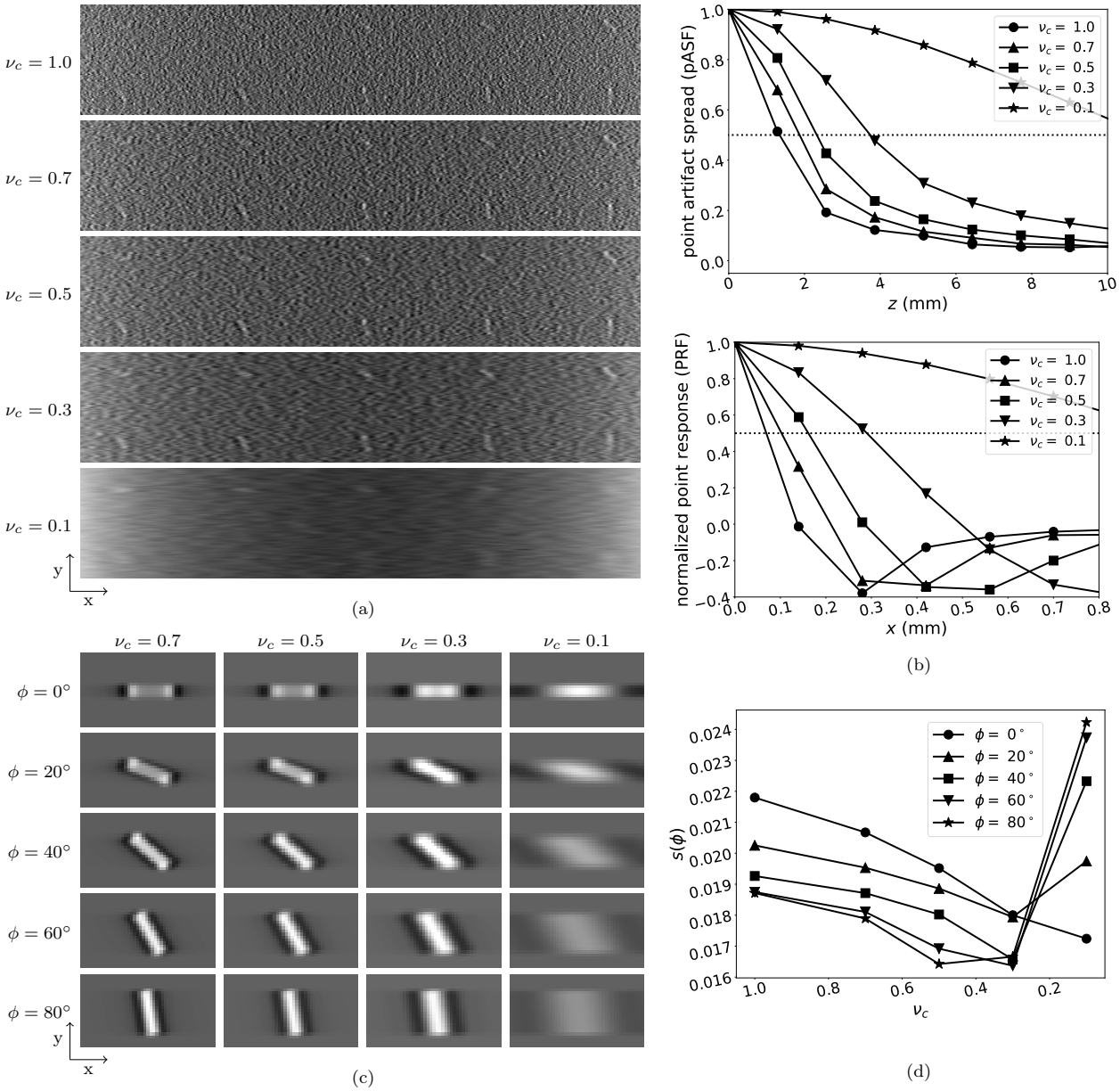

Figure 5.5: a) FBP reconstructions of rod phantom from noisy data at 5 cutoff frequencies. b) Profiles of the pASF and PRF in the z and x directions, respectively, of FBP reconstructions at 5 cutoff frequencies. Reference lines are shown at a value of 0.5. c) Noiseless FBP reconstructions of rods at 5 orientations and 4 cutoff frequencies. The display window is held constant over images within a column, but varies between columns. d) Scaled image RMSE $s(\phi)$ comparing scaled noiseless reconstructions to true signal. The quantity $s(\phi)$ is shown as a function of cutoff frequency for the 5 signal orientations shown in c).

5.4.1 Simulation Study

FBP - Figure 5.5 shows the simulation results for FBP. In panel a) we show reconstructions at five different cutoff frequencies in the presence of noise for visual assessment of orientation

dependence in signal conspicuity. A common trend of decreasing conspicuity with decreasing signal angle is observed for reconstructions with cutoff frequencies $\nu_c > 0.3$. Conspicuity appears to be approximately orientation independent in the $\nu_c = 0.3$ reconstruction, but further increasing regularization appears to reverse the trend in orientation dependence, favoring low-angle signals, as seen in the $\nu_c = 0.1$ reconstruction.

Panel b) shows the pASF and PRF at different cutoff frequencies. The full width at half maximum (FWHM) of the pASF doubles from 3.8 mm to 7.4 mm in going from a cutoff frequency of $\nu_c = 0.7$ to $\nu_c = 0.3$. The FWHM of the PRF almost triples over this range, going from 0.2 mm to 0.6 mm. Considering a cutoff frequency of 0.3 provided the closest to orientation independent conspicuity in noisy data reconstructions, removing orientation dependence via increasing Hanning window regularization is seen to come at a large cost to both x and z resolution.

In panel c) of Figure 5.5 we show the noiseless 2D signal profiles of FBP reconstructions at 4 different cutoff frequencies. The display window is constant over the images in a single column so that signal amplitude can be compared between orientations, but the display window differs between each column. As seen earlier in Figure 5.2, an orientation dependent cupping in signal amplitude can be seen at high cutoff frequencies, with the cupping becoming progressively more pronounced with decreasing signal angle. As cutoff frequency is decreased, the extent of cupping is reduced, being barely discernible in the $\nu_c = 0.3$ reconstructions; however, the signals at this cutoff frequency exhibit significant blur in the x-direction. Note the reconstruction at this same cutoff frequency exhibits approximately orientation independent conspicuity in panel a). At a cutoff frequency of $\nu_c = 0.1$, signal amplitude is seen to decrease with increasing signal angle, in line with the orientation dependence of conspicuity at this regularization strength in panel a).

One can also observe overshoot around the x-edges of signal profiles that increases in x-extent with decreasing filter width. This edge enhancement along the x-axis is characteristic of FBP reconstruction from projections acquired over a limited angular range. [89]

In panel d) we plot $s(\phi)$ as a function of cutoff frequency. The horizontal axis of the plot has been inverted to be consistent with similar plots for the other 3 algorithms, with regularization strength increasing to the right. A minimum orientation dependence in s(ϕ) of 1.7×10^{-3} is observed at a cutoff frequency of $\nu_c = 0.3$, the same cutoff at which the cupping in signal amplitude is seen to largely disappear from low angle signals in panel c) and conspicuity is seen to be largely orientation independent in panel a). The rank ordering of $s(\phi)$ at cutoff frequencies above $\nu_c = 0.3$ favors larger angles, tracking with the presence of cupping artifact in signal profiles. At lower cutoff frequencies the rank ordering reverses as excessive blurring in the x-direction results in $s(\phi)$ favoring signals with larger x-extent.

mFBP - The simulation results for mFBP are shown in Figure 5.6. Referring to panel a), the orientation dependence of conspicuity is seen to decrease with increasing δ values, but further reduction is difficult to discern at δ values above $\delta = 0.10$. Inspecting panel b), we see that the pASF at this value is comparable to FBP with a cutoff frequency of $\nu_c = 1.0$ near the plane containing the signal and $\nu_c = 0.7$ at larger distances. Referring back to panel a), the $\delta = 0.10$ reconstruction is seen to have reduced orientation dependence relative to the FBP $\nu_c = 0.7$ reconstruction.

The PRF curves in panel b) show the x resolution of the mFBP reconstructions, in terms of FWHM, is comparable to FBP reconstruction with a cutoff frequency of $\nu_c = 1.0$ at all regularization strengths; however, the negative side lobes of the point response function are reduced as regularization strength is increased, suggesting a reduction in x-edge enhancement at large regularization strengths.

Inspecting panel c), signal profiles are seen to become less orientation dependent with increasing regularization strength. Both orientation dependent cupping and x-direction overshoot are seen to decrease with increasing δ values.

Referring to panel d), the $s(\phi)$ for each orientation decreases with increasing values of δ, but the rank ordering of $s(\phi)$ reverses between values of $\delta = 0.025$ and $\delta = 0.05$. The reversal in rank ordering is largely attributable to the orientation dependence of the overshoot

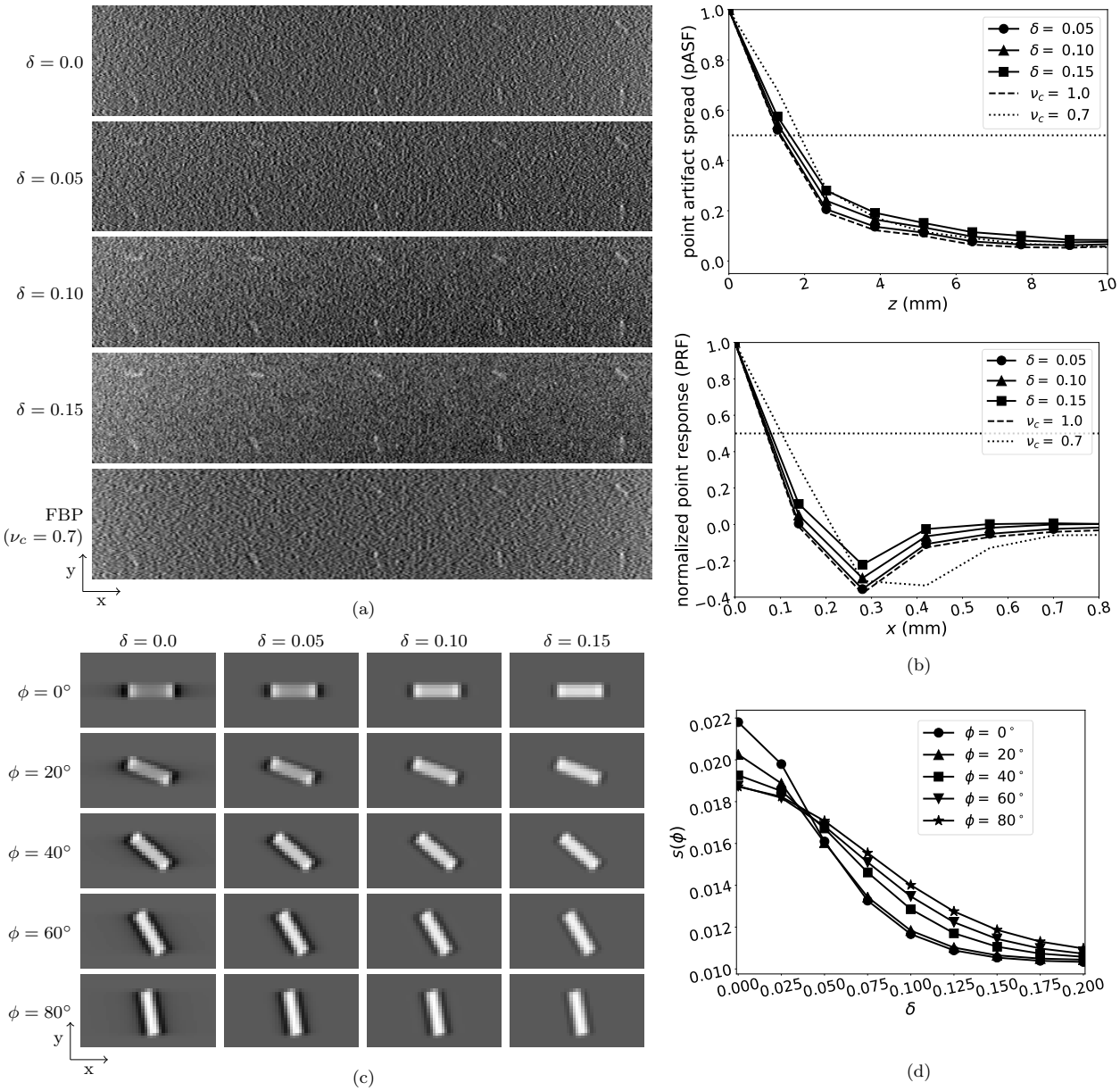

Figure 5.6: a) mFBP reconstructions of rod phantom from noisy data at 5 regularization strengths. b) Profiles of the pASF and PRF in the z and x directions, respectively, of mFBP reconstructions at varying regularization strengths. The corresponding curves for FBP with cutoff frequencies of $\nu_c = 1.0$ and $\nu_c = 0.7$ are shown for comparison. Reference lines are shown at a value of 0.5. c) Noiseless mFBP reconstructions of rods at 5 orientations and regularization strengths. The display window is held constant over images within a column, but varies between columns. d) Scaled image RMSE $s(\phi)$ comparing scaled noiseless reconstruction to true signal. The quantity $s(\phi)$ is shown as a function of cutoff frequency for the 5 signal orientations shown in c).

artifact. The high-angle signals have longer x-edges and therefore exhibit overshoot in more pixels, leading to a larger value of $s(\phi)$. As overshoot is further reduced at larger δ values the orientation dependence of $s(\phi)$ is seen to decrease.

For quantitative comparison of orientation dependence at matched resolution, variation in $s(\phi)$ over signal angle for mFBP at $\delta = 0.10$ is 2.4×10^{-3} while it is 3.6×10^{-3} for FBP at $\nu_c = 0.7$.

LSQI - The simulation results for LSQI are shown in Figure 5.7. Recall that the regularization strength for LSQI is specified on a log scale via the parameter $\gamma = \log_{10} \lambda$. Conspicuity of signals in the noisy reconstructions in panel a) shows a trend of increasing with signal angle at low regularization strengths, similar to the results with FBP at high cutoff frequencies. By contrast to FBP, the conspicuity becomes less orientation dependent with increasing regularization strength indefinitely, though it is difficult to discern further improvement beyond a regularization strength of approximately $\gamma = -0.5$. Recall the reconstruction limits to backprojection, up to scale, as $\gamma \to \infty$, so one would expect minimal orientation dependence in the limit of large γ.

In panel b) we see that the FWHM of the pASF is better or comparable to that of FBP with a cutoff frequency of $\nu_c = 1.0$ for all regularization strengths, even in the limit of infinite regularization (see the backprojection curve). At larger distances from the slice containing the true signal, though, the tail of the pASF becomes worse with increasing regularization strength, rising slightly above the tail of FBP at $\nu_c = 0.7$ in every LSQI curve. A regularization strength of $\gamma = -0.5$ appears to be comparable to FBP with a cutoff frequency of $\nu_c = 1.0$ in slices close to the signal and comparable to FBP with a cutoff frequency of $\nu_c = 0.7$ beyond approximately 6 mm away from the signal. A $\gamma = -0.5$ LSQI reconstruction is therefore seen to have matched, or slightly improved, z-resolution compared to a $\nu_c = 0.7$ FBP reconstruction; however, referring back to panel a), it appears the orientation dependence of conspicuity in the LSQI $\gamma = -0.5$ reconstruction is less than that in the FBP $\nu_c = 0.7$ reconstruction.

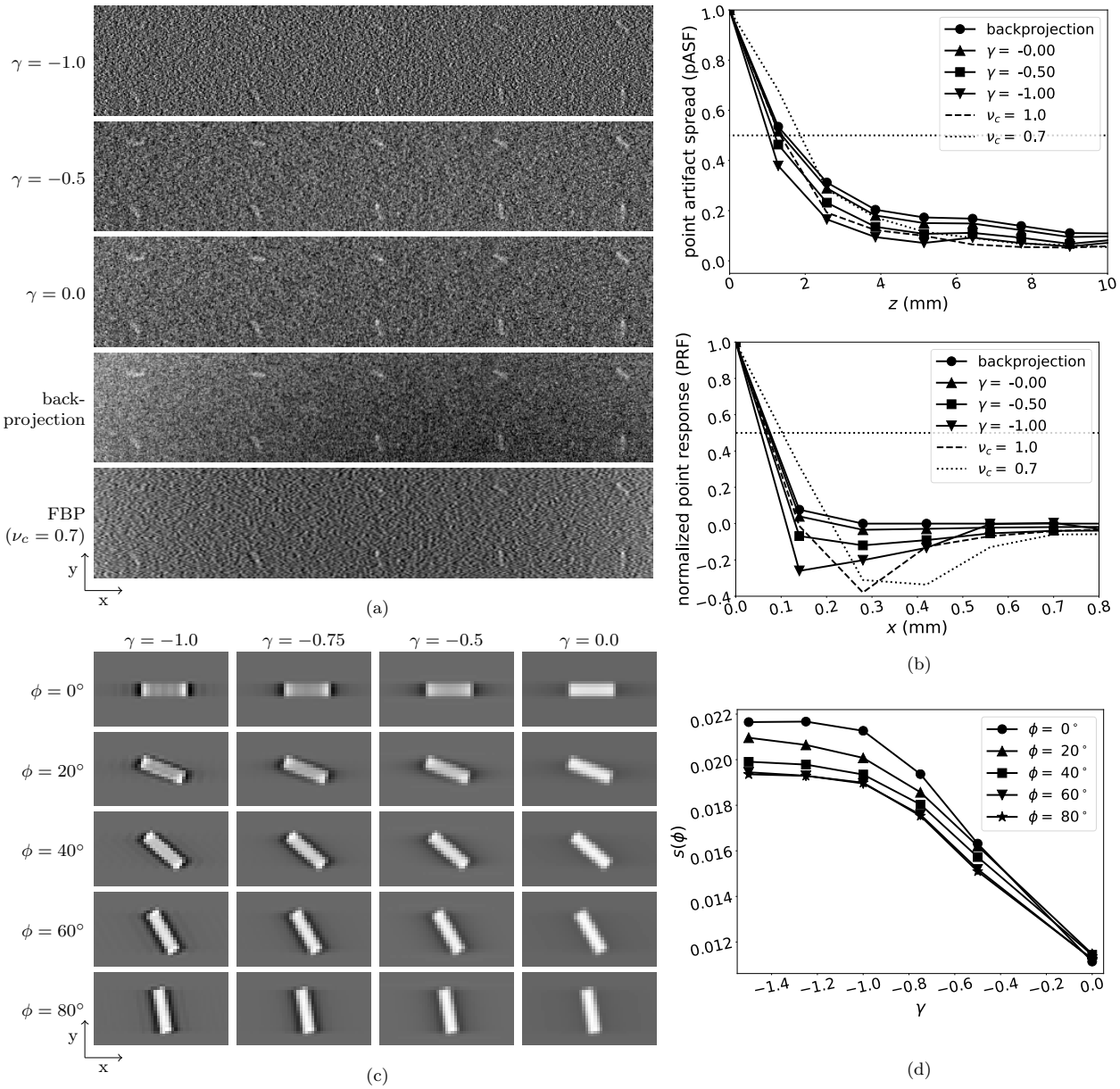

Figure 5.7: a) LSQI reconstructions of rod phantom from noisy data at 3 regularization strengths. Backprojection (infinite regularization) and FBP reconstructions are shown for reference. b) Profiles of the pASF and PRF in the z and x directions, respectively, of LSQI reconstructions at varying regularization strengths. The corresponding curves for FBP with cutoff frequencies of $\nu_c = 1.0$ and $\nu_c = 0.7$ are shown for comparison. Reference lines are shown at a value of 0.5. c) Noiseless LSQI reconstructions of rods at 5 orientations and 4 regularization strengths. Regularization strength is specified by $\gamma = \log_{10} \lambda$. d) Scaled image RMSE $s(\phi)$ comparing scaled noiseless reconstructions to true signal. The quantity $s(\phi)$ is shown as a function of regularization strength for the 5 signal orientations shown in c).

The PRF curves show the x resolution of the LSQI reconstructions, in terms of FWHM, is comparable to FBP reconstruction with a cutoff frequency of $\nu_c = 1.0$ at all regularization strengths; however, the negative side lobes of the point response function are reduced as regularization strength is increased, suggesting a reduction in x-edge enhancement at large regularization strengths.

The noiseless signal profiles of LSQI reconstruction are shown in panel c) of Figure 5.7. Signal profiles at the lowest two regularization strengths exhibit the same orientation dependent cupping in signal amplitude observed in the high cutoff frequency FBP reconstructions. The cupping again decreases with increasing regularization strength, but, unlike FBP, the orientation dependence appears to decrease indefinitely with increasing regularization, matching the trends in conspicuity observed in panel a). We also observe that overshoot around the x-edges of signals, while present at low regularization strengths, is progressively reduced with increasing regularization strength, in line with the reduction in magnitude of negative side-lobes in the PRF curves in panel b).

The rank ordering of the curves in panel d) is seen to favor high angle signals, similar to the behavior observed in the high-cutoff frequency regime of the FBP $s(\phi)$ curves. As regularization strength is increased, both $s(\phi)$ for each signal orientation and the orientation dependence of $s(\phi)$ decrease. Unlike the mFBP curves, there is no reversal in the rank ordering as regularization strength is increased. This results from differences in the overshoot artifact between the two algorithms. Comparing the $\delta = 0.10$ PRF of mFBP in Figure 5.6 to that of LSQI with $\gamma = -0.5$, we see that the overshoot in the mFBP point response has more than double the magnitude though signal profiles indicate that the cupping artifact has largely been eliminated in both reconstructions. It is the overshoot that causes a reversal in rank ordering in mFBP, and since it is of lower magnitude in the LSQI reconstructions, the rank ordering continues to favor high-angle signals at high regularization strengths.

For quantitative comparison of orientation dependence in FBP and LSQI at matched z-resolution, the range in $s(\phi)$ over signal orientation for FBP with $\nu_c = 0.7$ is 3.6×10^{-3}

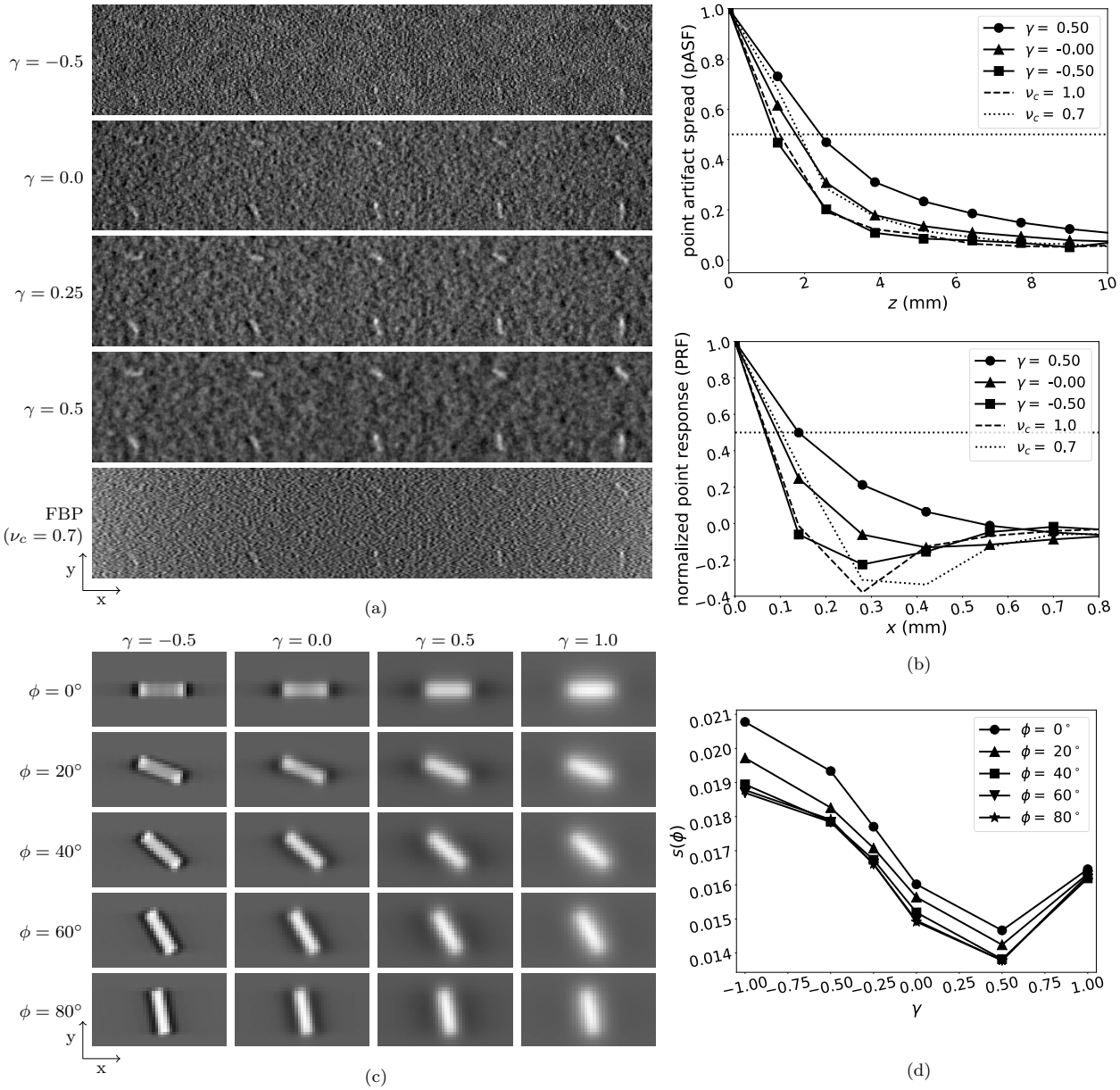

Figure 5.8: a) LSQD reconstructions of rod phantom from noisy data at 4 regularization strengths. FBP reconstruction with $\nu_c = 0.7$ is shown for reference. b) Profiles of the pASF and PRF in the z and x directions, respectively, of LSQD reconstructions at varying regularization strengths. The corresponding curves for FBP with cutoff frequencies of $\nu_c = 1.0$ and $\nu_c = 0.7$ are shown for comparison. Reference lines are shown at a value of 0.5. c) Noiseless LSQD reconstructions of rods at 5 orientations and 4 regularization strengths. d) Scaled image RMSE $s(\phi)$ comparing scaled noiseless reconstructions to true signal. The quantity $s(\phi)$ is shown as a function of regularization strength for the 5 signal orientations shown in c).

whereas for LSQI at $\gamma = -0.50$ it is 1.2×10^{-3}.

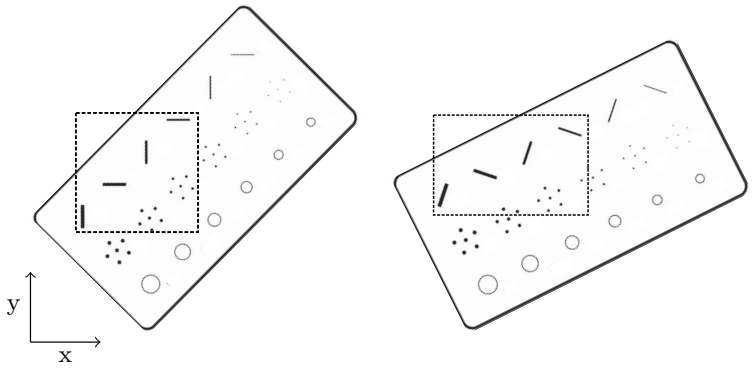

Figure 5.9: Diagram illustrating the two orientations of the ACR digital mammography phantom employed in the physical phantom study. In the left panel, the fibers are oriented at approximately 0° and 90° with respect to the x-axis. In the right they are oriented at approximately 20° and 70°.

LSQD - Simulation results for LSQD are shown in Figure 5.8. Trends in signal conspicuity seen in panel a) are largely the same as the trends observed with LSQI. Inspecting panel b), we see that a $\gamma = 0.0$ LSQD reconstruction has comparable z and x resolution to an FBP reconstruction with cutoff frequency $\nu_c = 0.7$. In the corresponding reconstructions in panel a) signal conspicuity appears to be less orientation dependent in the LSQD reconstruction.

The LSQD signal profiles in panel c) of Figure 5.8 follow similar trends to those observed with LSQI. In particular, the orientation dependent cupping phenomenon is again observed at low regularization strengths and is reduced with increasing regularization. Additionally, overshoot in the x direction is reduced at high regularization strengths. By contrast to LSQI, the in-plane signal profile exhibits significant blurring in both the x and y directions at the highest regularization strength. These visual trends track well with the $s(\phi)$ curves in panel d), which exhibit decreasing orientation dependence with increasing regularization strength but an increase in $s(\phi)$ beyond a regularization strength of $\gamma = 0.5$ attributable to the increased blurring.

The range of $s(\phi)$ over signal orientation for LSQD at this regularization strength is 1.1×10^{-3} compared to 3.6×10^{-3} for FBP, demonstrating reduced orientation dependence in LSQD relative to FBP at matched z-resolution.

5.4.2 Physical Phantom Study

In the simulation studies we observed matched z resolution between FBP, mFBP, LSQI, and LSQD, at regularization strengths of $\nu_c = 0.7$, $\delta = 0.1$, $\gamma = -0.5$, and $\gamma = 0.0$, respectively. We also observed a decrease in orientation dependence for mFBP, LSQI, and LSQD relative to FBP both visually, in reconstructions from noisy data, and quantitatively, in $s(\phi)$. Here we reconstruct ACR digital mammography accreditation phantom data at these regularization strengths to corroborate this result with real data. We also include reconstructions at one lower and one higher regularization strength to verify the trends observed in simulation.

Reconstructions with FBP, mFBP, LSQI, and LSQD are shown in Figure 5.10. For reconstructions in the top row of each panel, the phantom was oriented so the rods lay approximately 0° and 90° off the source-axis plane, while for reconstructions in the bottom row, the rods were oriented at approximately 20° and 70°. In both rows, the rod of largest diameter occupies the bottom left corner and rod diameter decreases going up and to the right. Refer to Figure 5.9 for a diagram of the ACR digital mammography phantom insert along with ROIs used for visualization at each orientation. The regularization parameter employed in reconstruction is shown in each image, where we have again used the simplifying notation $\gamma = \log_{10} \lambda$ for LSQI and LSQD. Regularization strength increases going from the top panel to the bottom.

The results are largely in line with what was observed in simulation. Each of the four algorithms exhibits significant orientation dependence at the lowest regularization strength (top panel), with the second thickest rod often being invisible when oriented at 0° despite the third thickest rod, oriented at 90° being conspicuous in the same reconstruction. Conspicuity is seen to be largely in line with signal thickness in both orientations for LSQI and mFBP in the middle panel, while the FBP reconstruction of comparable resolution exhibits significant orientation dependence. The LSQD reconstruction in the middle panel exhibits orientation dependence, but to a lesser extent than FBP.

It is difficult to discern any improvement to orientation dependence of conspicuity in the

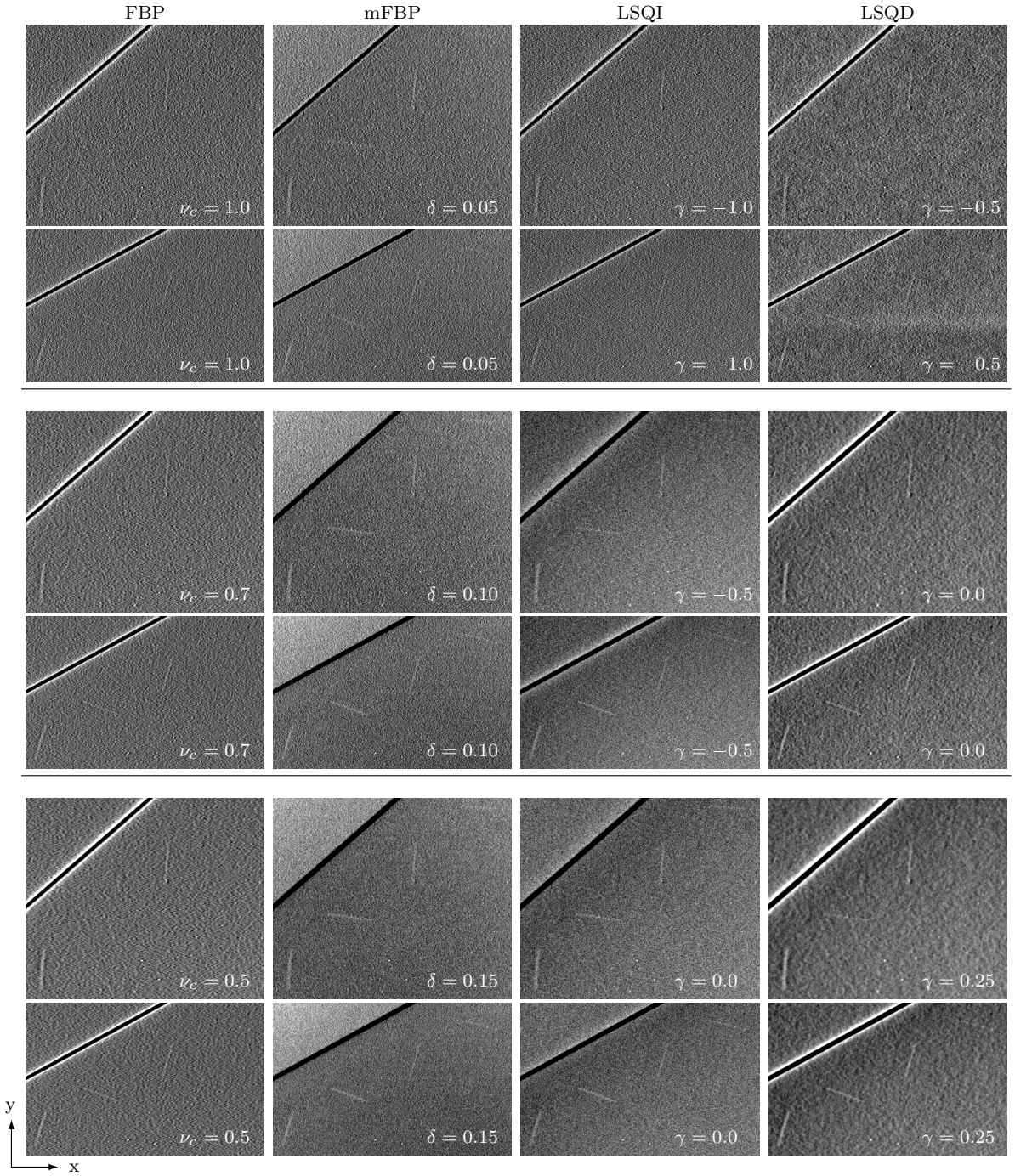

Figure 5.10: FBP, mFBP, LSQI, and LSQD reconstructions of the ACR phantom at two orientations. The phantom is oriented so the rods are approximately rotated 0° (horizontal) and 90° (vertical) or 20° and 70° from the x-axis. The thickest rod lies in the bottom left corner of each ROI while the thinnest lies in the upper right corner. Regularization strength increases going from the top to bottom panel. Reconstructions in the middle panel have comparable resolution as evaluated by the pASF and PRF in simulation.

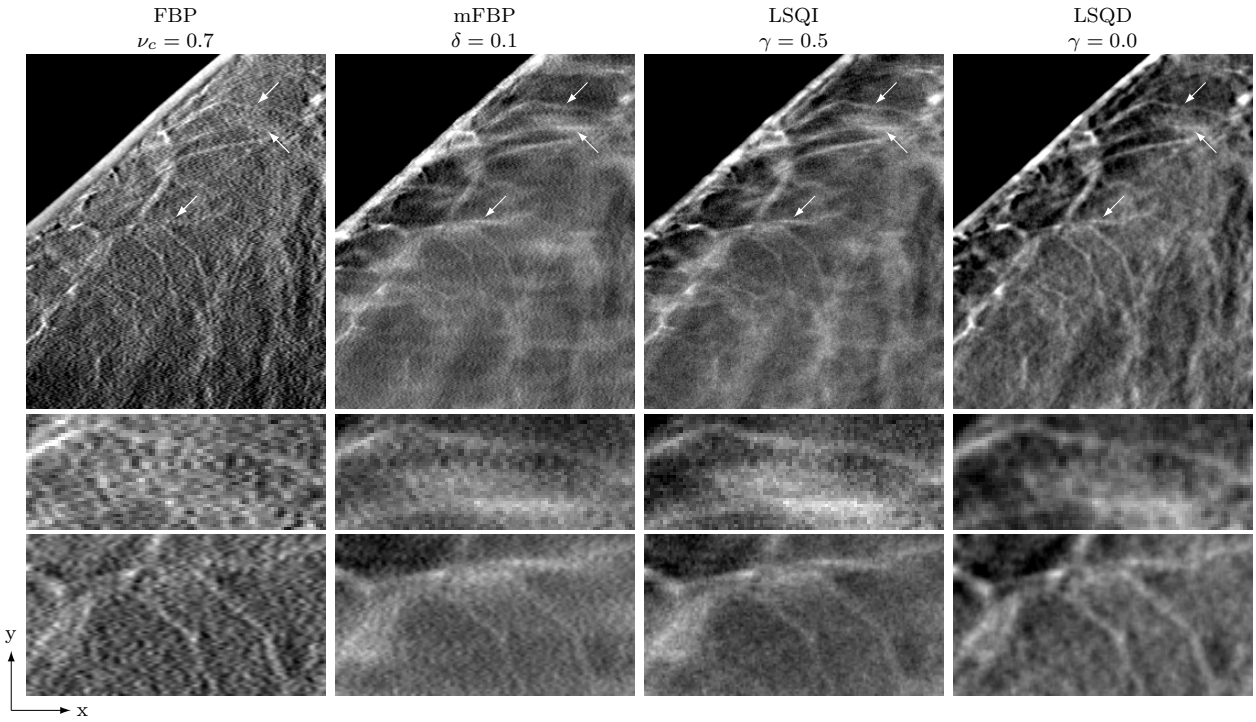

Figure 5.11: Top row: In-plane slice of FBP, mFBP, LSQI, and LSQD reconstructions of a breast. Reconstructions have matched resolution as evaluated by the pASF and PRF in simulation. Arrows point to low angle structures which appear more conspicuous in the mFBP, LSQI, and LSQD reconstructions relative to FBP. Middle row: ROI containing structures pointed to by two top right arrows in the top row. Bottom row: ROI containing structure pointed to by the bottom left arrow in the top row.

LSQI and mFBP reconstructions in the bottom panel, while the orientation dependence of LSQD and FBP have clearly improved. Note that FBP at this cutoff frequency has the worst z and x resolution, as measured by pASF and PRF, of any of the reconstructions in the panel.

5.4.3 Breast Data Study

In the final study, using the regularization strengths determined from simulation to have matched resolution between algorithms, but reduced orientation dependence for LSQI, LSQD, and mFBP, we reconstruct breast data to investigate orientation dependence in the presence of realistic background structure. For reference, the same regularization strengths employed in these reconstructions were used to generate the images in the middle panel of Figure 5.10.

An ROI from breast data reconstructed using each of the four algorithms is shown in Figure 5.11. Two smaller ROI are also shown containing structures nearly oriented in the x and y directions. Three structures oriented close to the x direction are pointed to by arrows in the top row.

In the second row of images, we see “breakage" in a low-angle structure in the FBP reconstruction while it appears contiguous in the LSQI, LSQD, and mFBP reconstructions. We also see a horizontal structure in the bottom right corner of the ROI in the mFBP, LSQI, and LSQD reconstructions that does not appear to be present in the FBP reconstruction. In the bottom row of images, we see a structure aligned with the x-axis more conspicuously in the LSQI, LSQD, and mFBP images than in the FBP image. Meanwhile, two structures aligned more closely with the y-axis are visible in all four reconstructions, though they appear more conspicuously in the FBP reconstruction.

5.5 Discussion

The main trend observed in all four reconstruction algorithms is that an orientation dependent cupping artifact is observed at low regularization strengths, in which signals lying close to parallel to the x-axis are more affected than their orthogonal counterparts. As regularization strength is increased, the cupping artifact is reduced, though different forms of regularization yield significantly different tradeoffs with respect to reducing orientation dependence while maintaining resolution. We found that using LSQI, LSQD, and mFBP we can maintain resolution comparable to an FBP reconstruction with a Hanning window cutoff frequency of $\nu_c = 0.7$ while reducing orientation dependence significantly.

While LSQI, LSQD, and mFBP were all seen to have a better tradeoff than FBP with respect to reducing orientation dependence while maintaining resolution, LSQD appeared to have a slightly worse tradeoff than LSQI and mFBP. We saw from the simulation studies that LSQD with a regularization strength of $\gamma = 0.0$ was comparable in resolution to FBP with a cutoff frequency of $\nu_c = 0.7$. Inspecting the middle panel of Figure 5.10, conspicuity of

LSQD at this regularization still shows some orientation dependence, while comparable resolution LSQI and mFBP reconstructions, shown in the same panel, do not; however, different forms of derivative regularization may lead to different results. For example, in our implementation, the matrix D approximated the gradient operator, and therefore weighted each dimension via division by the appropriate voxel dimension. Altering this weighting scheme by, for instance, using isotropic weighting, could impact the tradeoff between resolution and orientation dependence.

Increasing regularization in mFBP, LSQI, and LSQD was seen to reduce overshoot in the x-profiles of the point response function. While this may initially seem advantageous, as it reduces the extent of overshoot artifacts surrounding high-contrast artifacts, this overshoot in the point response is also responsible for edge enhancement along the x direction in traditional FBP tomosynthesis reconstructions. This could potentially cause a reduction in conspicuity for fiber-like structures oriented parallel to the y-axis. Referring back to Figure 5.11, this effect may be responsible for the increased conspicuity in FBP of the two near-vertical structures in the bottom right quadrant of the bottom row of ROIs. We caution, however, that other factors, such as noise texture, could be responsible for this increased conspicuity. To emphasize this point, recall from the simulation studies that the magnitude of overshoot in mFBP at a regularization strength of $\delta = 0.1$ was double that of LSQI at $\gamma = -0.5$; however, conspicuity of the two y-oriented structures in Figure 5.11 does not appear to be clearly improved in mFBP as compared to LSQI.

5.6 Conclusions

We have investigated the interplay between orientation and parameter dependence of signal conspicuity in DBT for four reconstruction algorithms. We employed simulation studies to characterize how signal profiles varied with regularization in the four reconstruction frameworks and investigated the impact of these variations on signal conspicuity in the presence of noise. We additionally studied the resolution of reconstructed images as a function of

regularization strength to determine whether orientation dependence could be reduced relative to FBP with Hanning window apodization while maintaining similar resolution. We then used physical phantom and breast data to gauge the potential impact of orientation dependence in real data reconstructions.

The results demonstrated a common trend among all four algorithms of signals oriented parallel to the x-axis being less conspicuous than perpendicular signals at low regularization strengths. LSQI, LSQD, and mFBP all showed favorable tradeoffs between resolution and orientation dependence as compared to FBP with Hanning window apodization, though we also observed that reduction in orientation dependence came at a cost of reduced edge enhancement in reconstructions.

Future work will focus on investigating the interplay between regularization strength and orientation dependence for non-linear reconstruction algorithms, particularly those employing different forms of edge-preserving regularization. Contrast-to-noise ratio in non-linear reconstruction is dependent on signal contrast, so orientation dependence may exhibit dependence on signal amplitude for such algorithms.

CHAPTER 6

SUMMARY AND CONCLUSIONS

In this thesis, extensive characterization studies have been performed to characterize parameter trends for IIR algorithms in breast CT and DBT, and, in the process, a number of objective image quality metrics that can be of use in guiding reconstruction algorithm development have been employed. With these studies a number of important trends have been uncovered relating to the selection of parameters for IIR in breast CT and DBT. Here, the findings from each chapter are summarized.

In Chapter 2, a detailed investigation of discrete-to-discrete forward models in IIR for CT was performed, focusing in particular on the converged solutions to the underlying optimization problems motivating IIR. The conditioning of four common discrete-to-discrete CT forward models was seen to exhibit extreme sensitivity to pixel size, deteriorating quite rapidly when the number of image pixels approaches the number detector elements. Using larger pixel sizes, conditioning issues could be avoided entirely, but it was seen that further improvement to RMSE could be achieved employing smaller pixel sizes and appropriate levels of regularization. However, sensitivity of image RMSE to regularization strength increased with decreasing pixel size. It was also seen that by employing alternative expansion sets, namely the natural pixel and Gaussian blur formulations, that image RMSE could be further reduced. Lastly, we saw that in the case of noisy data, while the level of regularization required to minimize image RMSE increased, smaller pixel sizes remained favorable.

Next, in Chapter 3, our focus was extended from the converged solutions of reconstruction optimization problems to the case of early truncation of a sparsity-exploiting IIR algorithm. Incremental algorithms, which have been empirically observed to exhibit fast initial convergence, were applied to the task of image reconstruction based on a TV-constrained data-discrepancy minimization reconstruction optimization problem in a sparse-view system geometry. An investigation was performed to determine whether statistical design considerations motivating the data-discrepancy term led to significant differences in the statistics of

reconstructed images at early iteration. The results indicated that the design considerations of the corresponding optimization problems could be observed at as low as 50 iterations. In addition, with appropriate parameter selection, reconstructed images were seen to be free of streak artifacts typical of reconstructions from sparse-view geometries.

In Chapter 4, the focus was shifted to DBT, and an investigation of simulation-based metrics for characterizing image reconstruction algorithms in DBT was performed. Three simulation-based image quality metrics for use in parameter selection for linear IIR were investigated. In the process, an RMSE-based metric was adapted to DBT along with a task-based metric for assessing linear IIR. The proposed gradient image RMSE metric appeared to rectify the short-comings of the image RMSE, in particular, removing its sensitivity to mean pixel value. It was also seen that the ROI-HO efficiency demonstrated a signal-dependent saturating behavior with increasing regularization strength for both SKE/BKE and SKE/BKS tasks and both algorithms considered. These trends in ROI-HO efficiency tracked well with conspicuity of signals in real data reconstructions of the ACR phantom for both the SKE/BKE and SKE/BKS tasks.

Lastly, in Chapter 5, a study was performed to investigate how reconstruction algorithm design, for both IIR and analytic algorithms, could be used to mitigate the orientation dependence of fiber-like signals in DBT. Simulation-based metrics were employed to characterize how signal profiles varied with regularization strength using four reconstruction algorithms. Physical phantom and breast data was then used to gauge the potential impact of orientation dependence in real data reconstructions. In all four reconstruction algorithms considered, a tradeoff was observed between reducing orientation dependence and maintaining depth resolution that was dictated by regularization strength. This tradeoff was seen to be more favorable in the two IIR algorithms investigated than in FBP with Hanning window apodization. A modified regularization strategy in FBP was investigated and led to a tradeoff comparable to what was seen with the iterative algorithms.

To summarize, in this thesis, using objective image quality metrics, extensive character-

ization of important parameter trends has been performed for IIR algorithm design in both breast CT and DBT. To simplify the analysis, the primary focus was on the characterization of parameter trends for IIR algorithms that do not incorporate sparsity-exploiting regularization strategies; however, the trends uncovered in this work should be of use for guiding the design of sparsity-exploiting IIR algorithms for breast CT and DBT. The work on breast CT is directly applicable to the design of IIR algorithms, with or without sparsity exploiting regularization, with regards to guiding the selection of voxel size, regularization strength, and iteration number. The work on DBT both provides simulation-based methodologies for informing parameter selection and demonstrates important object-dependent parameter trends that need be considered when designing both IIR and analytic algorithms.

REFERENCES

[1] Bian, J., Yang, K., Boone, J. M., Han, X., Sidky, E. Y., and Pan, X., "Investigation of iterative image reconstruction in low-dose breast CT," *Phys. Med. Biol.* **59**, 2659–2685 (2014).

[2] Sidky, E. Y., Pan, X., Reiser, I. S., Nishikawa, R. M., Moore, R. H., and Kopans, D. B., "Enhanced imaging of microcalcifications in digital breast tomosynthesis through improved image-reconstruction algorithms," *Med. Phys.* **36**(11), 4920–4932 (2009).

[3] Boone, J. M., Nelson, T. R., Lindfors, K. K., and Seibert, J. A., "Dedicated Breast CT : Radiation Dose and Image Quality Evaluation," *Radiology* **221**, 657–667 (2001).

[4] O'Connell, A. M., Karellas, A., and Vedantham, S., "The Potential Role of Dedicated 3D Breast CT as a Diagnostic Tool: Review and Early Clinical Examples," *Breast J.* **20**, 592–605 (2014).

[5] Natterer, F., [*The Mathematics of Computerized Tomography*], SIAM (2001).

[6] Kak, A. C. and Slaney, M., [*Principles of Computerized Tomographic Imaging*], IEEE Press, Piscataway, NJ (1988).

[7] Deans, S. R., [*The Radon Transform and Some of its Applications*], Courier Corporation (2007).

[8] Lewitt, R. M., "Alternatives to voxels for image representation in iterative reconstruction algorithms.," *Phys. Med. Biol.* **37**(3), 705–16 (1992).

[9] Miller, E. R., McCurry, E. M., and Hruska, B., "An infinite number of laminograms from a finite number of radiographs," *Radiology* **98**, 249–255 (1971).

[10] Niklason, L. T., Christian, B. T., Niklason, L. E., Kopans, D. B., Castleberry, D. E., Opsahl-Ong, B. H., Landberg, C. E., Slanetz, P. J., Giardino, A. A., Moore, R., Albagli, D., Dejule, M. C., Fitzgerald, P. F., Fobare, D. F., Giambattista, B. W., Kwasnick, R. F., Liu, J., Lubowski, S. J., Possin, G. E., Richotte, J. F., Wei, C.-Y., and Wirth, R. F., "Digital Tomosynthesis in Breast Imaging," *Radiology* **205**, 399–406 (1997).

[11] Poplack, S. P., Tosteson, T. D., Kogel, C. A., and Nagy, H. M., "Digital Breast Tomosynthesis: Initial Experience in 98 Women," *Am. J. Roentgenol.* **189**(September), 616–623 (2007).

[12] Good, W. F., Abrams, G. S., Catullo, V. J., Chough, D. M., Ganott, M. A., Hakim, C. M., and Gur, D., "Digital Breast Tomosynthesis: A Pilot Observer Study," *Am. J. Roentgenol.* **190**(April), 865–869 (2008).

[13] Rafferty, E. A., "Digital Mammography: Novel Applications," *Radiol. Clin. North Am.* **45**, 831–843 (2007).

[14] Svahn, T., Andersson, I., Chakraborty, D., Svensson, S., Ikeda, D., Fornvik, D., Mattson, S., Tingberg, A., and Zackrisson, S., "The Diagonstic Accuracy of Dual-View Digital Mammography, Single-View Breast Tomosynthesis and a Dual-View Combination of Breast Tomosynthesis and Digital Mammography in a Free-Response Observer Performance Study," *Radiat. Prot. Dosimetry* **139**, 113–117 (2010).

[15] Rose, S. L., Tidwell, A. L., Bujnoch, L. J., Kushwaha, A. C., Nordmann, A. S., and Sexton Jr., R., "Implementation of Breast Tomosynthesis in a Routine Screening Practice: An Observational Study," *Am. J. Roentgenol.* **200**(June), 1401–1408 (2013).

[16] Wu, T., Moore, R. H., Rafferty, E. A., and Kopans, D. B., "A comparison of reconstruction algorithms for breast tomosynthesis.," *Med. Phys.* **31**(9), 2636–2647 (2004).

[17] Zhou, J., Zhao, B., and Zhao, W., "A computer simulation platform for the optimization of a breast tomosynthesis system," *Med. Phys.* **34**(3), 1098–1109 (2007).

[18] Sidky, E. Y., "Breast tomosynthesis: Update on image acquisition and reconstruction techniques," Presented at the 2012 meeting of the Radiological Society of North America.

[19] Sechopoulos, I., "A review of breast tomosynthesis. Part II. Image reconstruction, processing and analysis, and advanced applications," *Med. Phys.* **40**(37), 14302 (2013).

[20] Orman, J., Mertelmeier, T., and Haere, W., "Adaptation of image quality using various filter setups in the filtered backprojection approach for digital breast tomosynthesis," in [*Proc. 8th Int. Work. Digit. Mammogr.*], 175–182 (2006).

[21] Sidky, E. Y. and Pan, X., "Image reconstruction in circular cone-beam computed tomography by constrained, total-variation minimization.," *Phys. Med. Biol.* **53**(17), 4777–4807 (2008).

[22] Chen, G.-H., Tang, J., and Leng, S., "Priorimage constrained compressed sensing (PICCS): A method to accurately reconstruct dynamic CT images from highly undersampled projection data sets," *Med. Phys.* **35**(2), 660–663 (2008).

[23] Tian, Z., Jia, X., Yuan, K., Pan, T., and Jiang, S. B., "Low-dose CT reconstruction via edge-preserving total variation regularization.," *Phys. Med. Biol.* **56**(18), 5949–67 (2011).

[24] Xia, D., Xiao, X., Bian, J., Han, X., Sidky, E. Y., Carlo, F. D., and Pan, X., "Image reconstruction from sparse data in synchrotron-radiation-based microtomography," *Rev. Sci. Instrum.* **82**, 1–9 (2011).

[25] Liu, Y., Ma, J., Fan, Y., and Liang, Z., "Adaptive-weighted total variation minimization for sparse data toward low-dose x-ray computed tomography image reconstruction Adaptive-weighted total variation minimization for sparse data toward low-dose x-ray computed tomography image reconstruction," *Phys. Med. Biol.* **57**, 7923–7956 (2012).

[26] Han, X., Bian, J., Ritman, E. L., Sidky, E. Y., and Pan, X., "Optimization-based reconstruction of sparse images from few-view projections," *Phys. Med. Biol.* **57**, 5245–5273 (2012).

[27] Jørgensen, J. S., Sidky, E. Y., and Pan, X., "Quantifying admissible undersampling for sparsity-exploiting iterative image reconstruction in X-Ray CT," *IEEE Trans. Med. Imaging* **32**(2), 460–473 (2013).

[28] Niu, S., Gao, Y., Bian, Z., Huang, J., Chen, W., Yu, G., Liang, Z., and Ma, J., "Sparse-view x-ray CT reconstruction via total generalized variation regularization.," *Phys. Med. Biol.* **59**(12), 2997–3017 (2014).

[29] Man, B. D., Member, S., Nuyts, J., Marcha, G., and Suetens, P., "Reduction of metal streak artifacts in x-ray computed tomography using a transmission maximum a posteriori algorithm," *IEEE Trans. Nucl. Sci.* **41**(3), 977–981 (2000).

[30] Elbakri, I. A. and Fessler, J. A., "Statistical image reconstruction for polyenergetic X-ray computed tomography," *IEEE Trans. Med. Imaging* **21**(2), 89–99 (2002).

[31] Lasio, G. M., Whiting, B. R., and Williamson, J. F., "Statistical reconstruction for x-ray computed tomography using energy-integrating detectors.," *Phys. Med. Biol.* **52**(8), 2247–2266 (2007).

[32] Barrett, H. H. and Myers, K. J., [*Foundations of Image Science*], John Wiley & Sons, Hoboken, New Jersey (2004).

[33] Matej, S., Lewitt, R. M., and Member, S., "Practical Considerations for 3-D construction Using Spherical Symmetric Volume Elements," *IEEE Trans. Med. Imaging* **15**(1), 68–78 (1996).

[34] Ziegler, A., Köhler, T., Nielsen, T., and Proksa, R., "Efficient projection and backprojection scheme for spherically symmetric basis functions in divergent beam geometry," *Med. Phys.* **33**(12), 4653–4663 (2006).

[35] Snyder, D. L. and Miller, M. I., "The use of sieves to stabilize images produced with the EM algorithm for emission tomography," *IEEE Trans. Nucl. Sci.* **32**(5), 3864–3872 (1985).

[36] Buonocore, M. H., Brody, W. R., and Macovski, A., "A natural pixel decomposition for two dimensional image reconstruction," *IEEE Trans Biomed Eng* **BME-28**(2), 69–78 (1981).

[37] Hsieh, Y. L., Gullberg, G. T., Zeng, G. L., and Huesinan, R. H., "Image reconstruction using a generalized natural pixel basis," *IEEE Trans. Nucl. Sci.* **43**(4 PART 1), 2306–2319 (1996).

[38] Zbijewski, W. and Beekman, F. J., "Characterization and suppression of edge and aliasing artefacts in iterative x-ray CT reconstruction," *Phys. Med. Biol.* **49**(1), 145–157 (2004).

[39] Pan, X., Sidky, E. Y., and Vannier, M., "Why do commercial CT scanners still employ traditional, filtered back-projection for image reconstruction?," *Inverse Probl.* **25**(12), 1230009 (2009).

[40] Herman, G. T. and Davidi, R., "On Image Reconstruction from a Small Number of Projections.," *Inverse Probl.* **24**(4), 45011–45028 (2008).

[41] Nuyts, J., De Man, B., Fessler, J. A., Zbijewski, W., and Beekman, F. J., "Modelling the physics in the iterative reconstruction for transmission computed tomography.," *Phys. Med. Biol.* **58**(12), R63–96 (2013).

[42] Johns, P. C. and Yaffe, M. J., "X-ray characterisation of normal and neoplastic breast tissues," *Phys Med Biol* **32**, 675–95 (1987).

[43] Siddon, R. L., "Fast calculation of the exact radiological path for a three-dimensional CT array," *Med. Phys.* **12**, 252–255 (1985).

[44] Björck, Å., [*Numerical methods for least squares problems*], Society for Industrial and Applied Mathematics, Philadelphia (1996).

[45] De Man, B. and Basu, S., "Distance-driven projection and backprojection in three dimensions.," *Phys. Med. Biol.* **49**(11), 2463–2475 (2004).

[46] Golub, G. H. and Loan, C. F. V., [*Matrix Computations*], vol. 3rd, Johns Hopkins University Press, Baltimore and London, 3rd ed. (1996).

[47] Joseph, P. M., "An improved algorithm for reprojecting rays through pixel images," *IEEE Trans Med Imaging* **1**, 192–6 (1982).

[48] Wolf, P. A., Jørgensen, J. S., Schmidt, T. G., and Sidky, E. Y., "Few-view single photon emission computed tomography (SPECT) reconstruction based on a blurred piecewise constant object model.," *Phys. Med. Biol.* **58**(16), 5629–52 (2013).

[49] Gordon, R., Bender, R., and Herman, G. T., "Algebraic Reconstruction Techniques (ART) for Three-dimensional Electron Microscopy and X-ray Photography," *J. Theor. Biol.* **29**, 471–481 (1970).

[50] Qi, J. and Leahy, R. M., "Iterative reconstruction techniques in emission computed tomography," *Phys. Med. Biol.* **51**, R541–R578 (2006).

[51] Sidky, E. Y., Duchin, Y., Pan, X., and Ullberg, C., "A constrained, total-variation minimization algorithm for low-intensity x-ray CT," *Med. Phys.* **38**(S1), S117 (2011).

[52] Bertsekas, D. P., "Incremental proximal methods for large scale convex optimization," *Math. Program.* **129**(2), 163–195 (2011).

[53] Andersen, M. S. and Hansen, P. C., "Generalized row-action methods for tomographic imaging," *Numer. Algorithms* **67**(1), 121–144 (2014).

[54] Ahn, S., Fessler, J. A., Blatt, D., Member, S., and Hero, A. O., "Convergent Incremental Optimization Transfer Algorithms: Application to Tomography," *IEEE Trans. Med. Imaging* **25**(3), 283–296 (2006).

[55] Chambolle, A. and Pock, T., "A first-order primal-dual algorithm for convex problems with applications to imaging," *J. Math. Imaging Vis.* **40**(1), 120–145 (2011).

[56] Sidky, E. Y., Jørgensen, J. H., and Pan, X., "Convex optimization problem prototyping for image reconstruction in computed tomography with the Chambolle-Pock algorithm.," *Phys. Med. Biol.* **57**(10), 3065–91 (2012).

[57] Køhler, T. and Proksa, R., "Noise properties of maximum likelihood reconstruction with edge-preserving regularization in transmission tomography," in [*Proceedings of the 10th International Meeting on Three-Dimensional Image Reconstruction in Radiology and Nuclear Medicine*], 263–266 (2011).

[58] Bertsekas, D. P., Nedić, A., and Ozdaglar, A. E., [*Convex Analysis and Optimization*], Athena Scientific (2003).

[59] Hu, Y.-H., Zhao, B., and Zhao, W., "Image artifacts in digital breast tomosynthesis: Investigation of the effects of system geometry and reconstruction parameters using a linear system approach.," *Med. Phys.* **35**(2008), 5242–5252 (2008).

[60] Sechopoulos, I. and Ghetti, C., "Optimization of the acquisition geometry in digital tomosynthesis of the breast.," *Med. Phys.* **36**(4), 1199–1207 (2009).

[61] Saunders, R. S., Samei, E., Lo, J. Y., and Baker, J. A., "Can compression be reduced for breast tomosynthesis? Monte carlo study on mass and microcalcification conspicuity in tomosynthesis.," *Radiology* **251**(3), 673–682 (2009).

[62] Van de Sompel, D., Brady, S. M., and Boone, J., "Task-based performance analysis of FBP, SART and ML for digital breast tomosynthesis using signal CNR and Channelised Hotelling Observers," *Med. Image Anal.* **15**(1), 53–70 (2011).

[63] Park, S., Jennings, R., Liu, H., Badano, A., and Myers, K., "A statistical, task-based evaluation method for three-dimensional x-ray breast imaging systems using variable-background phantoms.," *Med. Phys.* **37**, 6253–6270 (2010).

[64] Zeng, R., Park, S., Bakic, P., and Myers, K. J., "Evaluating the sensitivity of the optimization of acquisition geometry to the choice of reconstruction algorithm in digital breast tomosynthesis through a simulation study.," *Phys. Med. Biol.* **60**(3), 1259–88 (2015).

[65] Reiser, I. and Nishikawa, R. M., "Task-based assessment of breast tomosynthesis: Effect of acquisition parameters and quantum noise.," *Med. Phys.* **37**(4), 1591–600 (2010).

[66] Sánchez, A. A., Sidky, E. Y., and Pan, X., "Use of the Hotelling observer to optimize image reconstruction in digital breast tomosynthesis," *J. Med. Imaging* **3**(1), 011008 (2015).

[67] Richard, S. and Samei, E., "Quantitative imaging in breast tomosynthesis and CT: Comparison of detection and estimation task performance.," *Med. Phys.* **37**(2010), 2627–2637 (2010).

[68] Gang, G. J., Lee, J., Stayman, J. W., Tward, D. J., Zbijewski, W., Prince, J. L., and Siewerdsen, J. H., "Analysis of Fourier-domain task-based detectability index in tomosynthesis and cone-beam CT in relation to human observer performance.," *Med. Phys.* **38**(4), 1754–1768 (2011).

[69] Young, S., Bakic, P. R., Myers, K. J., Jennings, R. J., and Park, S., "A virtual trial framework for quantifying the detectability of masses in breast tomosynthesis projection data.," *Med. Phys.* **40**(5), 051914 (2013).

[70] Sanchez, A. A., Sidky, E. Y., Reiser, I., and Pan, X., "Comparison of human and Hotelling observer performance for a fan-beam CT signal detection task," *Med. Phys.* **40**(3), 031104 (2013).

[71] Sanchez, A. A., Sidky, E. Y., and Pan, X., "Task-based optimization of dedicated breast CT via Hotelling observer metrics," *Med. Phys.* **41**(10), 101917 (2014).

[72] Sanchez, A. A., Sidky, E. Y., and Pan, X., "Region of interest based Hotelling observer for computed tomography with comparison to alternative methods," *J. Med. Imaging* **1**(3), 031010 (2014).

[73] Rose, S. D., Sidky, E. Y., Sanchez, A. A., and Pan, X., "Investigating pixel size and resolution in optimization-based CT image reconstruction," in [*Proc. 4th Intl. Mtg. image Form. X-ray CT*], 287–290 (2016).

[74] Myers, K. J., Rolland, J. P., Barrett, H. H., and Wagner, R. F., "Aperture optimization for emission imaging: effect of a spatially varying background," *J. Opt. Soc. Am. A.* **7**(7), 1279–1293 (1990).

[75] Metheany, K. G., Abbey, C. K., Packard, N., and Boone, J. M., "Characterizing anatomical variability in breast CT images," *Med. Phys.* **10**, 4685–4694 (2008).

[76] Chen, L., Abbey, C. K., Nosratieh, A., Lindfors, K. K., and Boone, J. M., "Anatomical complexity in breast parenchyma and its implications for optimal breast imaging strategies," *Med. Phys.* **3**, 1435–1441 (2012).

[77] Chen, L., Boone, J. M., and Abbey, C. K., "Association between power law coefficients of the anatomical noise power spectrum and lesion detectability in breast imaging modalities," *Phys. Med. Biol.* **58**, 1663–1681 (2013).

[78] Vedantham, S., Shi, L., Karellas, A., O'Connell, A. M., and Conover, D., "Dedicated Breast CT: Anatomic Power Spectrum," in [*Proc. 2nd Int. Mtg. image Form. X-ray CT*], 70–73 (2012).

[79] Fessler, J. A. and Rogers, W. L., "Spatial resolution properties of penalized-likelihood image reconstruction: Space-invariant tomographs," *IEEE Trans. Image Process.* **5**(9), 1346–1358 (1996).

[80] Qi, J. and Huesman, R. H., "Lesion detectability of MAP reconstruction using computer observer: A theoretical study.," *J. Nucl. Med.* **41**(5), 18p–19p (2000).

[81] Cloquet, C. and Defrise, M., "MLEM and OSEM Deviate From the Cramer-Rao Bound at Low Counts," *IEEE Trans. Nucl. Sci.* **60**(1), 134–143 (2013).

[82] Tanner, W. P. and Birdsall, T. G., "Definitions of d' and η as Psychophysical Measures," *J. Acoust. Soc. Am.* **30**(10), 922–928 (1958).

[83] Barrett, H. H. and Swindell, W., [*Radiological Imaging: The Theory of Image Formation, Detection, and Processing*], Academic Press, San Diego (1996).

[84] Burgess, A. E. and Judy, P. F., "Signal detection in power-law noise : effect of spectrum exponents," *J. Opt. Soc. Am. A.* **24**(12), 52–60 (2007).

[85] Frikel, J. and Quinto, E. T., "Characterization and reduction of artifacts in limited angle tomography," *Inverse Probl.* **29**(12), 125007 (2013).

[86] Reiser, I., Edwards, A., and Nishikawa, R. M., "Validation of a power-law noise model for simulating small-scale breast tissue," *Phys. Med. Biol.* **58**(17), 6011–6027 (2013).

[87] Sanchez, A. A., "Estimation of noise properties for TV-regularized image reconstruction in computed tomography," *Phys. Med. Biol.* **60**(18), 7007–7033 (2015).

[88] Bonetto, P., Qi, J., and Leahy, R. M., "Covariance approximation for fast and accurate computation of channelized Hotelling observer statistics," *IEEE Trans. Nucl. Sci.* **47**(4), 1567–1572 (2000).

[89] Zhao, B., Zhou, J., Hu, Y.-H., Mertelmeier, T., Ludwig, J., and Zhao, W., "Experimental validation of a three-dimensional linear system model for breast tomosynthesis," *Med. Phys.* **1**, 240–251 (2009).

[90] Chawla, A. S., Lo, J. Y., Baker, J. A., and Samei, E., "Optimized image acquisition for breast tomosynthesis in projection and reconstruction space," *Med. Phys.* **36**(11), 4859–4869 (2009).

[91] Lu, Y., Chan, H.-P., Wei, J., Goodsitt, M., Carson, P. L., Hadjiiski, L., Schmitz, A., Eberhard, J. W., and Claus, B. E. H., "Image quality of microcalcifications in digital breast tomosynthesis: Effects of projection-view distributions," *Med. Phys.* **38**(10), 5703–5712 (2011).

[92] Tucker, A. W., Hill, C., and Zhou, O., "Dependency of image quality on system configuration parameters in a stationary digital breast tomosynthesis system," *Med. Phys.* **40**(3), 031917 (2013).

[93] Chan, H.-P., Goodsitt, M. M., Helvie, M. A., Zelakiewicz, S., Schmitz, A., Noroozian, M., Pramagul, C., Roubidoux, M. A., Nees, A. V., Neal, C. H., Carson, P., Lu, Y., Hadjiiski, L., and Wei, J., "Digital breast tomosynthesis: Observer performance of clustered microcalcification detection on breast phantom images acquired with an experimental system using variable scan angles, angular increments, and number of projection views," *Radiology* **273**(3), 675–685 (2014).

[94] Goodsitt, M. M., Chan, H.-P., Schmitz, A., Zelakiewicz, S., Telang, S., Hadjiiski, L., Watcharotone, K., Helvie, M. A., Colleen, N., Paramagul, C., Christodoulou, E., Larson, S. C., and Carson, P. L., "Digital breast tomosynthesis: Studies of the effects of acquisition geometry on contrast-to-noise ratio and observer preference of low-contrast objects in breast phantom images," *Phys Med Biol.* **59**(19), 5883–5902 (2014).

[95] Mertelmeier, T., Orman, J., Haerer, W., and Dudam, M. K., "Optimizing filtered backprojection reconstruction for a breast tomosynthesis prototype device," in [*Proc SPIE*], **6142**, 131–142 (2006).

[96] Sanchez, A. A., Sidky, E. Y., and Pan, X., "Use of the Hotelling observer to optimize image reconstruction in digital breast tomosynthesis," *J. Med. Imaging* **3**(1), 011008 (2015).

[97] Rose, S. D., Sanchez, A. A., Sidky, E. Y., and Pan, X., "Investigating simulation-based metrics for characterizing linear iterative reconstruction in digital breast tomosynthesis," *Med. Phys.* **44**(9), 279–296 (2017).

[98] Maidment, A., "AAPM Medical Physics Tutorial Session 1: Digital Breast Tomosynthesis," Presented at the 2017 meeting of the Radiological Society of North America.

[99] Li, X., Da, Z., and Liu, B., "A generic geometric calibration method for tomographic imaging systems with flat-panel detectors – A detailed implementation guide.," *Med. Phys.* **37**(7), 3844–3854 (2010).

[100] Gomi, T., Hirano, H., and Umeda, T., "Computerized medical imaging and graphics evaluation of the X-ray digital linear tomosynthesis reconstruction processing method for metal artifact reduction," *Comput. Med. Imaging Graph.* **33**, 267–274 (2009).